ZEOLITE MEMBRANES FOR THE SEPARATION OF KRYPTON AND XENON FROM SPENT NUCLEAR FUEL REPROCESSING OFF-GAS

A Thesis
Presented to
The Academic Faculty

by

Phillip Grant Crawford

In Partial Fulfillment
of the Requirements for the Degree
Master of Science in Chemical Engineering in the
School of Chemical and Biomolecular Engineering

Georgia Institute of Technology
December 2013

ZEOLITE MEMBRANES FOR THE SEPARATION OF KRYPTON AND XENON FROM SPENT NUCLEAR FUEL REPROCESSING OFF-GAS

Approved by:

Dr. Sankar Nair, Advisor
School of Chemical and Biomolecular Engineering
Georgia Institute of Technology

Dr. Ramesh Bhave
Senior Scientist
Oak Ridge National Laboratory

Dr. David Sholl
School of Chemical and Biomolecular Engineering
Georgia Institute of Technology

Date Approved: November 16, 2013

ACKNOWLEDGEMENTS

There is no way I could have completed all this work without a tremendous amount of help and support from my advisors, labmates, and family. First, I thank my advisor Prof. Sankar Nair and my co-advisor Dr. Ramesh Bhave for giving me this amazing opportunity. I started this project with almost no experience with zeolite membranes, but Prof. Nair patiently guided me through my entire graduate research experience and has substantially influenced my development as an engineer and scientist. I am also grateful for all the support and advise Dr. Bhave gave me throughout this research, especially during my visits to Oak Ridge National Lab (ORNL). The knowledge and experience I gained while working with many talented scientists and engineers at ORNL was indispensable to my success as a graduate researcher. In addition to my committee members Prof. Nair and Dr. Bhave, I thank Prof. David Sholl for agreeing to be part of my thesis committee and providing me with excellent feedback after my defense presentation.

During this research, my labmates have been both friends and mentors to help me overcome many challenges. Without their expertise, none of this work would have been possible. They have taught me everything I know about zeolite synthesis, characterization, and testing, and I am extremely grateful for all the help I have received. I especially thank Dr. Seok-Jhin Kim for teaching me how to synthesize and test zeolite membranes. I also thank Dr. Pyungsoo Lee for guiding me through my first zeolite synthesis at ORNL. I thank Dr. Mohamad Kassaee and Andrew Brown for their extensive help with zeolite permeation testing. I thank Kiwon Eum for his help with operating the pressure decay cell and for being an awesome office mate in general (along with Dr.

Jason Bentley). I also thank Krishna Jayachandrababu, Ben Ivey, Seung Won Choi, Dr. Hyung Ju Kim, Dr. Fereshteh Rashidi, and Dr. Zhengzhi Zhou for the help they provided me.

I thank my parents and sister for their unwavering support and love during my undergraduate and graduate career at Georgia Tech. My Mom and Dad are the biggest influences of my life and their unfaltering commitment to me has given me tremendous confidence and encouragement during my studies at Georgia Tech. Finally, I thank God and Jesus Christ for all the blessings and loving people in my life.

TABLE OF CONTENTS

LIST OF TABLES

LIST OF FIGURES

SUMMARY

The goal of this research was to identify and fabricate zeolitic membranes that can separate radioisotope krypton-85 (half-life 10.72 years) and xenon gas released during spent nuclear fuel reprocessing. In spent nuclear fuel reprocessing, fissionable plutonium and uranium are recovered from spent nuclear fuel and recycled. During the process, krypton-85 and xenon are released from the spent nuclear fuel as process off-gas. The off-gas also contains NO, NO_2, ^{129}I, ^{85}Kr, $^{14}CO_2$, tritium (as ^3H_2O), and air and is usually vented to the atmosphere as waste without removing many of the radioactive components, such as ^{85}Kr. Currently, the US does not reprocess spent nuclear fuel. However, as a member of the International Framework for Nuclear Energy Cooperation (IFNEC, formerly the Global Nuclear Energy Partnership), the United States has partnered with the international nuclear community to develop a “closed” nuclear fuel cycle that efficiently recycles all used nuclear fuel and safely disposes all radioactive waste byproducts. This research supports this initiative through the development of zeolitic membranes that can separate ^{85}Kr from nuclear reprocessing off-gas for capture and long-term storage as nuclear waste. The implementation of an $^{85}Kr/Xe$ separation step in the nuclear fuel cycle yields two main advantages. The primary advantage is reducing the volume of ^{85}Kr contaminated gas that must be stored as radioactive waste. A secondary advantage is possible revenue generated from the sale of purified Xe.

This research proposed to use a zeolitic membrane-based separation because of their molecular sieving properties, resistance to radiation degradation, and lower energy requirements compared to distillation-based separations. Currently, the only commercial process used to separate Kr and Xe is cryogenic distillation. However, cryogenic

distillation is very energy intensive because the boiling points of Kr and Xe are -153 °C and -108 °C, respectively. The ^{85}Kr/Xe separation step was envisioned to run as a continuous cross-flow filtration process (at room temperature using a transmembrane pressure of about 1 bar) with a zeolite membrane separating krypton-85 into the filtrate stream and concentrating xenon into the retentate stream. To measure process feasibility, zeolite membranes were synthesized on porous α-alumina support discs and permeation tested in dead-end filtration mode to measure single-gas permeance and selectivity of CO_2, CH_4, N_2, H_2, He, Ar, Xe, Kr, and SF_6. Since the kinetic diameter of krypton is 3.6 Å and xenon is 3.96 Å, zeolites SAPO-34 (pore size 3.8 Å) and DDR (pore size 3.6 Å) were studied because their pore sizes are between or equal to the kinetic diameters of krypton and xenon; therefore, Kr and Xe could be separated by size-exclusion. Also, zeolite MFI (average pore size 5.5 Å) permeance and selectivity were evaluated to produce a baseline for comparison, and amorphous carbon membranes (pore size < 5 Å) were evaluated for Kr/Xe separation as well.

After permeation testing, MFI, DDR, and amorphous carbon membranes did not separate Kr and Xe with high selectivity and high Kr permeance. However, SAPO-34 zeolite membranes were able to separate Kr and Xe with an average Kr/Xe ideal selectivity of 11.8 and an average Kr permeance of 19.4 GPU at ambient temperature and a 1 atm feed pressure. Also, an analysis of the SAPO-34 membrane defect permeance determined that the average Kr/Xe selectivity decreased by 53% at room temperature due to unselective defect permeance by Knudsen diffusion. However, sealing the membrane defects with polydimethylsiloxane increased Kr/Xe selectivity by 32.8% to 16.2 and retained a high Kr membrane permeance of 10.2 GPU at ambient temperature. Overall, this research has shown that high quality SAPO-34 membranes can be consistently fabricated to achieve a Kr/Xe ideal selectivity >10 and Kr permeance >10 GPU at ambient temperature and 1 atm feed pressure. Furthermore, a scale-up analysis based on the experimental results determined that a cross-flow SAPO-34 membrane with a Kr/Xe selectivity of 11.8 and an area of 4.2 m^2 would recover 99.5% of the Kr from a 1 L/min feed stream containing 0.09% Kr and 0.91% Xe at ambient temperature and 1 atm feed pressure. Also, the membrane would produce a retentate stream containing 99.9% Xe. Based on the SAPO-34 membrane analysis results, further research is warranted to develop SAPO-34 membranes for separating ^{85}Kr and Xe.

CHAPTER 1

INTRODUCTION

1.1 Motivation and Background

As the world searches for alternative energy sources to fossil fuels, many countries have invested in nuclear energy because the technology is currently available, does not use fossil fuels, and avoids greenhouse gas emissions such as carbon dioxide. In 2012, nuclear power plants produced 11.3% of the total electrical power produced worldwide, and in December 2012 there were 67 nuclear power reactors under construction throughout the world.[1,2] The main drawback to nuclear power is the production of nuclear waste, and in 2008 the world nuclear industry was estimated to generate 10,500 tHM (metric ton of heavy metal) per year of spent nuclear fuel with total spent nuclear fuel generated projected as 445,000 tHM worldwide by year 2020.[3] Nuclear fuel for nuclear power plants is produced from fissionable materials (usually uranium and plutonium) through a series of processes called the nuclear fuel cycle, and spent nuclear fuel can be recycled through a process called nuclear reprocessing, which recovers fissionable materials to be reused as nuclear fuel.[3] Currently, the United States (US) does not reprocess spent nuclear fuel generated from commercial nuclear power plants .The US discontinued nuclear reprocessing in 1976 as part of a nuclear non-proliferation policy. In 1981, the ban on nuclear reprocessing in the US was lifted, but the US has continued to employ a “once through” nuclear cycle that stores all spent nuclear fuel as nuclear waste after a single use.[4] However, as a member of the International Framework for Nuclear Energy Cooperation (IFNEC, formerly the Global Nuclear Energy Partnership), the US has partnered with the international nuclear community to develop a "closed" nuclear fuel cycle that efficiently recycles all used nuclear fuel and safely disposes all radioactive waste byproducts.[4] This research aimed to identify, fabricate, and characterize zeolitic membranes that can separate radioactive krypton-85 and xenon gas released during nuclear reprocessing, which supports the overall strategy of the United States and the IFNEC to develop and implement a worldwide closed nuclear fuel cycle.[5]

1.2 Release of Krypton and Xenon during Nuclear Reprocessing

Aqueous nuclear reprocessing usually begins by shearing and chopping spent fuel rods into smaller pieces, and then the pieces are oxidized at high temperature through a process called voloxidation. The resulting oxide powder is dissolved in acidic solution (usually nitric acid) to convert the spent nuclear fuel into an aqueous solution for further processing.[6] Then the solution is chemically processed to recover uranium and plutonium primarily using a series of precipitation and/or liquid-liquid extraction steps.[7] Plutonium and Uranium Recovery by Extraction (PUREX) nuclear reprocessing technology can recover up to 99.5% of the fissionable uranium and plutonium from used nuclear fuel.[3]

During the fission of uranium and plutonium in a nuclear reactor, gaseous fission products krypton-85 and xenon-135 are formed and trapped in the solid fuel rods.[8] Krypton-85 is a radioisotope that has a half-life of 11 years and decays into stable rubidium-85.[9] Xenon-135 is a radioisotope with a half-life of 9.2 hours, and xenon-135 that captures a neutron transmutes to stable xenon-136.[8,10] Xenon-135 that does not capture a neutron transmutes to radioisotope cesium-135 (2.3×10^6 years), but in a nuclear reactor essentially all of the xenon-135 produced adsorbs a neutron and transmutes to stable xenon.[10,11] The yield of krypton-85 and xenon-135 from uranium fission is about 0.3% and 6.5%, respectively.[9,11] Nuclear fission consumes the uranium or plutonium in the nuclear fuel rods, and the fuel rods become depleted (spent nuclear fuel) when not enough uranium or plutonium is present to sustain a nuclear chain reaction.

Radioisotope krypton-85 (^{85}Kr) and stable xenon-136 (Xe) are released from the spent nuclear fuel during the shearing/chopping, voloxidation, and acid dissolution steps as process off-gas.[6] When using nitric acid to dissolve the spent fuel, the process off gas contains NO, NO_2, radioisotope iodine-129 (^{129}I, half-life 1.6 x 10^7 years), Xe, ^{85}Kr, CO_2 containing radioisotope carbon-14 (^{14}C, half-life 5,730 years), ^{3}H (radioactive tritium, half-life 10.3 years), and air.[5,6,12-14] Based on test data from Oak Ridge National Laboratory (ORNL), the concentration of ^{85}Kr in the process-off is estimated to range from 100 to 1000 ppm, and the Xe concentration is estimated to be 10 times the concentration of ^{85}Kr.[5,14] In countries that currently employ commercial scale nuclear reprocessing (such as Russia, Japan, France, and the United Kingdom), the process off-gas is usually treated to reduce the concentration of certain radioactive isotopes (usually ^{129}I and/or tritium), but even with treatment the off-gas (including ^{85}Kr and Xe) is largely vented into the atmosphere.[3]

1.3 Krypton and Xenon Separation for Krypton Capture

To implement a closed nuclear fuel cycle in the US, the vented process off-gas must meet Environmental Protection Agency (EPA) requirements specified by 40 CFR 190 and 10 CFR 20. 40 CFR 190 requires that ^{85}Kr and ^{129}I emissions must be less than 50,000 curies and 5 millicuries, respectively, per gigawatt-year of electrical energy produced by the nuclear fuel cycle. 10 CFR 20 sets dose limits for workers and individual members of the public for tritium, ^{14}C (as CO_2), ^{85}Kr, and ^{129}I in the air at a defined site boundary and in water.[6] The dose limits are listed in Table 1.1.

Table 1.1: 10 CFR 20 dose limits for workers and individual members of the public.[6]

	Air (Ci/m^3) at Site Boundary	Water (Ci/m^3)
Tritium (^3H)	1.0×10^{-7}	1.0×10^{-3}
Carbon-14 (as CO_2)	3.0×10^{-5}	-
Krypton-85	7.0×10^{-7}	-
Iodine-129	4.0×10^{-11}	2.0×10^{-7}

Economical technologies already exist to separate, capture, and dispose of ^{129}I, tritium, and CO_2 containing ^{14}C.[5-7,12-14] However, it would be desirable to also separate Xe from ^{85}Kr to reduce the volume of radioactive waste captured for long-term decay storage and also because Xe is a high-value rare noble gas, but since ^{85}Kr and Xe are essentially chemically inert they can only be physically separated.[6,14] To meet EPA requirements, all ^{85}Kr contaminated off-gas must be captured and stored as radioactive waste until the ^{85}Kr decays to safe radioactive levels. Historically, ^{85}Kr has been captured and stored in compressed gas cylinders. While in operation from 1953 to 1992, the Idaho Chemical Processing Plant (at Idaho National Laboratory) processed spent nuclear fuel and stored ^{85}Kr as 90% Xe-10% ^{85}Kr mixtures in pressurized gas cylinders.[15] Therefore, separating Xe from ^{85}Kr would significantly reduce the storage volume of ^{85}Kr contaminated off-gas and reduce the storage costs.[5,15] Furthermore, decommissioned nuclear reprocessing facilities in the US (Savannah River Plant and Idaho Chemical

Processing Plant) reported that 4.7 kg of Xe evolve as off-gas per metric ton of heavy metal.[15] A nuclear reprocessing facility with an 800 tHM/year recycle capacity would release approximately 3700 kg of Xe (6.3 x 10^5 standard liters) per year, which, sold for \$25/L (Airgas® pricing in March 2013 for 99.995% research grade Xe), would yield \$16 million of Xe recovered per year. Therefore, the main advantages of separating ^{85}Kr from Xe in nuclear reprocessing off-gas are reductions in storage costs and possible revenue generated from the sale of purified Xe.

1.4 Krypton/Xenon Separation Technologies

Primarily, only four technologies have been explored for the separation of ^{85}Kr and Xe from nuclear reprocessing off-gas: cryogenic distillation, fluorocarbon adsorption, solid adsorption on activated charcoal and zeolites, and permeation through silicone rubber membranes. [5,6,14,15,16-18]

1.4.1 Cryogenic Distillation

Purified Xe and Kr are commercially produced through cryogenic fractional distillation of liquefied air (Xe and Kr occur naturally in the atmosphere at 1 ppm and 0.08 ppm by volume, respectively), but the process required for a nuclear processing plant is on a much smaller scale.[15] In the past, cryogenic distillation processes were developed and operated to capture ^{85}Kr from nuclear reprocessing dissolver off-gas in the US, and a detailed description of this type of process is given by Moore.[5,15,19] The main disadvantage of cryogenic distillation is the high operating cost due to relatively high power requirements compared to adsorption and membrane processes, which Waggoner estimated in 1981 to be the highest among the three technologies (110% higher than fluorocarbon adsorption and 24% higher than mordenite adsorption).[20,21]

1.4.2 Fluorocarbon Adsorption

Fluorocarbon adsorption uses the organic solvent dichlorodifluoromethane (CCl_2F_2) to selectivity adsorb ^{85}Kr and Xe from the process off-gas. Then the solvent is boiled to remove and recover the noble the gases. This technology has moved through many pilot scale development phases and can recover > 99% of ^{85}Kr from the feed stream, and typical product stream composition after one fluorocarbon adsorption step was reported as: CO_2-78%, Xe-13%, N_2-5.5%, Kr-2.0%, O_2-1.4%, and Ar-0.1%.[5,14] Therefore, to separate ^{85}Kr and Xe and reduce the ^{85}Kr decay storage volume and costs, additional process steps would be required.[15] Furthermore, the use of CCl_2F_2 was banned in the United States by the Montreal Protocol in 1996 because it depletes ozone in the Earth's atmosphere. Therefore, a new organic solvent would need to be identified and tested to replace CCl_2F_2.

1.4.3 Solid Adsorption on Activated Charcoal and Zeolites

Cryogenic activated charcoal adsorption has been used to produce research grade purity Kr at ORNL, and activated carbon at low temperatures (ACHAT) has been shown on an industrial scale to produce > 99% Kr product streams by the Jülich Research Centre in Germany.[5,15] The main drawback to using activated carbon is O_2 and NO_x must be removed from the feed stream because activated charcoal is combustible.[15,16]

The silver-exchanged synthetic zeolite mordenite (AgZ) has been studied to selectively remove and recover Xe from process streams containing Kr.[5,15] In this process the Xe is adsorbed from a feed stream at ambient temperatures on an AgZ bed and then the Kr is adsorbed at -80 °C on a hydrogen mordenite (HZ) bed. The Kr is desorbed from the HZ bed at 60 °C and concentrated by two more HG adsorption steps then finally captured with a cold trap. The Xe is desorbed from the AgZ bed at 200-250 °C. The main disadvantages with this method are Xe/Kr selectivity in the first step and capital costs. Lab scale tests at the Oak Ridge Gaseous Diffusion Plant at ORNL have shown that approximately 5% of the Kr is adsorbed with the Xe in the first step and additional purification may be required to remove the Kr.[5,15] Also, an economic analysis by Waggoner in 1981 estimated that the capital for the mordenite adsorption process is the highest among the three technologies (36% higher than cryogenic distillation and 64% higher than fluorocarbon adsorption).[21]

1.4.4 Permeation through Silicone Rubber Membranes

In 1971 the Oak Ridge Gaseous Diffusion Plant studied separation of Kr and Xe by selective permeation through silicon rubber membranes (thin sheets) because of the advantages of membrane processes compared to the other listed Kr/Xe separation processes. These advantages included: no fire/explosion hazard, relatively low operating costs, small equipment size, and ambient operating temperature. However, the ORNL researchers estimated the capital costs of a silicon membrane separation process based on their results and found that it is greater than the capital costs of traditional adsorption and extraction separation processes.[16] Also, in 1980 Stern et. al. studied the permeation of Xe and Kr through silicon rubber capillaries (hollow fibers) and measured effective permeability coefficients of 21.0 x 10^{15} kg-m^2/(s-m^2-Pa) for Kr and 73.1 x 10^{15} kg-m^2/(s-m^2-Pa) for Xe at 20 °C.[17,18] But in 1981 Waggoner determined that silicone membranes are not sufficiently selective for a silicon membrane Kr/Xe separation process to be cost effective.[21]

1.5. Zeolite Membranes for Krypton and and Xenon Separation

As mentioned earlier, at present the only Kr and Xe separation process commercially used is fractional cryogenic distillation, which is very energy intensive because the atmospheric boiling points of Kr and Xe are -153°C and -108°C, respectively.[5,15] This research examines the membrane-based separation of ^{85}K from Xe and proposes to use zeolite membranes because of their molecular sieving properties, resistance to radiation degradation, and lower energy requirements compared to cryogenic distillation.[15,20,22,23] The ^{85}Kr/Xe separation step is envisioned to run as a continuous cross-flow membrane process at room temperature using a transmembrane pressure of about 1 bar, with a zeolite membrane separating a pre-concentrated ^{85}Kr/Xe feed gas into a filtrate stream containing concentrated ^{85}Kr and retentate stream containing concentrated Xe.

Zeolites are microporous aluminosilicate materials with highly repeating three-dimensional crystalline structures. Zeolites occur naturally and can also be produced synthetically. Zeolites consist of aluminum and silicon atoms (“T-atoms”) that are bonded by oxygen atoms (“O-bridges”) to form tetrahedral TO_4 units. Zeolites can also contain phosphorous, germanium, boron, zinc or only silicon as T-atoms. The TO_4 units interconnect to form a network of repeating pores, channels, and cavities. Zeolite pore sizes are < 2 nm, and the zeolite framework void space contains positively charged cations that electrostatically bond to the negatively charged TO_4 units ($[SiO_4]^{4-}$ and $[AlO_4]^{5-}$) to give the zeolite framework zero net charge. Zeolites can be classified by their Si/Al molar ratio as given in Table 2.1.[22,24]

Table 1.2: Zeolite classification by Si/Al ratio.[22,25]

	Si/Al Molar Ratio	Zeolite Characteristic
Low Silica (Al-Rich)	~ 1 - 1.5	Hydrophilic
Intermediate Silica	~ 2 - 5	-
High Silica	~ 10 -100	Hydrophobic, Organophilic
Pure Silica	∞	Hydrophobic, Organophilic

Zeolites are commercially used as adsorbents for air purification, catalysts for petroleum cracking, and ion-exchange water softeners for water purification, but within the last 20 years zeolites have been studied extensively for use as membranes for liquid and gas separations.[26-28] Zeolite membranes can selectively permeate molecules based on molecular size differences less than 1 Å because molecules smaller than the zeolite pores pass through the membranes with less resistance than molecules larger than the zeolite pores, an effect know as molecular sieving.[22] For example, MFI membranes have been shown to have *p*-xylene/*o*-xylene permselectivities from 23 to 278 for equilmolar binary mixtures at 125 °C.[29] Also, high CO_2/CH_4 permselectivities have been reported for DDR and SAPO-34 membranes. Li et al. reported average CO_2/CH_4 permselectivities around

250 for SAPO-34 membranes with equilmolar binary mixtures at 22 °C, and Bergh et al. reported CO_2/CH_4 permselectivities from 100 to 3000 for DDR with equilmolar binary mixtures at -53°C to 100 °C.[30,31] Zeolites also have excellent thermal and chemical stability, and zeolite membranes can be used for applications that would degrade and destroy polymer membranes, such as radioactive material separations in the nuclear industry and high pressure CO_2/CH_4 in the oil and gas industry.[26,27,32] However, issues still exist with the fabrication of zeolite membranes, such as high capital costs and membrane defect formation (cracks, pinholes, and grain boundaries), that have prevented zeolite membranes from being readily adopted by industry.[27,33]

To investigate process feasibility, three zeolites (MFI, SAPO-34, and DDR) were synthesized on porous α-alumina support discs or tubes, and permeation measurements were carried out in dead-end filtration mode to determine single-gas permeance and permselectivity of CO_2, CH_4, N_2, H_2, He, Ar, Xe, Kr, and SF_6. I hypothesized that zeolites SAPO-34 (pore size 3.8 Å) and DDR (pore size 3.6 Å) may be selective Kr/Xe membranes because their crystal structure pore sizes are between or equal to the kinetic diameters of krypton (3.6 Å) and xenon (3.96 Å).[34,35] Gas permeation measurements on MFI (average pore size 5.5 Å) were used to establish a baseline for comparison since MFI has been well study.[36] Amorphous carbon membranes (pore size < 5 Å) were also tested to determine their Kr/Xe permeance and permselectivity.[37] A graph of gas kinetic diameters and the zeolite/carbon membrane pore sizes is given in Figure 1.1.

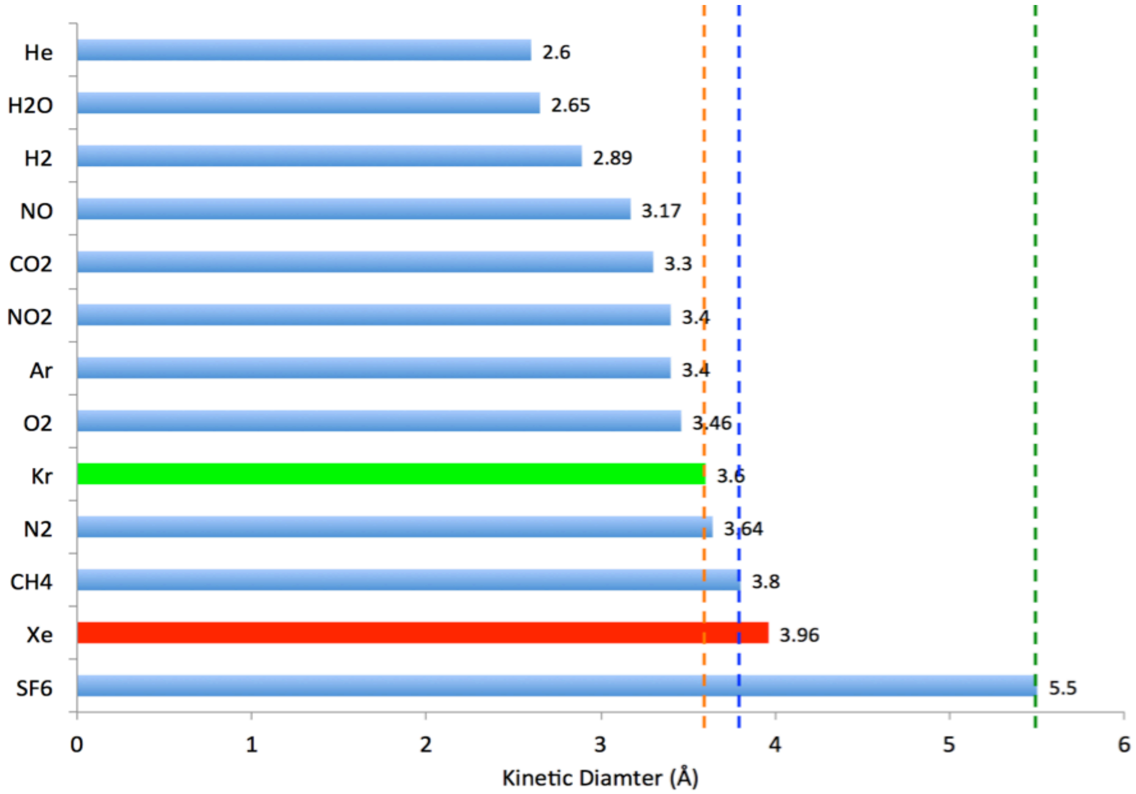

Figure 1.1: Kinetic diameters of certain molecules (Kr is highlighted green and Xe is highlighted red). MFI average pore size (5.5 Å) is the green dashed line, SAPO-34 pore size (3.8 Å) is the blue dashed line, DDR pore size (3.6 Å) is the orange dashed line.[34,37]

1.6 Proposed ^{85}Kr/Xe Concentration and Off-Gas Treatment Process

For a zeolite membrane-based separation step of ^{85}Kr and Xe to be a viable separation route, the feed stream to this separation step must be pre-concentrated with respect to ^{85}Kr and Xe by reducing the concentrations of the of NO_x, CO_2, N_2, H_2O, and O_2 in an upstream off-gas treatment process. An off-gas treatment process to capture all radioactive components and concentrate the off-gas into an essentially binary mixture of ^{85}Kr and Xe, without the use of cryogenic distillation, is proposed and illustrated in Figure 1.2. However, the development of a complete off-gas treatment process was outside the scope of this research and many of the unit-operations proposed in Figure 1.2 are still in the research and development phase.

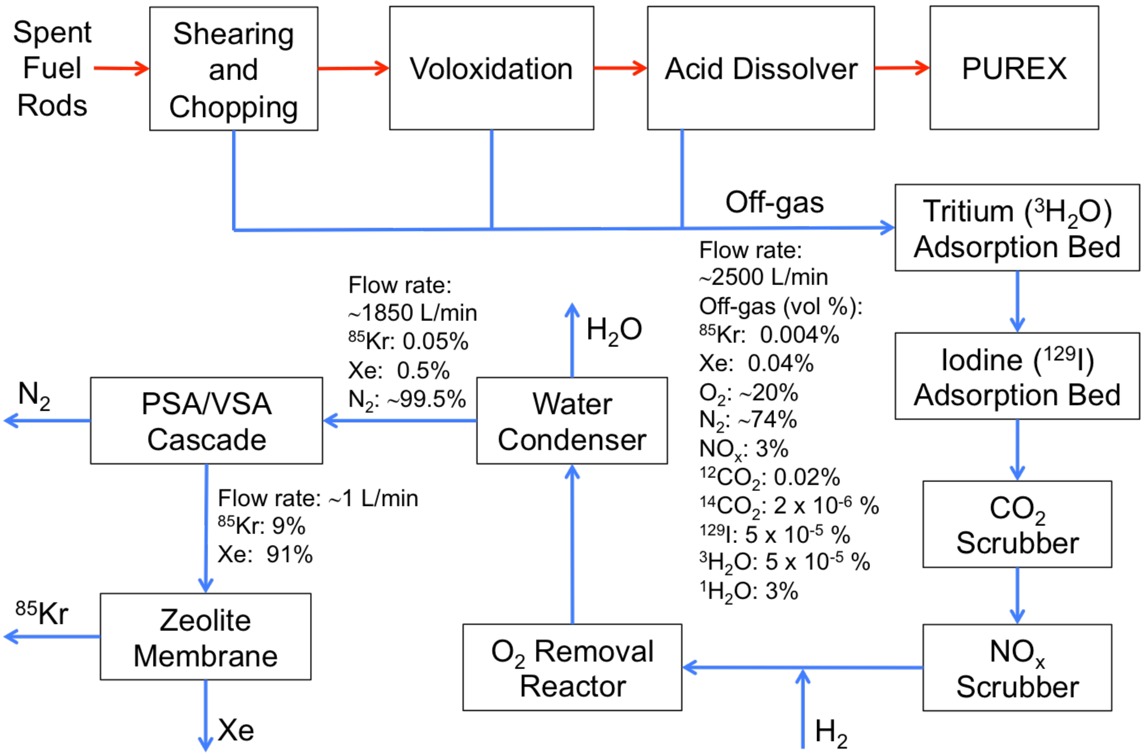

Figure 1.2: Process flow diagram for proposed off-gas treatment process. Red lines indicate solid and aqueous streams (uranium and plutonium), blue lines indicate gas streams (process off-gas).

In Figure 1.2, the off-gas is collected from the shearing and chopping, voloxidation, and acid dissolver steps. Voloxidation of the fuel is usually performed in air so the majority of off-gas is composed of oxygen (~20%) and nitrogen (~74%), however advanced voloxidation techniques are under development that use pure O_2 or oxidants other than O_2.[6,39] Figure 1.2 also lists the estimated combined off-gas flow rate and composition containing 0.004 % ^{85}Kr and 0.04% Xe (estimated by Gombert, Rubin et al., and Bhave et al.).[5,15,39] Before the off-gas enters the tritium adsorption step, it is filtered through a sintered metal HEPA (high efficiency particulate absorption) filter and then all released tritium is converted to tritiated water (^3H_2O) by flowing the off-gas stream through a heated catalytic combiner containing a copper catalyst. The tritiated water and any other water is removed from the off-gas by adsorption onto Linde Type 3A zeolite.[5,14] Next, ^{129}I is removed by adsorption onto silver-exchanged zeolites AgX (faujasite) or AgZ (mordenite). CO_2 (including $^{14}CO_2$ and $^{12}CO_2$) is removed with a caustic scrubber using NaOH solution. CO_2 can also be removed by adsorption on molecular sieves such as Linde Type 4A zeolite.[14] The CO_2 scrubber step will also remove NO_x, but a subsequent NO_x wet scrubber may be necessary to completely remove NO_x from the off-gas. The NO_x scrubber can use alkaline water or water alone to strip NO_x from the off-gas.[40] Next, hydrogen is introduced into the stream and reacted with O_2 over a palladium-platinum catalyst at ~550 °C to form water. Then a condenser (cold trap) removes the water.[15]

After leaving the condenser, the off-gas stream contains approximately 0.05% ^{85}Kr and 0.5% Xe with the balance as N_2. Next, the N_2 is removed by a series of pressure swing adsorption (PSA) and/or vacuum swing adsorption (VSA) steps that selective adsorb ^{85}Kr and Xe over N_2 using activated carbon and/or molecular sieves. Although this research did not find any studies that have separated Kr and Xe from $Kr/Xe/N_2$ mixtures using PSA and/or VSA, Kawai et al. has shown that Kr can be separated from N_2 using a two step process of equilibrium PSA (adsorbent was activated carbon) followed by rate-dependent PSA (adsorbent was Linde Type 4A zeolite). Kawai et al. separated a 30% Kr/70% N_2 mixture into 99.99% Kr 99.9% N_2 and 99.9% N_2 outlet streams.[41] Also, Karwacki et al. demonstrated that Xe can be separated from N_2 using VSA with AgLiX (silver-lithium exchanged faujasite) zeolite or activated carbon adsorbent. Karwacki et al. increased the concentration of Xe by ≥1500% from a feed of 1% Xe/99% N_2 with a Xe recovery rate of 75-99% and a maximum Xe/N_2 adsorption selectivity (ratio of Henry's constants) of ~75.[42] Currently, PSA/VSA processes are being evaluated by ORNL for the separation of ^{85}Kr and Xe from N_2.[39]

After the off-gas is concentrated into a binary ^{85}Kr/Xe stream (estimated flow rate is 10 L/min with a composition of 9% ^{85}Kr/91% Xe after removing all the N_2), a zeolite membrane separates the mixture into ^{85}Kr (permeate) and Xe (retentate) streams. The Xe stream can be considered pure when the ^{85}Kr radioactivity level meets the requirements set by 10 CFR 20 ($\leq 7 \times 10^{-7}$ Ci/m^3), which corresponds to a ^{85}Kr concentration of ≤ 0.5 ppb. The Xe retentate stream can be further purified through a series of zeolite membrane separation steps until the desired ^{85}Kr concentration is achieved.

1.7 Research Objectives

The objectives of this research were:

1) To synthesize MFI, SAPO-34, and DDR membranes on α-alumina support discs and/or tubes,
2) Characterize the permeation properties of the membranes in dead-end filtration mode by measuring single-gas permeance and permselectivity of the gases CO_2, CH_4, N_2, H_2, He, Ar, Xe, Kr, and SF_6,
3) Use the permeation data to assess their potential for Kr/Xe separations relevant to the nuclear fuel cycle.

All zeolite membranes were characterized by X-ray diffraction and scanning electron microscopy. Also, amorphous carbon membranes were received from ORNL and tested in dead-end filtration mode to measure single-gas permeance and permselectivity of CO_2, CH_4, N_2, H_2, He, Ar, Xe, Kr, and SF_6. The amorphous carbon membranes were synthesized or characterized prior to permeation testing by ORNL, but not as part of this research. Also, during the course of this research I examined the use of an ultraviolet (UV) light treatment process to treat SAPO-34 membranes before calcination. We hypothesized that treatment with UV light may aid template removal from the SAPO-34 membranes during high temperature calcination because the UV light exposure would degrade the structure directing agents into smaller organic molecules that would vaporize and evolve from the membranes with less resistance, thus producing a higher quality membrane.

The goal for Kr permeance (single-component) through the zeolite membrane was 10 GPU (1 GPU = 3.35×10^{10} mol/m^2/s/Pa). A challenging goal for Kr/Xe ideal permselectivity was 100, however more realistic values ranged from 10 to 50. Although no mixtures were tested in this research, the separation performance of a membrane can be estimated with its ideal permselectivity for those components. For example: given a 50/50 molar composition Kr/Xe feed and a membrane with a Kr/Xe ideal permselectivity of 100, the filtrate (permeate) composition would be 99% Kr/1% Xe.

1.8 References

1. International Atomic Agency. (2013). Energy, Electricity and Nuclear Power Estimates for the Period up to 2050. 1. Retrieved from http://www-pub.iaea.org/MTCD/Publications/PDF/RDS-1-33_web.pdf

2. International Atomic Agency. (2013). Nuclear Power Reactors in the World. 2. Retrieved from http://www-pub.iaea.org/MTCD/Publications/PDF/rds2-33_web.pdf.
3. International Atomic Agency. (2008). Spent Fuel Reprocessing Options. *IAEA-TECDOC-1587*. Retrieved from http://www-pub.iaea.org/MTCD/publications/PDF/te_1587_web.pdf.
4. Andrews, A. (2006). Nuclear Fuel Reprocessing: US Policy Development. Library of Congress Washington DC Congressional Research Service.
5. D. Gombert. (2007). Global Nuclear Energy Partnership: Integrated Waste Management Strategy; Waste Treatment Baseline Study, *DOE Report GNEP-WAST-WAST-AI-RT-2007-000324*.
6. Jubin, R. (2008). Spent Fuel Reprocessing. *Introduction to Nuclear Chemistry and Fuel Cycle Separations Course, Consortium for Risk Evaluation With Stakeholder Participation*, http://www.cresp.org/education/courses/shortcourse.
7. Simpson, M. F., & Law, J. D. (2013). Nuclear Fuel, Reprocessing of. In *Nuclear Energy* (pp. 153-173). Springer New York.
8. Zebroski, E. L. (1967). *U.S. Patent No. 3,356,585*. Washington, DC: U.S. Patent and Trademark Office.
9. Peterson, J., MacDonell, M., Haroun, L., Monette, F., Hildebrand, R. D., & Taboas, A. (2007). Radiological and chemical fact sheets to support health risk analyses for contaminated areas. *Human Health Fact Sheet, Argonne*, 38-39.
10. Roggenkamp, P. L. (2000). The Influence of Xenon-135 on Reactor Operation. *Prepared for the US Department of Energy Under Contract No. DE-ACO9-*

96SR18500 Westinghouse Savannah River Company Savannah River Site, Aiken, SC 29808, 49.

11. Saey, P. R., Bowyer, T. W., & Ringbom, A. (2010). Isotopic noble gas signatures released from medical isotope production facilities—simulations and measurements. *Applied Radiation and Isotopes, 68(9)*, 1846-1854.
12. Haefner, D., Law, J., & Tranter, T. (2010). System Design Description and Requirements for Modeling the Off-Gas Systems for Fuel Recycling Facilities. *INL-2010, Idaho National Laboratory*.
13. Izumi, J. (2003). Waste gas treatment using zeolites in nuclear-related industries. Handbook of Zeolite Science and Technology.
14. Jubin, R. T., DelCul, G. D., Patton, B. D., Owens, R. S., Ramey, D. W., & Spencer, B. B. (2009) Advanced Fuel Cycle Initiative Coupled End-to-End Research, Development, and Demonstration Project: Integrated Off-Gas Treatment System Design and Initial Performance-9226. *Waste Management Conference 2009, Phoenix, AZ.*
15. Moore, E. B. (1984). *Control technology for radioactive emissions to the atmosphere at US Department of Energy facilities* (No. PNL-4621-Final). Pacific Northwest Lab., Richland, WA (USA).
16. Rainey, R.H., Carter, W.L., & Blumkin, S. (1971). Completion Report: Evaluation of the use of Permselective Membranes in the Nuclear Industry for Removing Radioactive Xenon and Krypton form various Off-Gas Streams.
17. Stern, S. A., & Leone, S. M. (1980). Separation of krypton and xenon by selective permeation. *AIChE Journal, 26(6)*, 881-890.

18. Stern, S. A., & Wang, S. C. (1980). Permeation cascades for the separation of krypton and xenon from nuclear reactor atmospheres. *AIChE Journal, 26(6)*, 891-901.
19. Martin, J. R. (1976). *U.S. Patent No. 3,944,646*. Washington, DC: U.S. Patent and Trademark Office.
20. Koros, W. J. (2004). Evolving beyond the thermal age of separation processes: membranes can lead the way. *AIChE Journal, 50(10)*, 2326.
21. Waggoner, R.C. (1982). Technical and economic evaluation of processes for krypton-85 recovery from power fuel-reprocessing plant off-gas. DP-1637.
22. Payra, P., & Dutta, P. K. (2003). Zeolites: a primer. *Handbook of zeolite science and technology*, 1-19.
23. Roddy, J. W. (1981). *Survey: utilization of zeolites for the removal of radioactivity from liquid waste streams*. (No. ORNL/TM-7782). Oak Ridge National Lab., TN (USA).
24. Jacobs, P. A., Flanigen, E. M., Jansen, J. C., & van Bekkum, H. (2001). Introduction to zeolite science and practice. *Elsevier Science*. 1003.
25. Tsutsumi, K., Kawai, T., & Yanagihara, T. (1994). Adsorption Characteristics of Hydrophobic Zeolites. *Studies in Surface Science and Catalysis, 83*, 217.
26. Ackley, M. W., Rege, S. U., & Saxena, H. (2003). Application of natural zeolites in the purification and separation of gases. *Microporous and Mesoporous Materials, 61(1)*, 25-42.

27. Caro, J., Noack, M., Kölsch, P., & Schäfer, R. (2000). Zeolite membranes–state of their development and perspective. *Microporous and mesoporous materials, 38(1)*, 3-24.
28. Caro, J., & Noack, M. (2008). Zeolite membranes–Recent developments and progress. *Microporous and Mesoporous Materials, 115(3)*, 215-233.
29. Nair, S., Lai, Z., Nikolakis, V., Xomeritakis, G., Bonilla, G., & Tsapatsis, M. (2001). Separation of close-boiling hydrocarbon mixtures by MFI and FAU membranes made by secondary growth. *Microporous and mesoporous materials, 48(1)*, 225.
30. Li, S., Carreon, M. A., Zhang, Y., Funke, H. H., Noble, R. D., & Falconer, J. L. (2010). Scale-up of SAPO-34 membranes for CO_2/CH_4 separation. Journal of *Membrane Science, 352(1)*, 12-13.
31. Van den Bergh, J., Zhu, W., Gascon, J., Moulijn, J. A., & Kapteijn, F. (2008). Separation and permeation characteristics of a DD3R zeolite membrane. *Journal of Membrane Science, 316(1)*, 35-45.
32. Li, S., Martinek, J. G., Falconer, J. L., Noble, R. D., & Gardner, T. Q. (2005). High-pressure CO2/CH4 separation using SAPO-34 membranes. *Industrial & engineering chemistry research, 44(9)*, 3220.
33. Noack, M. M., Kölsch, P. P., Schäfer, R. R., Toussaint, P. P., & Caro, J. J. (2002). Molecular sieve membranes for industrial application: Problems, progress, solutions. *Chemical Engineering And Technology, 25(3)*, 221-230.

34. Carreon, M. A., Li, S., Falconer, J. L., & Noble, R. D. (2008). SAPO‐34 Seeds and Membranes Prepared Using Multiple Structure Directing Agents. *Advanced Materials, 20(4)*, 729.
35. Albrecht, E., Baum, G., Bellunato, T., Bressan, A., Dalla Torre, S., D'Ambrosio, C., … & Ullaland, O. (2003). VUV absorbing vapours in n-perfluorocarbons. *Nuclear Instruments and Methods in Physics Research Section A: Accelerators, Spectrometers, Detectors and Associated Equipment, 510(3)*, 268.
36. Xomeritakis, G., Nair, S., & Tsapatsis, M. (2000). Transport properties of alumina-supported MFI membranes made by secondary (seeded) growth. *Microporous and mesoporous materials, 38(1)*, 61.
37. Bhave, R. (2013). *Personal Communication.*
38. Rubel, A. M., & Stencel, J. M. (1996). Effect of pressure on NOx adsorption by activated carbons. *Energy And Fuels, 10(3)*, 708.
39. Bhave, R., Koros, W., DelCul, G., Jubin, R. (2011) Zeolite Membranes for the Capture of Krypton and Xenon from Voloxidation and Dissolve Off-gas. Unpublished proposal. *Oak Ridge National Laboratory, Oak Ridge, TN.*
40. Cox, L., & Blaszczak, R. (1999) *Nitrogen oxides (NOx) Why and How They are Controlled*. Environmental Protection Agency. DIANE Publishing. EP A-456/F-99-006R. 8.
41. Kawai, M., Nakamura, A., Nagasaka, T., & Hayashida, S. (2004). *U.S. Patent No. 6,752,851*. Washington, DC: U.S. Patent and Trademark Office.
42. Karwacki Jr, E. J., Golden, T. C., Ji, B., Motika, S. A., & Farris, T. S. (2007). *U.S. Patent No. 7,285,154*. Washington, DC: U.S. Patent and Trademark Office.

CHAPTER 2

ZEOLITE MEMBRANES FOR GAS SEPARATIONS

This chapter discusses the basic theory and equations for one-dimensional transport through zeolite membranes operated in dead-end filtration mode. This chapter also discusses in detail the structures of zeolites MFI, DDR, and SAPO-34.

2.1 Membrane Basics

A membrane is a semipermeable barrier that can separate multicomponent mixtures by selective transport through the semipermeable barrier. The transport of liquid and gas molecules through a membrane is called permeation, and membranes usually separate molecules based on molecular size, with smaller molecules permeating faster than larger molecules. A membrane that has different permeation rates for certain molecules is said to be permselective. In general there are two types of membranes processes: dead-end filtration and tangential flow filtration (TFF).[1]

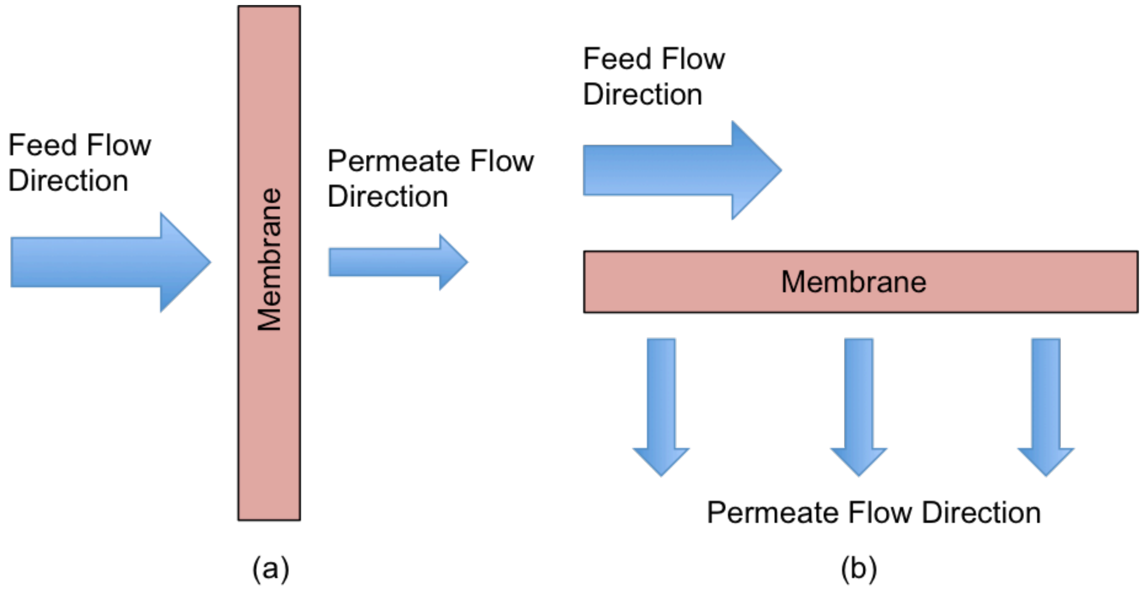

Figure 2.1: (a) Dead-end filtration, (b) tangential flow filtration (TFF) in cross-flow

In dead-end filtration, the direction of fluid flow entering the membrane is perpendicular to the membrane surface, but in tangential flow filtration the direction of the fluid flow entering the membrane is tangential to the surface of the membrane. The fluid that passes through the membrane is the filtrate (also called permeate), and in the case of TFF the fluid that does not pass through the membrane is the retentate. It is important to note that for TFF the permeate partial pressure or permeate concentration decreases along the length of the membrane unlike dead-end filtration, which is constant across the entire membrane area. Most industrial filtration processes use TTF because the tangential flow prevents fouling of the membrane. Therefore, TTF is operated continuously for longer periods of time compared to dead-end filtration, which is more likely to be operated as a batch process because the filter cake must be removed more frequently. Additionally, TTF usually employs many hollow tubular membranes operating in parallel that can be scaled up relatively easily to include a large amount of membrane area per unit volume compared to dead-end filtration membranes.[1] For hollow tubular membranes used in gas separations, the feed is usually fed into the hollow tube so permeate flows to the shell side.[2]

Also, for zeolite membranes synthesized on permeable supports (such as α-alumina and porous stainless steel) the zeolite membrane is usually positioned facing the feed side to prevent concentration polarization in the support layer.[3,4] Concentration polarization occurs when the concentration of permeating molecules becomes depleted at membrane surface and non-permeating molecules become concentrated at the membrane surface (called a "polarization layer"), thus decreasing flux through the membrane. If the polarization layer becomes concentrated above the solubility limit of the non-permeate molecules, the non-permeating molecules precipitate and form a gel or cake on the membrane surface, thus fouling the membrane and decreasing the flux even more.[1]

2.2 Mechanisms of Membrane Transport

Generally, there are four different mechanisms of transport for liquid and gas molecules through a membrane. The four mechanisms are: bulk flow through pores (also called viscous flow), diffusion through pores, restricted diffusion through pores, and solution diffusion through dense membranes. For gases, there are also two other special cases of transport through porous membranes: Knudsen diffusion and surface diffusion.[1,5]

Bulk flow occurs when the pores are much larger than the molecules and is governed by the continuity equation and equations of motion from fluid mechanics.[1,6] Gas transport through the α-alumina discs (used to support the zeolites membranes in this research) is bulk flow because the pore diameters (~300 nm) are much larger than the gas molecule kinetic diameters (≤ 0.55 nm). Bulk flow is driven by an external force, usually a pressure gradient and/or gravity. Diffusion through porous and nonporous membranes can be modeled with a modified version of Fick's first law of diffusion where the driving force is differences in fugacity, activity, chemical potential, concentration, or partial pressure across the membrane thickness. Transport through zeolites membranes occurs by restricted pore diffusion (also called molecular sieving), and transport through nonporous membranes occurs by solution-diffusion. In the solution-diffusion mechanism, the molecules on the feed side absorb into the membrane, diffuse across the membrane thickness, and then desorb on the filtrate side. Knudsen diffusion occurs when the mean free path of the diffusing molecules is greater than the pore diameter and is discussed in more detail in Section 2.5.[1] Surface diffusion occurs when the molecules adsorb on onto the inner surface of the pores and then travel through the pores by successively desorbing and adsorbing onto adjacent adsorption sites across the length of the membrane. Surface diffusion can be reverse-selective based on molecular size because larger molecules can adsorb more strongly and out-compete the smaller molecules for adsorption sites.[5]

2.3 Zeolite Membrane Permeance and Selectivity

The transmembrane flux for a single-component feed across a membrane is

$$N = \frac{P_M}{l_M}\left(P_F - P_P\right) \tag{2.1}$$

where N is the steady-state molar transmembrane flux, P_M is the permeability of the membrane, l_M is the thickness of the membrane, P_F is the feed pressure, and P_P is the permeate pressure. Equation 2.1 is a modified version of Fick's first law that takes into account molecular sorption and desorption in the membrane and external-fluid boundary layer or film mass-transfer resistances at the membrane surface, all represented in the permeability coefficient. Equation 2.1 can be further simplified by combining the permeability and membrane length into a single coefficient

$$\overline{P}_M = \frac{P_M}{l_M} \tag{2.2}$$

where $\overline{P}_M$ is the permeance of the membrane. Thus, the general expression for the transmembrane flux of any component i is

$$N_i = \overline{P}_{M_i}\left(Driving\ Force\right) \tag{2.3}$$

where the "Driving Force" is usually written as the difference in partial pressure or concentration of component i between the feed and permeate sides of the membrane. For a single-component feed gas and a pressure driving force, Equation 2.3 becomes

$$N = \overline{P}_M\left(P_F - P_P\right) = \overline{P}_M \Delta P_{drop} \tag{2.4}$$

where ΔP_{drop} is the pressure drop between the feed and permeate sides of the membrane.[1]

We can derive Equation 2.1 for a zeolite membrane using a modified version of Fick's first law of diffusion and the concentration profile across the membrane represented in Figure 2.2.

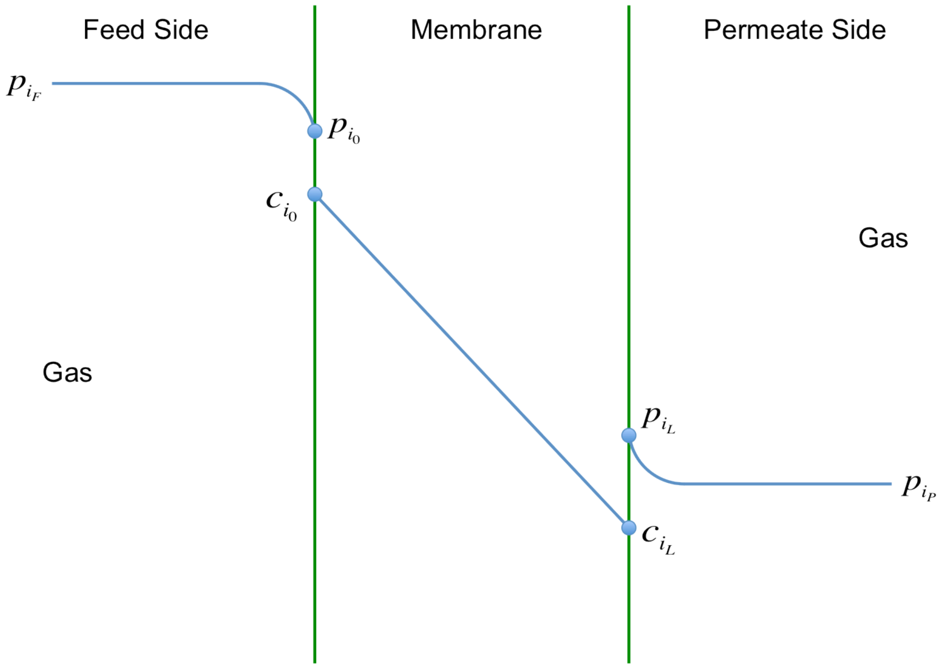

Figure 2.2: Concentration profile of through zeolite membrane.[1]

Based on Fick's second law of diffusion and assuming steady-state, we know the concentration profile through the membrane in Figure 2.2 is linearly decreasing from the feed side to the permeate side. Therefore, the steady-state transmembrane flux through the zeolite membrane is:

$$N_i = \frac{D_i}{l_M}\left(c_{i_L} - c_{i_0}\right) \tag{2.5}$$

where D_i is the molecular diffusivity of component i through the membrane, c_{i_0} is the concentration of component i in membrane at the upstream membrane surface, and c_{i_L} is the concentration of component i in the membrane at the downstream membrane surface. The concentrations c_{i_0} and c_{i_L} can be related to p_{i_0} and p_{i_L} by Henry's Law, which is a linear relationship that assumes the partial pressure directly adjacent to the membrane surface on both sides (p_{i_0} and p_{i_L}) is in thermodynamic equilibrium with the concentration in the membrane at the gas-membrane interface on both sides (c_{i_0} and c_{i_L}). Thus, Henry's Law gives

$$H_{i_0} = \frac{c_{i_0}}{p_{i_0}} \tag{2.6}$$

$$H_{i_L} = \frac{c_{i_L}}{p_{i_L}} \tag{2.7}$$

where H_{i_0} and H_{i_L} are Henry's constants and represent the solubility of component *i* in the membrane. Also, assuming that Henry's constant is not a function of total pressure and the temperature is constant and the same on both sides of the membrane:

$$H_{i_0} = H_{i_L} = H_i \tag{2.8}$$

Substituting in Equations 2.6, 2.7, and 2.8 into Equation 2.5 gives the total molar transmembrane flux.

$$N_i = \frac{H_i D_i}{l_M}\left(p_{i_L} - p_{i_0}\right) \tag{2.9}$$

Finally, assuming that any external-mass transfer resistances are negligible means $p_{i_F} = p_{i_0}$ and $p_{i_P} = p_{i_L}$ and gives

$$N_i = \frac{H_i D_i}{l_M}\left(p_{i_F} - p_{i_P}\right) \tag{2.10}$$

where p_{i_F} is the partial pressure of component *i* in the feed and p_{i_P} is the partial pressure of component *i* in the permeate. Equation 2.10 is exactly equal to Equation 2.1 for a single-component mixture, which means the permeance is

$$\frac{H_i D_i}{l_M} = \frac{P_{M_i}}{l_M} = \overline{P}_{M_i} \tag{2.11}$$

and the permeability is

$$P_{M_i} = H_i D_i \tag{2.12}$$

Therefore, the permeability for component *i* is equal to the product the Henry's constant and the diffusivity for component *i*. Also, for membranes operating in parallel the effective permeance is equal to the sum of all the membranes permeances:[1]

$$\overline{P}_{M_i,effective} = \sum_{1}^{n} \overline{P}_{M_i n} \tag{2.13}$$

where $\overline{P}_{M_i,effective}$ is the combined permeance of all the membranes in parallel for component *i*, called the effective permeance. For membranes operating in series, the inverse of the effective permeance is equal to the sum of all the inverse membrane permeances:[1]

$$\overline{P}_{M_i,effective} = \sum_{1}^{n} \frac{1}{\overline{P}_{M_i n}} \tag{2.14}$$

Therefore, for a zeolite membrane synthesized on a support layer the effective permeance is

$$\frac{1}{\overline{P}_{M_i,effective}} = \frac{1}{\overline{P}_{M_i,zeolite}} + \frac{1}{\overline{P}_{M_i,\sup port}} \tag{2.15}$$

where $\overline{P}_{M_i,zeolite}$ is the permeance of the zeolite membrane and $\overline{P}_{M_i,\sup port}$ is the permeance of the support layer. Also, including the zeolite defects as a membrane in series with the zeolite membrane yields

$$\frac{1}{\overline{P}_{M_i,effective}} = \frac{1}{\theta \overline{P}_{M_i,defects} + \left(1-\theta\right)\overline{P}_{M_i,zeolite}} + \frac{1}{\overline{P}_{M_i,\sup port}} \tag{2.16}$$

where θ is the fractional coverage of defects on the zeolite membrane surface given by

$$\theta = \frac{A_{defects}}{A_{zeolite} + A_{defects}} \tag{2.17}$$

where $A_{defects}$ is the area covered by the zeolite membrane defects and $A_{zeolite}$ is the area of the defect free zeolite membrane. If the permeance of the support layer is much larger than the permeance of the zeolite membrane and zeolite defects (which is usually true for small pore zeolites) such that[3]

$$\frac{1}{\theta \overline{P}_{M_i,defects} + (1-\theta)\overline{P}_{M_i,zeolite}} >> \frac{1}{\overline{P}_{M_i,\sup port}} \tag{2.18}$$

then Equation 2.16 becomes

$$\overline{P}_{M_i,effective} \approx \theta \overline{P}_{M_i,defects} + (1-\theta)\overline{P}_{M_i,zeolite} \tag{2.19}$$

Also, if the there are no membrane defects or if there are very few defects that are small in size then θ is essentially zero and Equation 2.19 becomes

$$\overline{P}_{M_i,effective} \approx \overline{P}_{M_i,zeolite} \tag{2.20}$$

Therefore, for a relatively defect free zeolite membrane synthesized on a porous support with a much larger permeance, the effective permeance is approximately equal to the zeolite membrane permeance. In this research, all permeances are reported are effective permeances, which, by this analysis, are approximately equal to the zeolite membrane permeance.

The separation factor (also called permselectivity or selectivity) of component A over component B in a multi-component feed through a membrane is defined as

$$\alpha_{A,B} = \frac{y_A/x_A}{y_B/x_B} \tag{2.21}$$

where y_A is the mole fraction of A in the permeate, x_A is the mole fraction of A in the feed, y_B is the mole fraction of B in the permeate, and x_B is the mole fraction of B in the feed.

For a single component feed or equilmolar binary feed ($x_A = x_B$), the separation factor is the ratio of the component fluxes:

$$\alpha_{A,B} = \frac{N_A}{N_B} = \frac{y_A}{y_B} = \frac{\frac{H_A D_A}{l_M}\left(x_A P_F - y_A P_P\right)}{\frac{H_B D_B}{l_M}\left(x_B P_F - y_B P_P\right)} \tag{2.22}$$

If the permeate pressure is low compare to the feed pressure then $x_A P_F >> y_A P_P$ and $x_B P_F >> y_B P_P$ then Equation 2.22 becomes

$$\alpha_{A,B}^{Ideal} = \frac{H_A D_A}{H_B D_B} = \frac{P_{M_A}}{P_{M_B}} = \frac{\overline{P}_{M_A}}{\overline{P}_{M_B}} \tag{2.23}$$

where $\alpha_{A,B}^{Ideal}$ is called the ideal separation factor, ideal permselectivity, or ideal selectivity. Equation 2.23 is also valid for single-component fluxes with the same feed pressure and low permeate pressure compared to the feed pressure ($P_F >> P_P$). An excellent membrane has a high permeance and selectivity for the desired component(s), and based on Equation 2.23 a high selectivity is achieved when the component solubility ratio (H_A/H_B) and/or diffusivity ratio (D_A/D_B) are high.[1]

2.4 Knudsen Diffusion through Zeolite Membrane Defects

Knudsen diffusion occurs when the mean free path of the permeating molecules is greater than the membrane pore diameters, which causes the permeating molecules to collide with the membrane pore walls more than other molecules in the mixture.[7] The mean free path of a gas molecule is the average distance a molecule travels before colliding with another molecule and is derived from kinetic theory for an ideal gas:[8]

$$\lambda = \frac{k_B T}{\sqrt{2}\pi d^2 P} \tag{2.24}$$

where k_B is the Boltzmann constant, T is the absolute temperature in Kelvin, d is the diameter of the gas molecules, and P is the total pressure.[8] For zeolite membranes and a gas feed, Knudsen diffusion usually dominates the flux through membrane defects and is modeled by a modified version of Fick's first law:[1,3]

$$N_i = \frac{D_{e_i}}{l_M}\left(c_{i_L} - c_{i_0}\right) \tag{2.25}$$

where D_{e_i} is the effective diffusivity of component i through the membrane defects. If the total pressure on both sides of the membrane is equal then there is no bulk flow, and if the ideal gas law is valid for component i and the temperature is equal on both sides of the membrane then the concentration can be related to the partial pressure at the gas-membrane interface by the ideal gas law:

$$c_{i_L} = \frac{c_M}{P} p_{i_L} = \frac{p_{i_L}}{RT} \tag{2.26}$$

$$c_{i_0} = \frac{c_M}{P} p_{i_0} = \frac{p_{i_0}}{RT} \tag{2.27}$$

where c_M is the total concentration in the membrane, P is the total pressure, R is the universal gas constant, and T is temperature. Then Equation 2.25 becomes

$$N_i = \frac{D_{e_i} c_M}{l_M P}\left(p_{i_L} - p_{i_0}\right) = \frac{D_{e_i}}{l_M RT}\left(p_{i_L} - p_{i_0}\right) \tag{2.28}$$

The effective diffusivity is

$$D_{e_i} = \frac{\varepsilon}{\tau}\left(\frac{1}{\left(1/D_i\right) + \left(1/D_{K_i}\right)}\right) \tag{2.29}$$

where ε is the volume fraction of defects in the zeolite membrane, τ is the tortuosity of the defects, and D_{K_i} is the Knudsen diffusivity of component *i*. If Knudsen diffusion dominates then there is very little molecular diffusion through the membrane defects and Equation 2.29 becomes

$$D_{e_i} = \frac{\varepsilon}{\tau} D_{K_i} \tag{2.30}$$

The Knudsen diffusivity through a straight cylindrical pore is derived from kinetic theory and gives

$$D_{K_i} = \frac{d_p \bar{v}_i}{3} \tag{2.31}$$

where d_p is the pore diameter of the defects and $\bar{v}_i$ is the average molecule velocity:

$$\bar{v}_i = \sqrt{\frac{8RT}{\pi M_i}} \tag{2.32}$$

where M_i is the molecular weight of the diffusing molecule. Combining Equations 2.38, 2.30, 2.31, and 2.32 gives the flux through zeolite membrane defects:

$$N_i \frac{\varepsilon d_p}{3\tau l_M RT} \sqrt{\frac{8}{\pi M_i RT}} \left(p_{i_L} - p_{i_0} \right) \tag{2.33}$$

where the permeance is

$$\bar{P}_{M_i} = \frac{\varepsilon d_p}{3\tau l_M} \sqrt{\frac{8}{\pi M_i RT}} \tag{2.34}$$

and the permeability is

$$P_{M_i} = \frac{\varepsilon d_p}{3\tau} \sqrt{\frac{8}{\pi M_i RT}} \tag{2.35}$$

A key difference between Equations 2.10 and 2.35 is the flux, permeance, and permeability for Knudsen diffusion do not depend on the solubility (Henry's constant) of permeating molecules in the membrane because there is no sorption in Knudsen diffusion. Substituting Equation 2.35 into Equation 2.23 gives the ideal selectivity of Knudsen diffusion:

$$\alpha_{A,B}^{Ideal} = \frac{\overline{P}_{M_A}}{\overline{P}_{M_B}} = \sqrt{\frac{M_B}{M_A}} \tag{2.36}$$

Equation 2.36 shows that the ideal selectivity of Knudsen diffusion is the square root of the ratio of the component molecular weights, which for similar sized molecules is close to unity.[1] For example, the ideal selectivity for Knudsen diffusion of an equilmolar Kr/Xe mixture is 1.25. Therefore, Knudsen diffusion through zeolite defects is highly undesirable because the selectivity is very low, and minimizing the membrane defects is essential to obtaining a zeolite membrane with high Kr/Xe selectivity.

2.5 Membrane Lag Time

The derivations in Sections 2.1, 2.2, and 2.3 were all performed under the assumption of steady-state flux, but in reality the flux is only steady-state after a certain "lag time" when the permeating molecules diffusive through the entire membrane thickness and reach the permeate side. During this unsteady-state flux period, the concentration profile through the membrane thickness is an exponential decay curve that shifts to a linear decay profile as time approaches the end of the lag time. In general, the characteristic diffusion time scale for a component *i* diffusing a distance L is

$$\tau = \frac{L^2}{D_i} \tag{2.37}$$

where τ is the characteristic diffusion time scale, which is an estimate of the time it takes for component i to diffuse distance L. When the pressure on permeate side of a membrane is initially zero and the membrane does not contain any permeating components (the membrane is "empty"), the time is takes for the permeating components to travel through the membrane thickness after the feed contacts the membrane surface at time zero is called the lag time. For a closed permeate volume with an initial pressure equal to zero, the lag time is

$$\tau_{lag} = \frac{L^2}{6D_i} \tag{2.38}$$

where τ_{lag} is the lag time for component i. The lag time can also be determined by the time when there is an inflection point in the permeate pressure vs. time plot for a membrane (Figure 2.3).

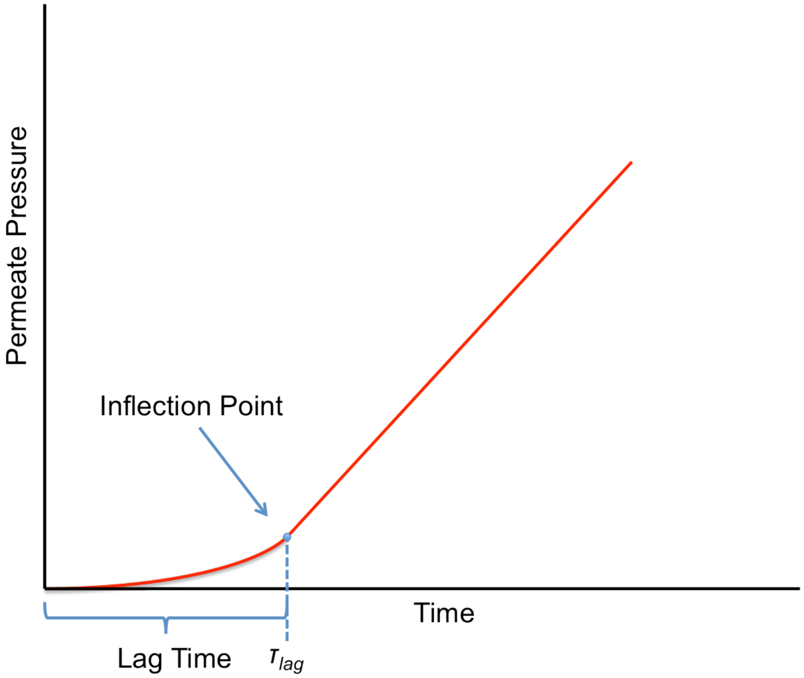

Figure 2.3: Permeate vs. time plot showing membrane lag time.[9]

For a single-component feed gas the lag time can be determined from the inflection point and, if the membrane thickness is known, the component diffusivity can be calculated with Equation 2.38. Also, for diffusivities that are very high the lag time will be very short or essentially zero, unless the membrane is very thick. This is normally the case for Knudsen diffusion as well because Knudsen diffusivity is usually large compared to molecular diffusivity.[9]

2.6 MFI Structure

MFI has an anisotropic channel network and pores composed of 10 T-atoms. The pore sizes are 5.1x5.5 Å along the [100] plane and 5.3x5.6 Å along the [010] plane.[10]

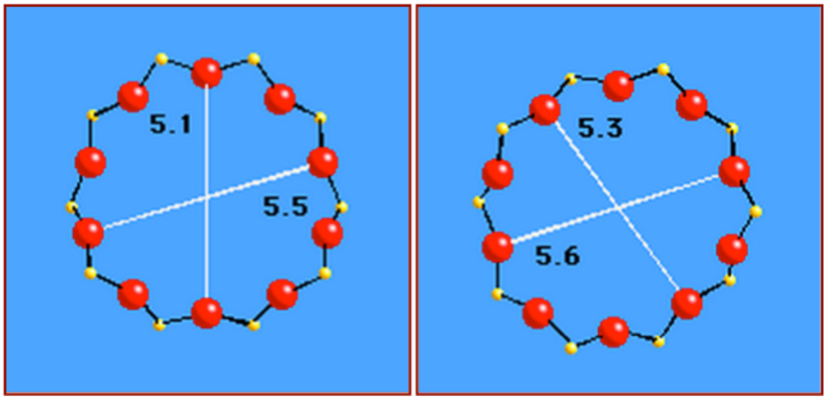

Figure 2.4: MFI pore dimensions in Angstroms (Å) viewed along [100] plane (left) and [010] plane (right). Silicone atoms are red and oxygen atoms are yellow. Image reproduced from reference [10].

There are two types of zeolites with an MFI framework: ZSM-5, which is an aluminosilicate (chemical formula $Al_nSi_{96-n}O_{192}$, $n < 27$), and silicalite-1, which is pure silica (chemical formula $Si_{96}O_{192}$).[10,11] MFI zeolites have a Si/Al molar ratio greater than

10 and are hydrophobic and organophilic.[11] In this research, MFI always refers to the pure-silica type. MFI has three orientations: *a*-orientation parallel to the [100] plane, *b*-orientation parallel to the [010] plane, and *c*-orientation.[11] MFI's channel network is connected in 3 dimensions, where 5.3x5.6 Å straight channels along the *b*-axis and perpendicularly intersect the 5.1x5.5 Å sinusoidal channels along the *a*-axis. MFI has an occupiable and accessible volume of 10% for a water molecule.[10,11] Typical MFI crystals are coffin- or octagonal-shaped.[12]

To achieve a high *p*-xylene (kinetic diameter 5.8 Å) to *o*-xylene (kinetic diameter 6.8 Å) selectivity (discussed in Chapter 1.5), MFI membranes are synthesized with the *b*-direction facing the membrane surface to utilize the 5.3x5.6 Å straight channels for *p*-xylene/*o*-xylene separation.[13] Also, MFI has been studied for separating CO_2 form CH_4 for natural gas processing because it strongly adsorbs CO_2. However, since the kinetic diameters of CO_2 and CH_4 are smaller than the MFI pore sizes, MFI selectivity for CO_2/CH_4 is usually because the main mechanism of separation is competitive adsorption in the membrane and not molecular sieving.[14] Typical ZSM-5 membrane selectivities for CO_2/CH_4 mixtures have ranged from 2.4 to 5.5 at room temperature, and, for pure-silica MFI membranes, a CO_2/CH_4 ideal selectivity of about 10 was reported by Lovallo et al.[14,15]

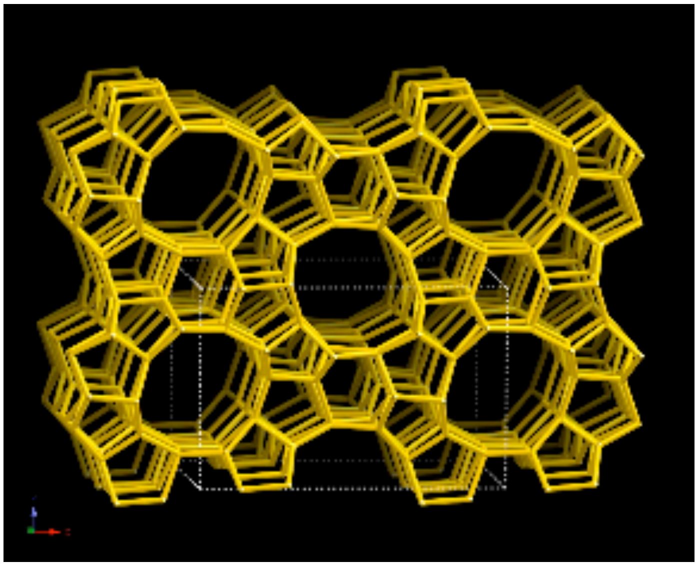

Figure 2.5: MFI structure viewed along [010] plane (b-axis). Image reproduced from reference [10].

2.7 DDR Structure

DDR (also called DD3R or deca-dodecasil 3R) has an anisotropic channel network and 3.6x4.4 Å pores composed of 8 T-atoms.[16] DDR is pure silica (chemical formula $Si_{120}O_{240}$), hydrophobic, and organophilic.[17]

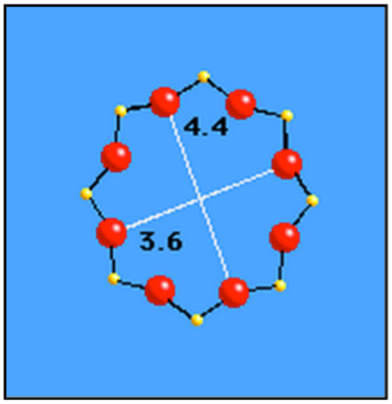

Figure 2.6: DDR pore dimensions in Angstroms (Å) viewed normal to [001] plane. Silicone atoms are red and oxygen atoms are yellow. Image reproduced from reference [16].

DDR's channel network is connected in 2 dimensions, where the 3.6x4.4 Å channels only intersect along two dimensions. DDR has an occupiable volume 11% for a water molecule and an accessible volume of 9% for a water molecule.[16] DDR crystals can have several different sizes and shapes (such as octahedral, hexagonal, and prismatic) depending the synthesis procedure.[18] Due to DDR's small pore size and strong adsorption for CO_2, DDR membranes can achieve high CO_2/CH_4 selectivities (>100) for the separation of CO_2/CH_4 mixtures (previously discussed in Chapter 1.5).

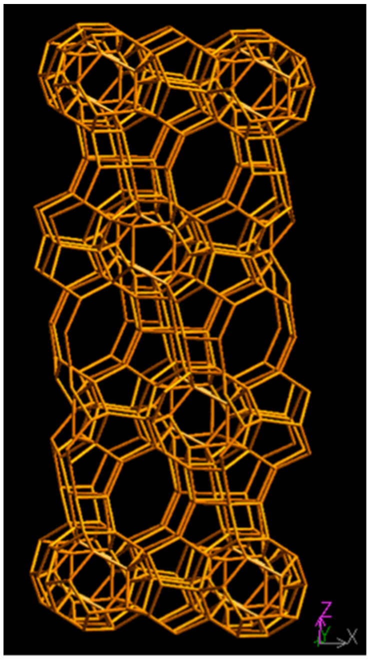

Figure 2.7: DDR structure viewed along [010] plane. Image reproduced from reference [16].

2.8 SAPO-34 Structure

SAPO-34 has an isotropic chabazite (CHA) framework with 3.8x3.8 Å pores composed of 8 T-atoms.[19] However, the pores size can be variable due to the flexibility of the CHA framework and has been shown to stretch to 4.3 Å in diameter. SAPO-34 is a silicoaluminophosphate (SAPO) zeolite with a low Si/Al molar ratio (usually < 1) and a chemical formula of $(Si_xAl_yP_z)O_2$ ($x = 0.01–0.98$, $y = 0.01–0.60$, $z = 0.01–0.52$, where $x + y + x = 1$).[19,20]

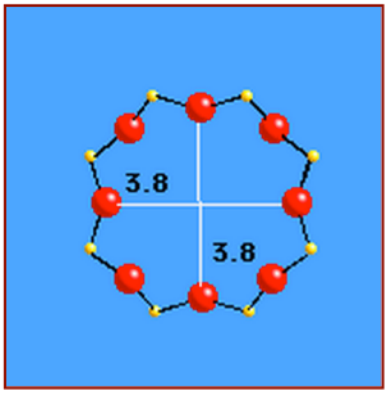

Figure 2.8: SAPO-34 pore dimensions in Angstroms (Å) viewed normal to [001] plane. Silicone atoms are red and oxygen atoms are yellow. Image reproduced from reference [19].

SAPO-34's channel network is connected in 3 dimensions with 3.8x3.8 Å channels. The accessible and occupiable volume for a water molecule in SAPO-34 is 17%.[19] SAPO-34 crystals are cubical and can very in size depending on the synthesis procedure. SAPO-34 is hydrophilic and adsorbs H_2O and CO2 strongly.[21] Due to SAPO-34's small pore size and strong adsorption for CO_2, SAPO-34 membranes can achieve high CO_2/CH_4 selectivities (> 100) for the separation of CO_2/CH_4 mixtures (previously discussed in Chapter 1.5).

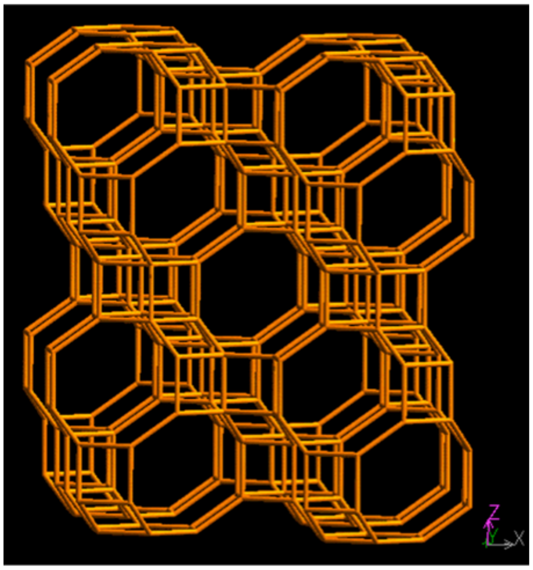

Figure 2.9: SAPO-34 (CHA) structure viewed along the [010] plane. Image reproduced from reference [19].

2.9 References

1. Seader, J. D. (2006). *Separation process principles*. Wiley. 2nd Edition. 496-531.
2. Brown, A. (2013). *Personal Communication*.
3. Cybulski, A., & Moulijn, J. A. (Eds.). (2005). *Structured catalysts and reactors*. CRC Press. 705.
4. Avila, A. M., Funke, H. H., Zhang, Y., Falconer, J. L., & Noble, R. D. (2009). Concentration polarization in SAPO-34 membranes at high pressures. *Journal of Membrane Science, 335(1)*, 32-36.
5. Husain, Shabbir. (2006). *Mixed Matrix Dual Layer Hollow Fiber Membranes For Natural Gas Separation*. (Doctoral dissertation). Retrievied from SMARTech Georgia Tech Theses and Dissertations. 2-3. http://hdl.handle.net/1853/16178.
6. Bird, R. B., Stewart, W. E., & Lightfoot, E. N. (2007). *Transport phenomena*. Wiley. 75-82.

7. Welty, J. R., Wicks, C. E., Rorrer, G., & Wilson, R. E. (2009). *Fundamentals of momentum, heat, and mass transfer*. John Wiley & Sons. 420-422.
8. Loeb, L. B. (2004). *The kinetic theory of gases*. Courier Dover Publications. 51.
9. Rutherford, S. W., & Do, D. D. (1997). Review of time lag permeation technique as a method for characterisation of porous media and membranes. *Adsorption, 3(4)*, 283-312.
10. International Zeolite Association. (2007). Database of Zeolite Structures: Framework Type MFI. Retrieved October 21, 2013, from http://izasc.ethz.ch/fmi/xsl/IZA-SC/ftc_fw.xsl?-db=Atlas_main&-lay=fw&-max=25&STC=MFI&-find.
11. Kassaee, Mohamad. (2012). *Internal surface modification of zeolite MFI particles and membranes for gas separation*. (Doctoral dissertation). Retrievied from SMARTech Georgia Tech Theses and Dissertations. 4. http://hdl.handle.net/1853/44906.
12. Zeng, G., Chen, C., Li, D., Hou, B., & Sun, Y. (2013). Exposure of (001) planes and (011) planes in MFI zeolite. *CrystEngComm*.
13. Nair, S., Lai, Z., Nikolakis, V., Xomeritakis, G., Bonilla, G., & Tsapatsis, M. (2001). Separation of close-boiling hydrocarbon mixtures by MFI and FAU membranes made by secondary growth. *Microporous and Mesoporous Materials*, *48(1)*, 225.
14. Li, S., Martinek, J. G., Falconer, J. L., Noble, R. D., & Gardner, T. Q. (2005). High-pressure CO2/CH4 separation using SAPO-34 membranes. *Industrial & Engineering Chemistry Research, 44(9)*, 3220.

15. Lovallo, M. C., Gouzinis, A., & Tsapatsis, M. (1998). Synthesis and characterization of oriented MFI membranes prepared by secondary growth. *AIChE Journal, 44(8)*, 1903.
16. International Zeolite Association. (2007). Database of Zeolite Structures: Framework Type DDR. Retrieved October 21, 2013, from http://izasc-mirror.la.asu.edu/fmi/xsl/IZA-SC/ftc_fw.xsl?-db=Atlas_main&-lay=fw&STC=DDR&-find.
17. Himeno, S., Tomita, T., Suzuki, K., Nakayama, K., Yajima, K., & Yoshida, S. (2007). Synthesis and permeation properties of a DDR-type zeolite membrane for separation of CO2/CH4 gaseous mixtures. *Industrial & Engineering Chemistry Research, 46(21)*, 6989.
18. Zhengzhi, Z., McCarley, K. C., Drese, J. H., & Nair, S. (2013). Zeolite DDR Submicron Crystals and Membranes for Gas Separation: Synthesis and Post-Treatment. Unpublished manuscript. *Georgia Institute of Technology, Atlanta, GA*.
19. International Zeolite Association. (2007). Database of Zeolite Structures: Framework Type CHA. Retrieved October 21, 2013, from http://izasc-mirror.la.asu.edu/fmi/xsl/IZA-SC/ftc_fw.xsl?-db=Atlas_main&-lay=fw&STC=CHA&-find.
20. Lok, B. M., Messina, C. A., Patton, R. L., Gajek, R. T., Cannan, T. R., & Flanigen, E. M. (1984). Silicoaluminophosphate molecular sieves: another new class of microporous crystalline inorganic solids. *Journal of the American Chemical Society, 106(20)*, 6092-6093.

21. Poshusta, J. C., Tuan, V. A., Falconer, J. L., & Noble, R. D. (1998). Synthesis and permeation properties of SAPO-34 tubular membranes. *Industrial And Engineering Chemistry Research, 37(10)*, 3924-3929.

CHAPTER 3

EXPRIMENTAL METHODS

This chapter outlines the materials and experimental procedures used for this research. The chapter also describes the lab apparatuses used to fabricate and test the zeolite membranes.

3.1 Porous α-Alumina Disc Polishing

MFI and SAPO-34 membranes were synthesized on porous α-alumina discs. One face of each disc was polished to obtain a smooth shiny surface. A continuous zeolite membrane only grew on the polished disc surface. The α-alumina discs were manufactured by CoorsTek Inc. with CoorsTek ADS-96R alumina material. The discs had a 1.00 in. diameter, 0.045 in. thickness, and 20% porosity. The discs were polished with a Petrolap (Buehler) wet polisher at 150 rpm for 2 min with Grit 400/P 800 Carbimet® (Buehler) silicon carbide grinding paper. During polishing, the grinding paper was continuously with tap water, and the alumina discs were rotated 90° every 30 s until 2 min elapsed. After polishing, each discs was sonicated in DI water for 5 to 10 seconds and then dried at 60 to 70 °C.

3.2 MFI Membrane Synthesis on α-Alumina Discs

MFI membranes were synthesized by in-situ hydrothermal synthesis on α-alumina discs. The MFI synthesis solution had a molar composition of 49 TEOS:0.28 TPAOH:180 H_2O, where the silica source was tetraethyl orthosilicate (TEOS, 98%, Sigma-Aldrich) and the structure directing agent was tetra-n-propylammonium hydroxide (TPAOH, 1 M in water, Alfa Aesar). The synthesis procedure is given below.[1]

1. Mix 1 M TPAOH and DI water at room temperature.
2. Add TEOS drop wise to the solution while stirring at room temperature.
3. Stir the solution for 5 h at room temperature (aging step).
4. Place one polished α-alumina disc into a 23 mL Teflon-lined Parr acid digestion vessel. Use a Teflon stand to hold up the disc vertically in the acid digestion vessel.
5. Fill the acid digestion vessel with synthesis solution until the solution completely submerges the disc. Do not completely fill the acid digestion vessel with synthesis solution. Fill the vessel just above the top of the vertical discs and no more than 1/3rd full. Close the acid digestion vessel.
6. Heat the acid digestion at 150 °C for 17 h (hydrothermal synthesis step).
7. After 17 h, wait for the acid digestion vessel to cool to room temperature.
8. Remove the α-alumina disc and wash the membrane (polished side) with DI water for 1 to 2 minutes.
9. Dry the membrane for 12 h at 60 to 70 °C.
10. Calcine the membrane in stagnant air at 550 °C for 6 h with a heating a cooling rate of 0.5 °C/min.

3.3 Amorphous Carbon Membrane Synthesis

The amorphous carbon membranes and membrane module were synthesized and designed at Oak Ridge National Lab (ORNL) using a proprietary procedure; therefore, the synthesis procedure is not reported in this thesis. The carbon membranes were synthesized on alumina coated porous stainless steel support tubes. The porous stainless steel tubes had 50 cm^2 of area, a pore size ~ 4 μm, and a thickness ~ 0.5 mm. The alumina coating had a pore size ~ 5 nm and a thickness ~ 5 um.[2]

3.4 DDR Seed Crystal Synthesis

DDR crystals were synthesized to seed the α-alumina support tubes for DDR membrane synthesis. The DDR seed crystal synthesis solution had a molar composition of 6 ADA:100 SiO_2:8000 H_2O:100 KF (potassium fluoride, 99%, Sigma-Aldrich). The silica source was LUDOX® SM-30 colloidal silica (30 wt. % suspension in water, Sigma-Aldrich), and the structure directing agent was 1-adamantylamine (1-ADA, 97%, Sigma-Aldrich). The synthesis procedure is given below.[3]

1. Mix LUDOX® SM-30 colloidal silica and DI water. Keep the mixture stirring.
2. Add ADA and stir for 5 min at room temperature.
3. Add KF and stir for 2 h at room temperature.
4. Fill a 23 mL Teflon-lined Parr acid digestion vessel no more than 1/3rd full with synthesis solution, add 5 mg of ball-milled purified DDR crystals (previously synthesized with this procedure without synthesis solution seeding before hydrothermal synthesis), and close the vessel.
5. Heat the acid digestion vessel at 150-160 °C for 6-8 h (hydrothermal synthesis step).
6. Wait for the acid digestion vessel to cool to room temperature.

7. Centrifuge the seeds in fresh DI water several times until the solution pH is approximately 7.
8. Dry and ball-mill the purified seeds into a fine powder.

3.5 DDR Membrane Synthesis on α-Alumina Tubes

DDR membranes were synthesized on the outer surface of porous α-alumina support tubes. The α-alumina tubes were manufactured by Ceramco Inc. The tubes had a 0.435 in. outer diameter, 0.055 in. thickness, 1.00 to 1.57 in. lengths, 30 % porosity, and 200 to 300 nm pore sizes. The tubes were not polished. The synthesis solution molar composition was 6 ADA:100 SiO_2:4000 H_2O:x KF ($x = 60$ to 100). All chemicals are the same as the DDR seed crystal synthesis. The synthesis procedure is given below.[3]

1. Mix LUDOX® SM-30 colloidal silica and DI water. Keep the mixture stirring.
2. Add ADA and stir for 5 min at room temperature.
3. Add KF and stir for 2 h at room temperature.
4. Seed the α-alumina tubes by dip-coating them in a 2g/L DDR seed crystal solution in DI water. Repeat the dip-coating two times, for a total of three seed layers.
5. Place one tube vertically in a 23 mL Teflon-lined Parr acid digestion vessel. Use a Teflon stand to hold up the tube vertically in the acid digestion vessel, and block the tube ends with Teflon tape so synthesis solution does not contact the interior surface of the tube.
6. Fill the acid digestion vessel with synthesis solution until the solution completely submerges the tube. Do not completely fill the acid digestion vessel with

synthesis solution. Fill each vessel just above the top of the vertical tube and no more than 1/3rd full. Close the acid digestion vessel.

7. Heat the acid digestion vessel at 160 °C for 36 h (hydrothermal synthesis step).
8. Wait for the acid digestion vessel to cool to room temperature.
9. Remove the α-alumina tub and wash the membrane with DI water.
10. Dry the membrane for 1 day at 60 °C.
11. Calcine the membrane in stagnant air at 700 °C for 8 h with a heating a cooling rate of 0.5 °C/min.
12. After calcination, one end of the tube was sealed with Scotch-Weld™ 5 min epoxy (3M) and the other end was sealed to the opening a Swagelok ¼'' to ¾'' fitting with epoxy such that the tube was covering the opening of the fitting on the ¾'' side. The fitting was then attached to a ¾'' Swagelok tee. The finished DDR membranes module is pictured in Figure 3.1.

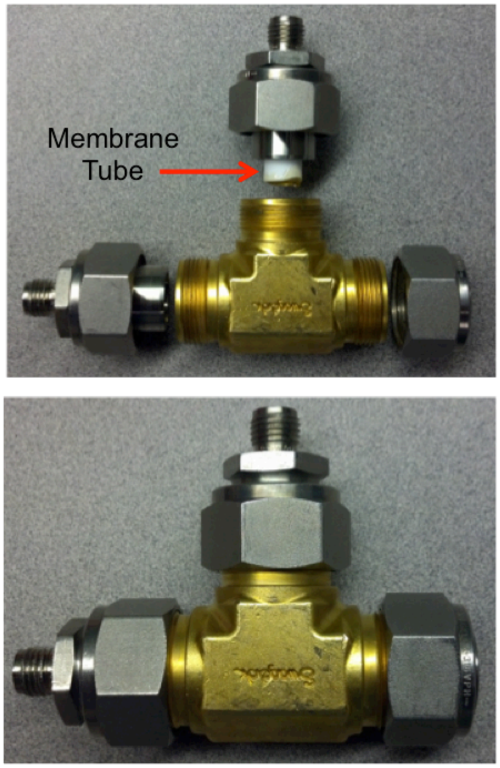

Figure 3.1: DDR membrane module disassembled (top) and assembled (bottom).

3.6 SAPO-34 Seed Crystal Synthesis

SAPO-34 crystals were synthesized to seed the α-alumina support discs for SAPO-34 membrane synthesis. The SAPO-34 seed crystal synthesis solution had a molar composition of 1.0 Al_2O_3:1.0 P_2O_5:x SiO_2:1.0 TEAOH:y DPA:z H_2O ($x = 0.3$ or 0.32, $y =$ 0.8 or 1.6, and $z = 52$ or 77). The alumina source was aluminum isoproxide (Al(i-C_3H_7O), 98%, Sigma-Aldrich); the phosphorous source was phosphoric acid (H_3PO_4, 35 wt. % in water, Sigma-Aldrich); the silica source was LUDOX® SM-30 colloidal silica (30 wt. % suspension in water, Sigma-Aldrich); the structure directing agents were tetraethylammonium hydroxide (TEAOH, 35 wt. % in water, Sigma-Aldrich) and dipropylamine (DPA, 99%, Sigma-Aldrich). The synthesis procedure was largely adapted from Li et al. and is given below.[4]

1. Mix aluminum isoproxide and DI water at room temperature. Keep the solution stirring at room temperature.
2. Add phosphoric acid drop wise to the solution.
3. Stir the solution for 3 h.
4. Add LUDOX® SM-30 colloidal silica drop wise to the solution.
5. Stir the solution for 3 h.
6. Add TEAOH drop wise to the solution.
7. Stir the solution for 0.5 hour.
8. Add DPA drop wise to the solution.
9. Stir the solution for at least 3 days at room temperature (aging step).
10. Fill a 23 mL Teflon-lined Parr acid digestion vessel no more than 1/3rd full with synthesis solution.
11. Heat the acid digestion vessel at 210 °C for 6-24 h (hydrothermal synthesis step)
12. Wait for the acid digestion vessel to cool to room temperature.
13. Centrifuge the seeds in fresh DI water at least five times until the supernatant is clear.
14. Dry the seeds for 12 hours at 60-70 °C
15. Grind the seeds into a fine powder with a mortar and pestle.
16. Calcine seeds at 390 °C for 10 h, 550 °C for 6 h, or 700 °C for 6 h with a heating and cooling rate of 1.0 °C/min or 0.5 °C/min.
    a. SAPO-34 seed crystals that were used to seed SAPO-34 membranes were not calcined prior to seeding. SAPO-34 seeds were calcined for characterization and pressure decay cell measurements.

3.7 SAPO-34 Membrane Synthesis on α-Alumina Discs

SAPO-34 membranes were synthesized on the polished surface of α-alumina discs. The SAPO-34 membrane synthesis solution had a molar composition of 1.0 Al_2O_3:1.0 P_2O_5:x SiO_2:1.0 TEAOH:y DPA:z H_2O ($x = 0.3$ or 0.32, $y = 0.8$ or 1.6, $z = 77$ or 150). All chemicals are the same as the SAPO-34 seed crystal synthesis. Several seeding and calcination techniques were used to determine which techniques produced the highest quality membranes. The synthesis procedure was largely adapted from Li et al. is given below.[4]

1. Mix aluminum isoproxide and DI water at room temperature. Keep the solution stirring at room temperature.
2. Add phosphoric acid drop wise to the solution.
3. Stir the solution for 2 to 5 h.
4. Add LUDOX® SM-30 colloidal silica drop wise to the solution.
5. Stir the solution for 0.5 to 3 h.
6. Add TEAOH drop wise to the solution.
7. Stir the solution for 0.5 h.
8. Add DPA drop wise to the solution.
9. Stir the solution for at least 4 days at room temperature (aging step).
10. Make a Make a 5 wt. % SAPO-34 seed solution in DI water. Sonicate the seed solution for 0.5 h.
11. Alumina discs seeding techniques:

   a. Technique 1 (Cotton Swab Rubbing): Apply 3 drops of seed solution to the polished disc surface and spread the solution over the disc surface with a cotton swab. Dry the seeded disc at 60-70 °C.
   b. Technique 2 (Finger Rubbing): Apply 3 drops of seed solution to the polished disc surface and spread/rub the solution over the disc surface with your finger (wearing gloves). Dry the seeded disc at 60-70 °C.
   c. Technique 3 (Finger Rubbing Multiple Layers): Apply 3 drops of seed solution to the polished disc surface and spread/rub the solution over the disc surface with your finger (wearing gloves). Dry the seeded disc at 60-70 °C. After the seed layer dries, forcefully rub the dried seed layer with your finger to remove the dried seeds from the disc surface. Repeat the procedure 2 more times, except for the last time do not remove the dried seed layer.

12. Place one disc vertically in a 23 mL Teflon-lined Parr acid digestion vessel. Use a Teflon stand to hold up the disc vertically in the acid digestion vessel.
13. Fill the acid digestion vessel with synthesis solution until the solution completely submerges the disc. Do not completely fill the acid digestion vessel with synthesis solution. Fill each vessel just above the top of the vertical disc and no more than 1/3rd full. Close the acid digestion vessel.
14. Heat the acid digestion vessel at 210 °C for 6 to 24 h (hydrothermal synthesis step).
15. Wait for the acid digestion vessel to cool to room temperature.
16. Remove the α-alumina disc and wash the membrane with DI water for 1 to 2 min.

17. Dry the membrane for 8 to 24 h at 60 to 70 °C.
18. Membrane Calcination techniques:[1]
    a. Technique 1: Calcine the membrane in stagnant air at 390 °C for 10 h or 550 °C for 6 h with a heating a cooling rate of 1.0 °C/min or 0.5 °C/min.
    b. Technique 2: Treat the membrane with UV-light by placing it approximately 1 cm from a UV-light source for 24 h (energy output at 1 cm distance was approximately 8.5 W/cm^2). Then Calcine the membrane in stagnant air at 390 °C for 10 h, 550 °C for 6 h, or 700 °C for 6 h with a heating a cooling rate of 1.0 °C/min or 0.5 °C/min.

3.8 Polydimethylsiloxane Membrane Treatment to Seal Defects

A 5 wt. % polydimethylsiloxane (PDMS) solution in hexanes (isomer mixture, Fisher Scientific) was used to seal SAPO-34 disc membrane and DDR tube membrane defects after the membranes were calcined. Slygard® 184 (Dow Corning) was used to make the PDMS solution with a resin to cross-linker weight ratio of 5.7 (volume ratio 1.72). The PDMS sealing procedure is given below.[3,5,6,7]

1. Dissolve PDMS in hexanes at room temperature.
2. Reflux the solution for 6 h in a 90 °C oil bath while stirring. The reflux apparatus is pictured in Figure 3.2.

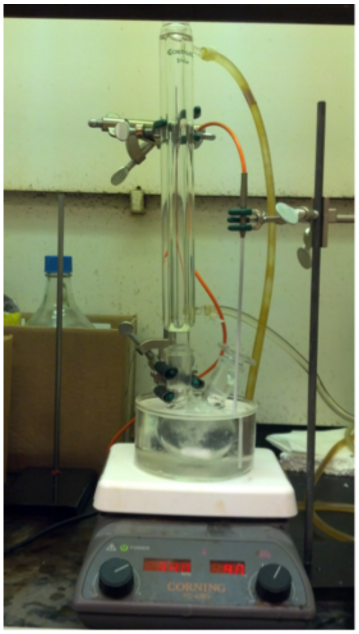

Figure 3.2: PDMS reflux apparatus.

3. Let the solution cool to room temperature. Keep the solution stirring.
4. DDR tube sealing procedure:
    a. Filter the PDMS solution with a 0.2 μm filter.
    b. Level the DDR membrane.
    c. Fill the DDR membrane module with PDMS solution so the outer surface of the tube/membrane is completely submerged. Leave the solution open to the atmosphere (do not cap the inlet of the DDR membrane module).
    d. Apply a vacuum (displacement 4.5 m^3/h, speed 3.5 m^3/h, ultimate pressure $2x10^{-3}$ mbar) to the inside of the tube for 10 min.
    e. Remove the PDMS solution and wash the membrane with hexanes.
    f. Cure the membrane at 80 °C for 4 h stagnant air.
5. SAPO-34 disc sealing procedures (sealing apparatus pictured in Figure 3.3):
    a. Multiple Layer Procedure:

    i. Filter the PDMS solution with a 0.2 μm filter.
    ii. Insert the membrane in a disc permeation cell with the membrane side facing up (facing feed side). Seal the membrane into the cell with Viton® O-rings (Marco Rubber, -26 to 240 °C).
    iii. Level the permeation cell and close the sweep gas valve.
    iv. Fill the feed side of the permeation cell with PDMS solution. Leave the solution open to the atmosphere (do not cap the inlet of the permeation cell).
    v. Apply a vacuum (displacement 4.5 m^3/h, speed 3.5 m^3/h, ultimate pressure $2x10^{-3}$ mbar) to the inside of the tube for 1 min.
    vi. Remove the PDMS solution and repeat the procedure 2 more time.
    vii. Remove the membrane and wash it with hexanes.
    viii. Cure the membrane in a vacuum oven at 100 °C for 12 h.

b. Single Layer Procedure:
    i. Filter the PDMS solution with a 0.2 μm filter.
    ii. Insert the membrane in a disc permeation cell with the membrane side facing up (facing feed side). Seal the membrane into the cell with Viton® O-rings (Marco Rubber, -26 to 240 °C).
    iii. Level the permeation cell and close the sweep gas valve.
    iv. Fill the feed side of the permeation cell with PDMS solution. Leave the solution open to the atmosphere (do not cap the inlet of the permeation cell).

v. Apply a vacuum (displacement 4.5 m^3/h, speed 3.5 m^3/h, ultimate pressure $2x10^{-3}$ mbar) to the inside of the tube for 30 sec.

vi. Remove the PDMS solution.

vii. Remove the membrane and wash it with hexanes.

viii. Cure the membrane in a vacuum oven at 100 °C for 12 h.

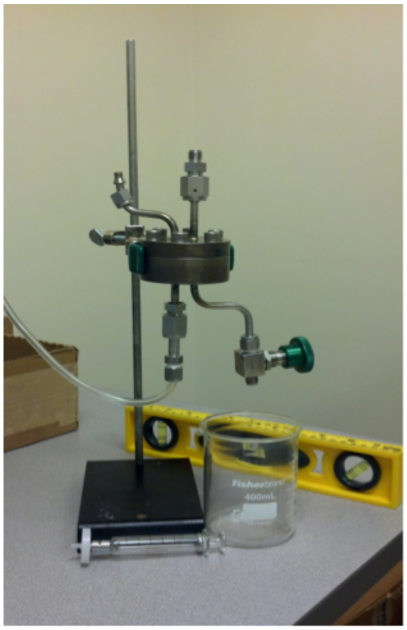

Figure 3.3: PDMS disc sealing apparatus.

3.9 Permeation Testing

The membranes were tested in single-gas permeation units, and two essentially identical permeation units were built for testing. The only significant design difference was one permeation unit was rated for flammable gas permeation, while the other unit was only rated for inert gas permeation. To test the DDR membrane modules (Figure 3.1) and carbon membrane module in dead-end filtration mode, the retentate lines were capped. The discs membranes were also tested in dead-end filtration mode, and the disc permeation cell (Figure 3.4) was designed and fabricated in-house. The disc permeation cell had feed and permeate lines (no retentate or sweep gas lines) and the membranes were sealed in the cell with Viton® O-rings (Marco Rubber, -26 to 240 °C). After sealing the 1 in. α-alumina disc in the disc permeation cell, the effective disc diameter was 0.75 in. and the actual membrane permeation area was 0.44 in^2. The permeation units were built using Swagelok® tubing and fittings and leaked tested (with a nonporous metal disc installed in the disc permeation cell) to ensure the leak rates for the units and disc permeation cell were < 0.05 GPU (leak test results in Appendix A). The flow diagram of the permeation units is given in Appendix B. Before permeation testing, each membrane was calcined or re-calcined (except PDMS treated membranes and carbon membranes) and degassed under vacuum (displacement 4.5 m^3/h, speed 3.5 m^3/h, ultimate pressure $2x10^{-3}$ mbar) to remove adsorbed molecules (primarily H_2O, N_2, O_2, and CO_2 in the atmosphere) from the membrane pores. MFI and SAPO-34 membranes were stored under vacuum or in He after calcination to prevent adsorption of CO_2 and H_2O, respectively. MFI and DDR membranes were degassed under vacuum at room temperature for 2 h and 0.5 h, respectively. SAPO-34 membranes were degassed under vacuum at 100 to 200 °C for 10 to 30 min. Carbon membranes were degassed under vacuum at 100 to 150 °C for 30 to 60 min. All membranes were degassed before testing each gas, unless otherwise noted.

To measure the permeance through the membranes, gas was feed into the tube permeation modules/discs permeation cell at a constant feed pressure and temperature, and the gas that permeated through membranes was collected in a 50 cm^3 cylinder located inside the permeation oven. Except for MFI, all membranes were facing the feed side when installed and tested. The initial pressure in the gas collection cylinder was approximately 0 pisa. The pressure of the collection cylinder was measured overtime (one measurement per second) and the number of measurements recorded depended on the membrane and gas being tested, but enough measurements were recorded to yield a linear fit of the recorded data with a correlation coefficient (R^2 value) of > 0.98 (usually ranged from 100 to 2000 measurements). Any pressure measurements recorded as the pressure equilibrated were truncated to yield a linear permeate pressure versus time plot. To calculate the effective permeance of the membrane layer and support layer, the permeate pressure versus time data were fit to a linear plot (MATLAB code used for the linear regression analysis of the permeation data is in Appendix C) and the slope of the plot (*dP/dt*) was used to calculate the molar flow rate (*dn/dt*) using the ideal gas law:

$$\frac{dn}{dt} = \frac{\left(dP / dt\right) V_C}{RT} \tag{3.1}$$

where V_C is the collection volume (includes 50 cm^3 collection cylinder, volume in tube permeation models/disc permeation cell, and volume in the permeate side tubing and fittings of the apparatus), R is the universal gas constant, and T is the absolute temperature. All test gases have a compressibility factor of approximately one at room temperature and atmospheric pressure.[8] Therefore, the ideal gas law is a valid model at the temperatures (-15 to 200 °C) and pressures (1 to 2 atm.) used for permeation testing. The molar transmembrane flux (N_{flux}) is

$$N_{flux} = \frac{\left(dn / dt\right)}{A_{membrane}} \tag{3.2}$$

where $A_{membrane}$ is the permeation area of the membrane. The effective permeance ($\overline{P}_{M,effective}$) is

$$\overline{P}_{M,effective} = \frac{N_{flux}}{\Delta P_{drop}} \tag{3.3}$$

where ΔP_{drop} is the transmembrane pressure drop given by

$$\Delta P_{drop} = \left(P_F - P_P\right) \tag{3.4}$$

where P_F is the feed pressure and P_P is the permeate pressure. The effective permeance is the combined permeance of the membrane and support layers

$$\frac{1}{\overline{P}_{M,effective}} = \frac{1}{\overline{P}_{M,membrane}} + \frac{1}{\overline{P}_{M,\sup port}} \tag{3.5}$$

where $\overline{P}_{M,membrane}$ is the permeance of the membrane layer and $\overline{P}_{M,\sup port}$ is the permeance of the support layer. All results are reported as effective permeance in gas permeation units (GPU, 1 GPU = 3.35×10^{-10} mol/m^2/s/Pa). Also, since the support permeance is much greater than the membrane permeance ($\overline{P}_{M,\sup port} >> \overline{P}_{M,membrane}$, except for MFI) the effective permeance is approximately equal to the membrane ($\overline{P}_{M,effective} \approx \overline{P}_{M,membrane}$); therefore, this study reports effective permeance results only. The ideal selectivity (α^{Ideal}) of pure species i and j at the same temperature and pressure is given by

$$\alpha^{Ideal} = \frac{N_{flux_i}}{N_{flux_j}} = \frac{\overline{P}_{M_i}}{\overline{P}_{M_j}} \tag{3.6}$$

The permeation units were built in lab ovens to perform supra-ambient testing, and the disc permeation cell and gas collection cylinder were submerged in a saltwater-ice cooling bath to perform sub-ambient testing. A feed coil was used during sub-ambient testing to facilitate heat transfer from the feed gas. The permeation unit with attached disc permeation cell and feed coil is pictured in Figure 3.4, and the disc permeation cell submerged in the cooling bath is also picture in Figure 3.4.

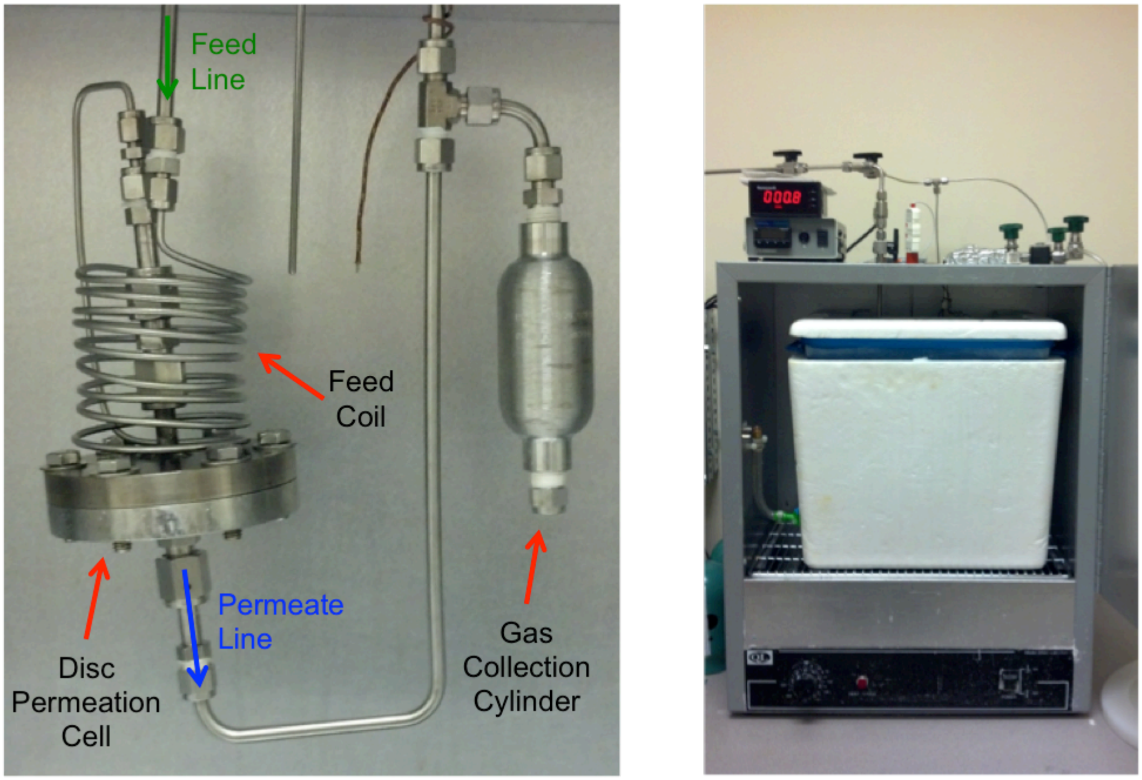

(a) (b)

Figure 3.4: (a) Disc permeation cell attached to feed coil and 50 cm^3 gas collection chamber. (b) Disc permeation cell submerge in cooling bath.

The feed pressure was measured with an Omega PX309 Series pressure transducer (0-200 psia range, 0.25% accuracy), the permeate pressure was measured with an Omega PX309 Series pressure transducer (0-30 pisa range, 0.25% accuracy), and the temperature was measured with an Omega Type K Chromega®-Alomega® exposed thermocouple (–270 to 1372 °C range, 0.75% accuracy above 0 °C). Feed pressure, permeate pressure, and temperature were recorded with a computer using an Omega USB data acquisition system and Omega's Personal DaqView Plus software. All test gases: H_2 (99.999%), CO_2

(99.999% or 99.99%), N_2 (99.999%), CH_4 (99.99%), He (99.999%), Ar (99.999 %), Xe (99.995%), Kr (99.9%), SF_6 (99.8%) were obtained from Airgas. A typical permeation testing procedure is given below.

1. Install the tube membrane module/disc permeation cell into permeation unit and open the valve (if there is one) to the 50 cm^3 gas collection cylinder.
2. Leak test the appropriate fittings with Snoop® (Sawagelok) leak detector while the apparatus is pressurized with helium or nitrogen gas at approximately 30 pisa. Tighten any leaks. If leaks persist, undo the fitting, apply Teflon tape to the threads, and then re-tighten.
3. Set the desired feed pressure with the regulator attached to the gas cylinder. Close the check valve.
4. Degas the membrane and entire permeation unit (all feed and permeate lines) under vacuum for the appropriate amount of time at the appropriate temperature.
5. Open the oven and cool the unit with a fan to the desired temperature. Keep the membrane under vacuum.
6. When the desired temperature has been reached and stabilizes, close the vacuum valve to the feed side and the feed valve to the tube membrane module/disc permeation cell. Keep the permeate side under vacuum.
7. Open the check valve and wait until the feed pressure stabilizes.
8. Begin recording measurements on the computer.
9. Quickly close the permeate valve directly after the permeate pressure transducer and open the feed valve to the tube membrane module/disc permeation cell.
10. Turn off the vacuum pump.

11. Record the appropriate number of measurements, then stop recording measurements on the computer and close the check valve.
12. Close the feed valve to the tube membrane module/disc permeation cell and purge the feed line (necessary for pressures > 1 atm).
13. Vacuum the entire permeation unit, set the desired temperature for the next test, and repeat Steps 6 to 12 if using the same gas. To test a different gas, repeat the procedure starting from Step 3.

3.10 Scanning Electron Microscopy Characterization

Scanning electron microscopy (SEM) was used to characterize the α-alumina support discs, MFI membranes, SAPO-34 seed crystals, and SAPO-34 membranes. SEM was used to visually determine seed crystal size, membrane quality, and membrane thickness. Three SEMs models were used: Hitachi SU8010 Cold Field Emission SEM, Hitachi S-800 Cold Field Emission SEM, and Zeiss LEO 1550 thermally-assisted field emission SEM. Images were acquired at accelerating voltages of 5 to 10 kV and if charging distorted images then the samples were coated with gold nanoparticles for 30 s using a Q150T ES Sputter Coater (Quorum Technologies).

3.11 X-Ray Diffraction Characterization

The MFI membranes, SAPO-34 seed crystals, and SAPO-34 membranes were characterized by a PANalytical X'Pert PRO X-ray diffractometer. Crystal (powder) and membrane X-ray diffraction (XRD) patterns were taken at 45 kV and 40 mA from a start angle of 4° to and end angle of 50°.

3.12 References

1. Kim, S.K. (2013). *Personal Communication.*
2. Bhave, R. (2013). *Personal Communication.*
3. Zhengzhi, Z., McCarley, K. C., Drese, J. H., & Nair, S. (2013). Zeolite DDR Submicron Crystals and Membranes for Gas Separation: Synthesis and Post-Treatment. Unpublished manuscript. *Georgia Institute of Technology, Atlanta, GA.*
4. Li, S., Carreon, M. A., Zhang, Y., Funke, H. H., Noble, R. D., & Falconer, J. L. (2010). Scale-up of SAPO-34 membranes for CO_2/CH_4 separation. *Journal of Membrane Science, 352(1)*, 7-13.
5. Husain, S. (2006). *Mixed matrix dual layer hollow fiber membranes for natural gas purification.* (Doctoral dissertation). Retrievied from SMARTech Georgia Tech Theses and Dissertations. http://hdl.handle.net/1853/16178.
6. Kassaee, M. (2013). *Personal Communication.*
7. Chiu, W. V., Park, I. S., Shqau, K., White, J. C., Schillo, M. C., Ho, W. S. W., ... & Verweij, H. (2011). Post-synthesis defect abatement of inorganic membranes for gas separation. *Journal of Membrane Science, 377(1)*, 182-190.
8. Air Liquide. (2013). Air Liquide Gas Encyclopedia. *Air Liquide.com.* Retrieved October 5, 2013 from http://encyclopedia.airliquide.com/encyclopedia.asp.

CHAPTER 4

RESULTS AND DISCUSSION

4.1 α-Alumina Disc Characterization

Porous α-alumina discs used to support the zeolite membranes were characterized by SEM and XRD. Figure 4.1 shows a typical disc surface before polishing and Figure 4.2 shows a typical disc surface after polishing.

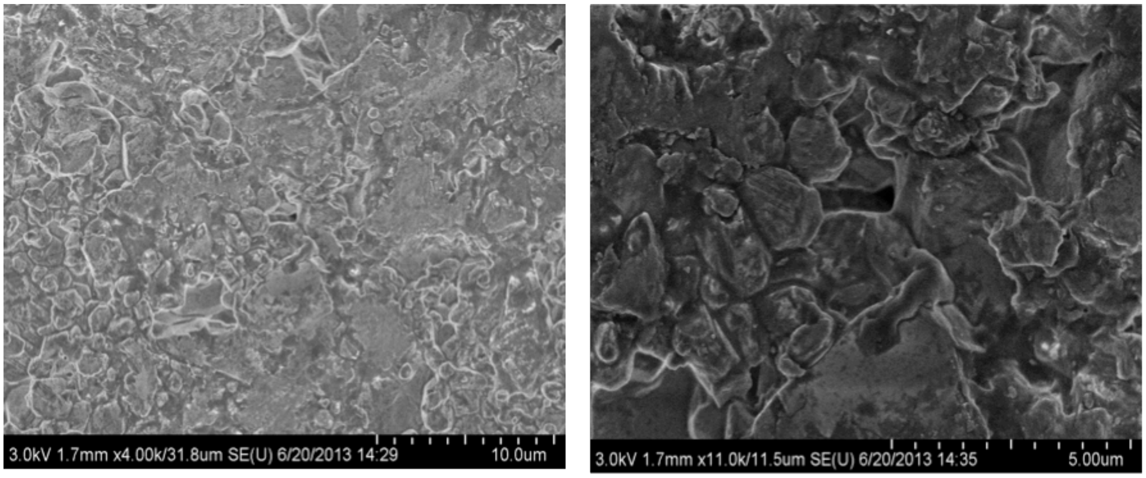

Figure 4.1: α-alumina disc surface before polishing.

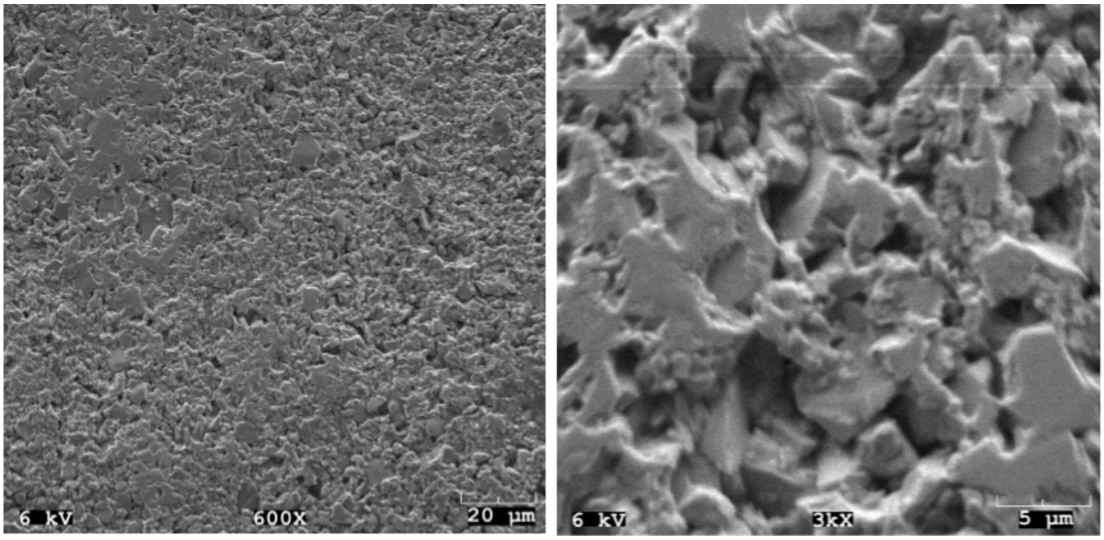

Figure 4.2: Polished surface of α-alumina disc.

Polishing the α-alumina disc levels the surface to make it very smooth and uniform. Polishing the disc also "activates" the disc surface by creating free hydroxyl (–OH) groups on the disc surface. Zeolite membranes preferentially grow on the polished surface because the hydroxyl groups form crystallization nucleation sites. This helps form a continuous zeolite membrane with fewer defects than zeolite membranes grown on unpolished alumina discs.[1] Figure 4.3 shows a typical α-alumina disc cross-section.

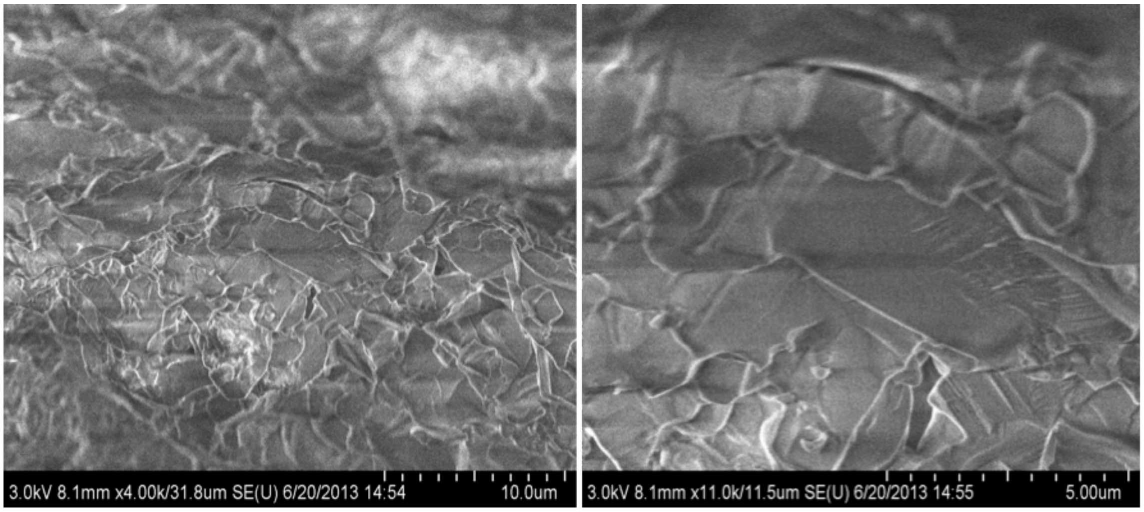

Figure 4.3: Cross-section of α-alumina disc.

Figures 4.1, 4.2, 4.3 show that the α-alumina discs have a sub-micron pore size (manufacture specifies ~ 300 nm) and do not have any large holes or cracks on the surface or through the discs. The XRD pattern of the α-alumina disc from 5° to 50° is given in Figure 4.4, and α-alumina has characteristic peaks at 26°, 35°, 38°, and 43°.[2]

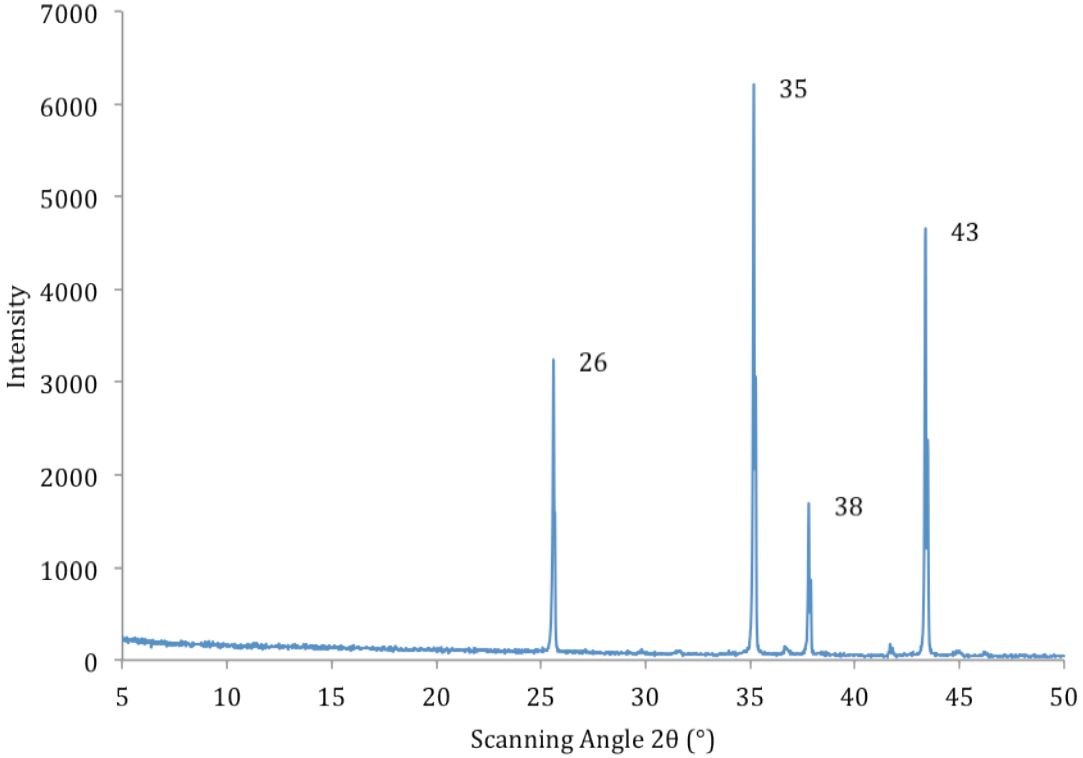

Figure 4.4: XRD pattern of α-alumina disc.

4.2 α-Alumina Disc Permeation

Two different α-alumina disk where polished and permeation tested without a zeolite membrane on the surface to determine the permeance through the zeolite support layer. Figure 4.5 shows the α-alumina permeances of H_2, He, CH_4, N_2, and CO_2 are greater than 1400 GPU for a 2 atm feed pressure between 25 and 100 °C. The permeance decreases from 25 °C to 100 °C decreases because the adsorption to alumina decreases as temperature increases.[3] The α-alumina disc has a CO_2/CH_4 ideal selectivity of 0.64 at 25 °C and 100 °C and an H_2/N_2 ideal selectivity of 3.2 at 25 °C and 100 °C. Although there is some adsorption and diffusion through the alumina disc, the main mechanism of transport is bulk flow, which leads to high permeances and low selectivities.

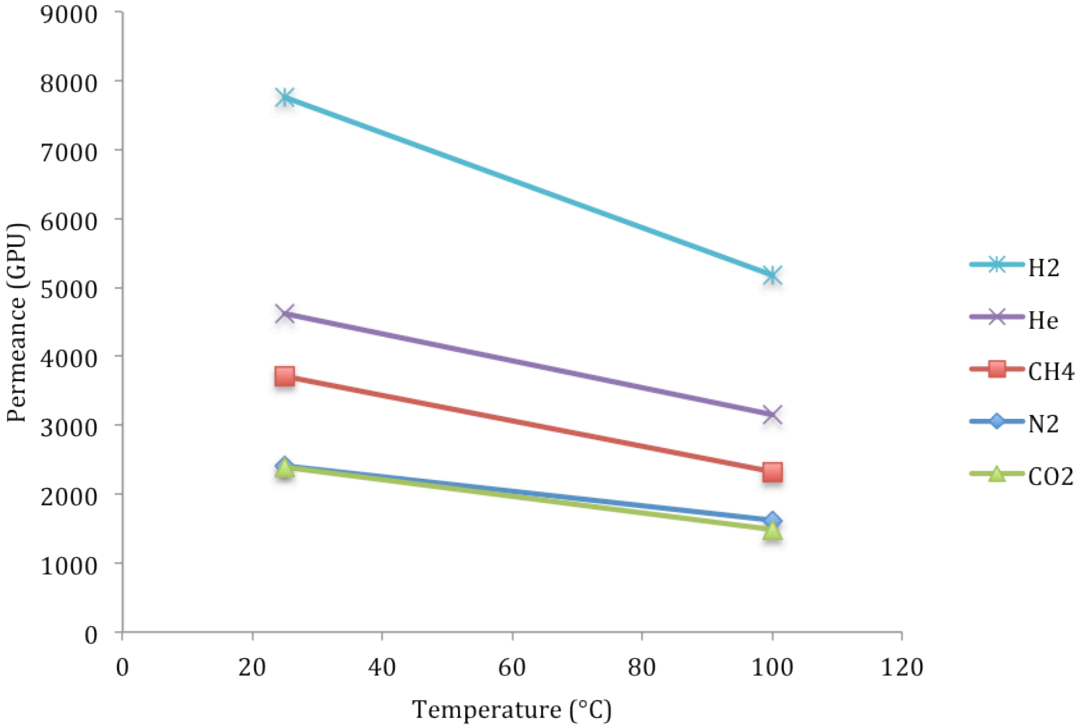

Figure 4.5: α-alumina disc permeance at 29.7 ± 0.8 psia average feed pressure and 23.8 ± 1.0 psi average pressure drop (95% confidence intervals).

Figure 4.6 shows the permeance of Kr and Xe through an α-alumina disc (different discs were tested in Figures 4.5 and 4.6). At 1 atm feed pressure, the permeances of Kr and Xe are greater than 850 GPU between 25°C and 175 °C. The decrease in permeance from 25 °C to 175 °C is contributed to decreasing Kr and Xe adsorption to α-alumina with increasing temperature. The average Kr/Xe ideal selectivity is 1.1 ± 0.029 (99% confidence interval) from 25 °C to 175 °C. Although Figures 4.5 and 4.6 are representative of permeation through a typical alumina disk used in this research, the permeance may vary between each disk depending on the manufacturing quality.

However, based on the disc quality assessment in Chapter 4.1, we do not expect the permeance between discs to vary significant.

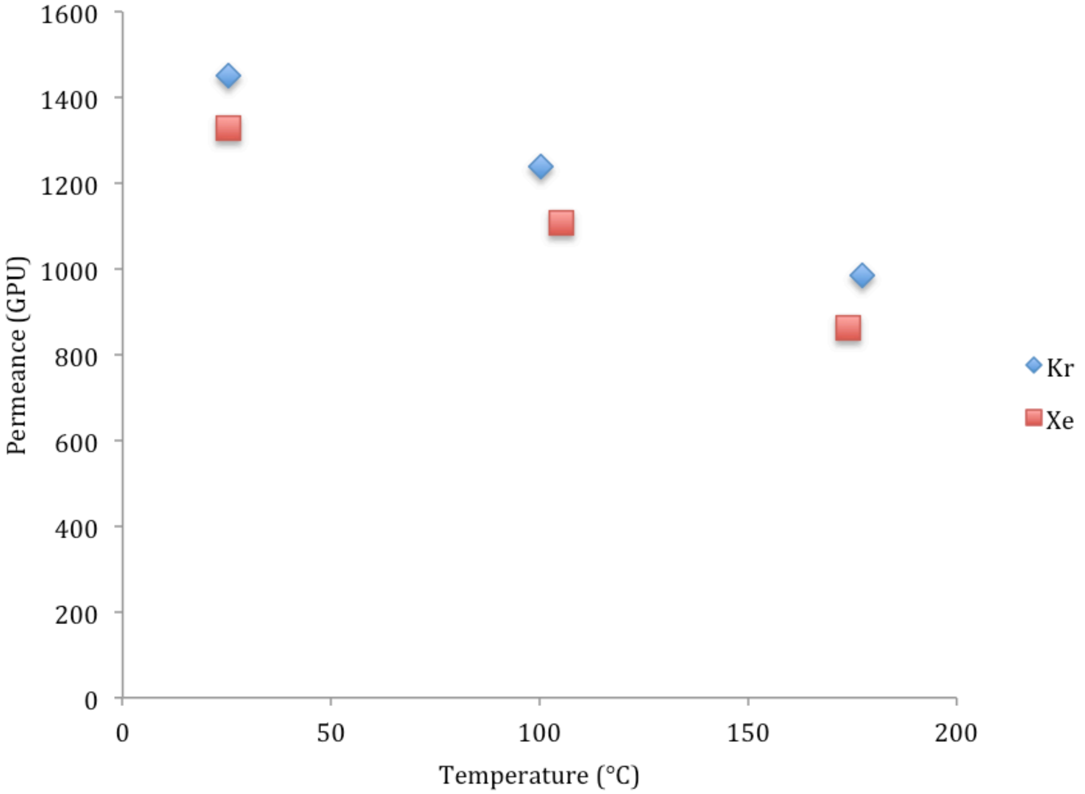

Figure 4.6: α-alumina disc permeance for Kr and Xe at 14.8 ± 0.2 psia average feed pressure and 13.6 ± 0.2 psi average pressure drop (95% confidence intervals).

4.3 MFI Membrane Characterization

MFI membranes were synthesized on α-alumina discs and characterized by SEM and XRD. Based on SEM and XRD results, the best quality MFI membrane was identified and used for permeation testing. SEM images showed the membrane was continuous and visually defect-free (Figure 4.7). The MFI membrane thickness was approximately 8 um based on SEM images of the membrane cross-section (Figure 4.8).

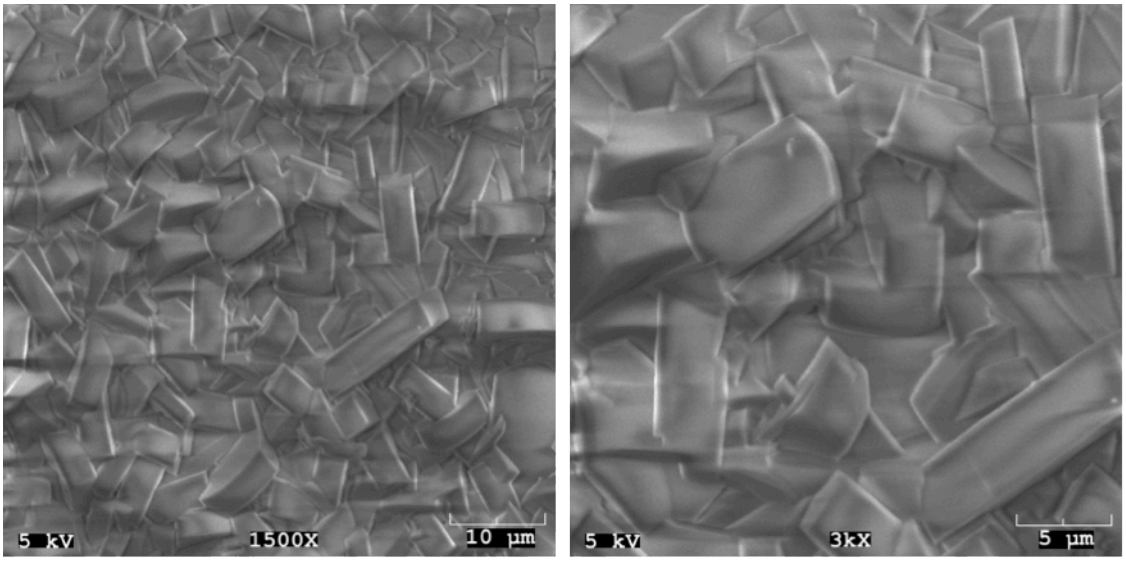

Figure 4.7: MFI membrane surface.

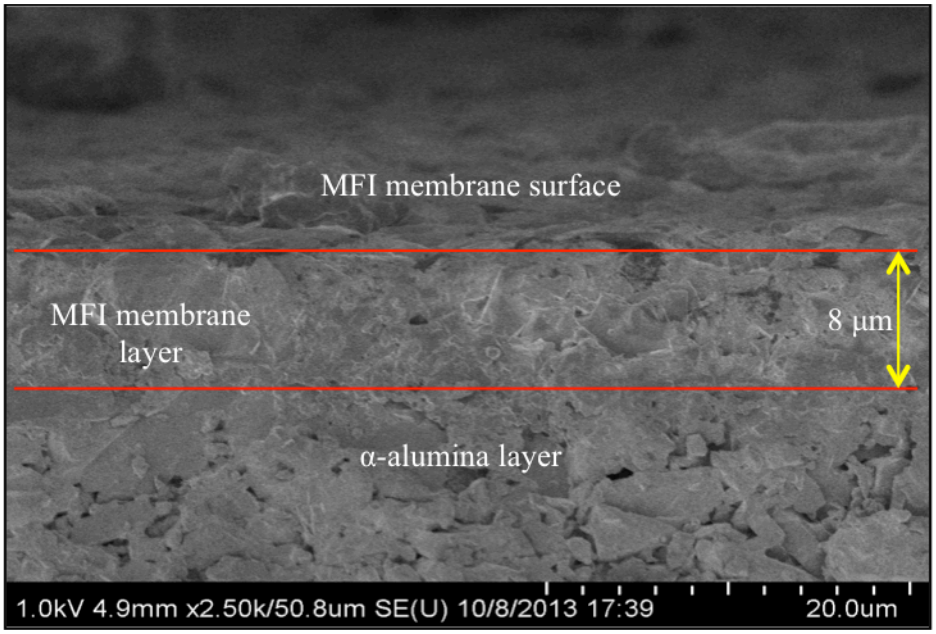

Figure 4.8: MFI membrane cross-section and thickness (~8 um).

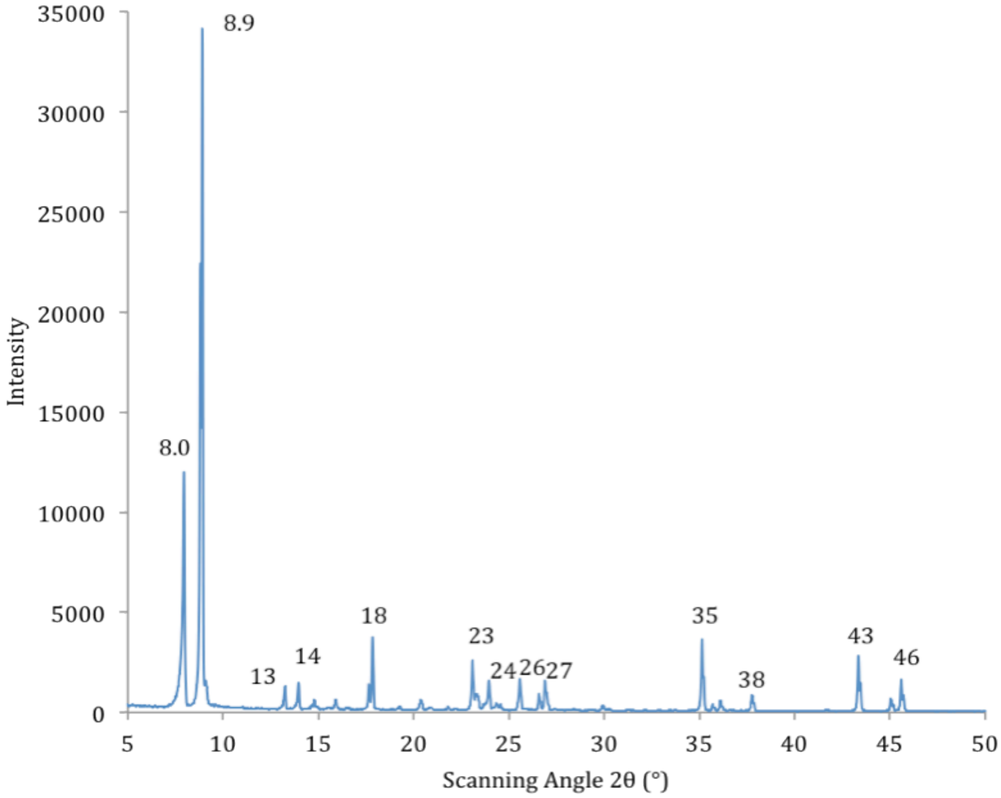

Figure 4.9: XRD pattern of MFI membrane (peaks at 26°, 35°, 38°, and 43° are from α-alumina support disc).

The XRD pattern of the MFI membrane (Figure 4.9) shows characteristic peaks MFI from 5° to 50°. The high intensity MFI peaks 8.0° and 8.9° compared to the α-alumina peaks (at 26°, 35°, 38°, and 43°) indicate the MFI membrane had a high degree of crystallinity.[4]

4.4 MFI Membrane Permeation

The MFI membrane characterized in Chapter 4.3 was permeation tested at 25 °C with a feed pressure of 2 atm.

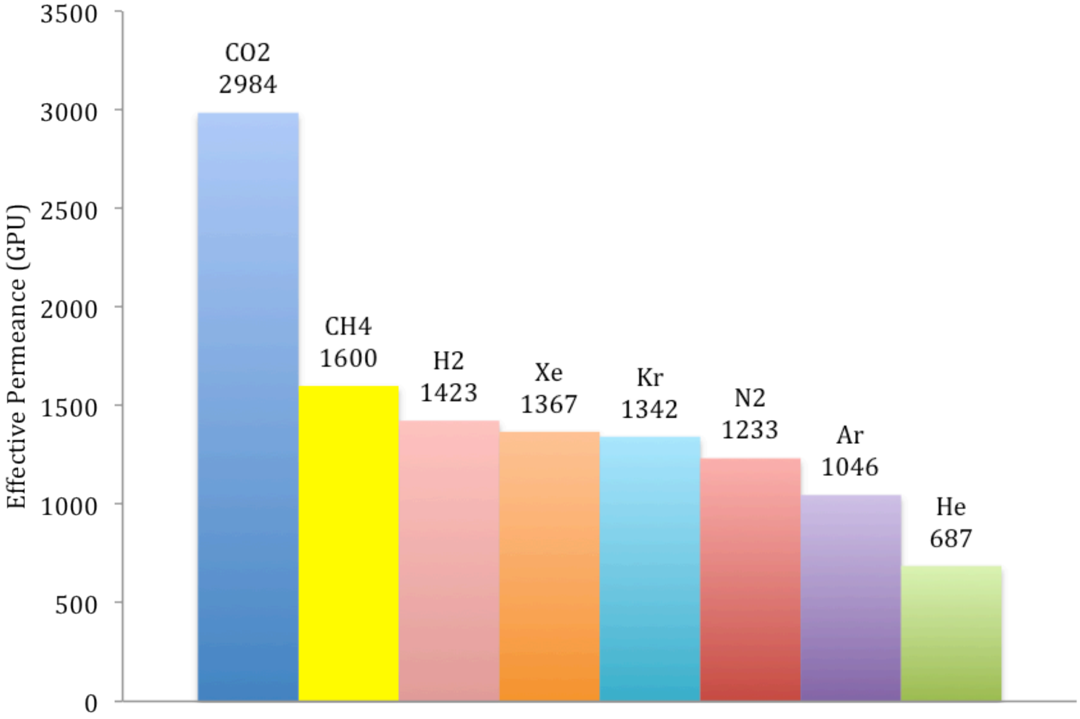

Figure 4.10: MFI membrane effective permeance at 30.2 ± 0.4 psia average feed pressure and 27.8 ± 0.6 psi average pressure drop and 25 °C (95% confidence intervals).

From Figure 4.10, the effective permeance of the MFI membrane is the same order of magnitude as the support layer permeance (Figures 4.5 and 4.6), so Equation 2.18 is invalid. Also, the zeolite membrane permeance for CO_2 and Kr cannot be calculated using Equations 2.15 because the effective permeances in Figure 4.10 are higher than the support permeances in Figures 4.5 and 4.6, which would give negative permeances for CO_2 and Kr and is not physically possible. This may be caused by differences in the permeances of CO_2 and Kr between the α-alumina discs tested in Figures 4.5 and 4.6 and the α-alumina disc used to support the MFI membrane. However, the combined support and MFI membrane selectivity can still be calculated by taking a ratio of the effective permeances in Figure 4.10. Based on this approach, the CO_2/CH_4 ideal selectivity is 1.87 and Kr/Xe ideal selectivity is 0.982. The CO_2/CH_4 selectivity indicates the MFI membrane was selective for CO_2 over CH_4 and is comparable to the MFI (silicalite-1) CO_2/CH_4 selectivity reported by van den Broeke et al., which was 2.4 at 30 °C and 100 kPA feed pressure for a equilmolar CO_2/CH_4 feed.[5] Also, the Kr/Xe selectivity indicates that the MFI membrane was slightly selective for Xe over Kr and the permeance trend of the noble gases (Xe > Kr > Ar > He) means the MFI membrane is reverse-selective with regards to atomic size. Reverse-selectivity is caused by surface diffusion of the noble gases through the membrane pores. Therefore, as noble gas size increases the noble gas adsorption affinity also increases because larger atoms have more electrons and larger electron clouds. Greater electron cloud size increases atomic polarizability, which increases the strength of Van der Waals' forces and therefore adsorption in the MFI membrane.[6] Bakker et al. also showed that MFI membranes (silicalite-1) are reverse selective for noble gases at room temperature due to surface diffusion and determined at high temperature (400 °C) MFI membranes are size selective for noble gases because adsorption decreases and molecular diffusivity dominates transport through the membrane.[7]

4.5 Carbon Membrane Permeation

The carbon membranes were received from Oak Ridge National Lab (ORNL) and were not characterized as part of this research. Characterization at ORNL by N_2 physisorption and SEM determined that the amorphous carbon membranes had a pore size < 0.5 nm and a membrane thickness of 200-500 nm.[8] Two carbon membranes were permeation tested (labeled sample # 2 and sample # 8).

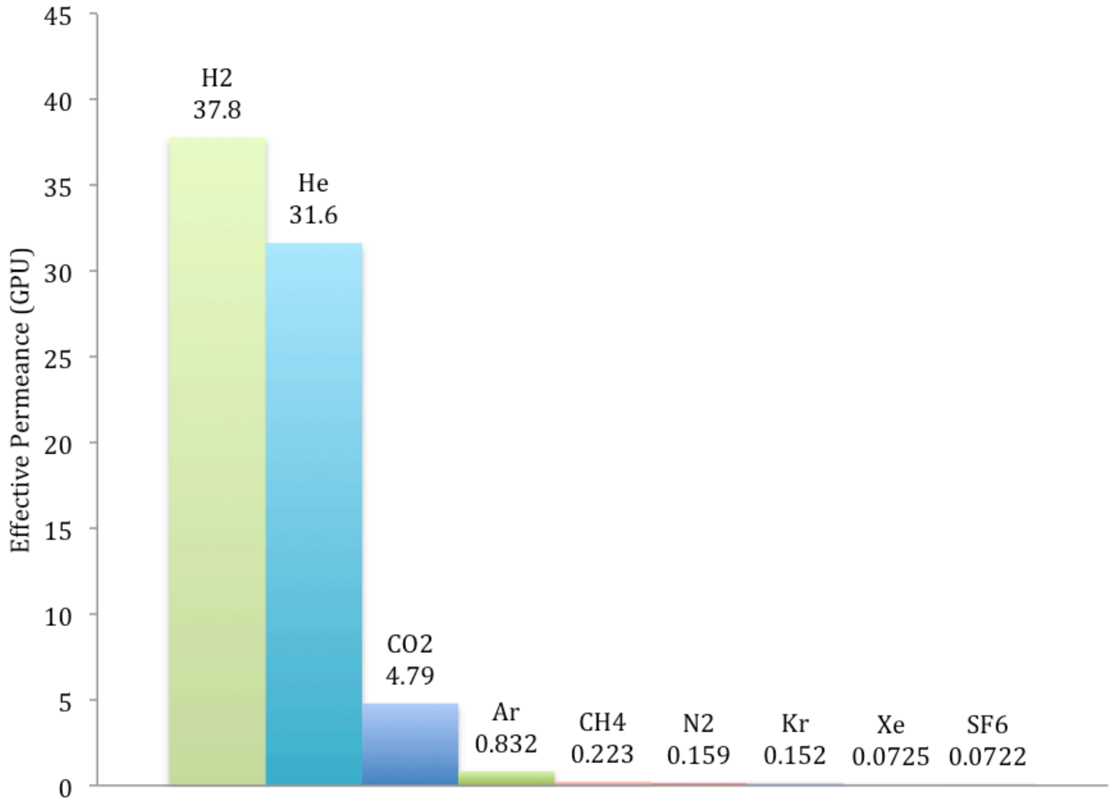

Figure 4.11: Carbon membrane (sample # 2) effective permeance at 30.4 ± 0.2 psia average feed pressure and 30.2 ± 0.3 psi average pressure drop and 25 to 26 °C (95% confidence intervals, atmospheric leak rate 1.25 x 10^{-2} GPU).

Figure 4.11 shows the carbon membrane (sample # 2) had an H_2/N_2 ideal selectivity of 238, a CO_2/CH_4 ideal selectivity of 21.5, and a Kr/Xe ideal selectivity of 2.10 for a 2 atm feed pressure at 25-26 °C. Also, Figure 4.12 shows the carbon membrane (sample # 8) had an H_2/N_2 ideal selectivity of 103, a CO_2/CH_4 ideal selectivity of 60.0, and a Kr/Xe ideal selectivity of 11.2 for a 1 atm feed pressure at 25-26°C. Both carbon membranes were essentially impermeable to Kr and Xe but can separate H_2 and He from larger gases (kinetic diameters ≥ 3.3) with high selectivity and permeance. Therefore, small pore (> 2.89 and < 3.3) amorphous carbon membranes cannot separate Kr and Xe with high Kr permeance because Kr is too large to travel through the membrane pores.

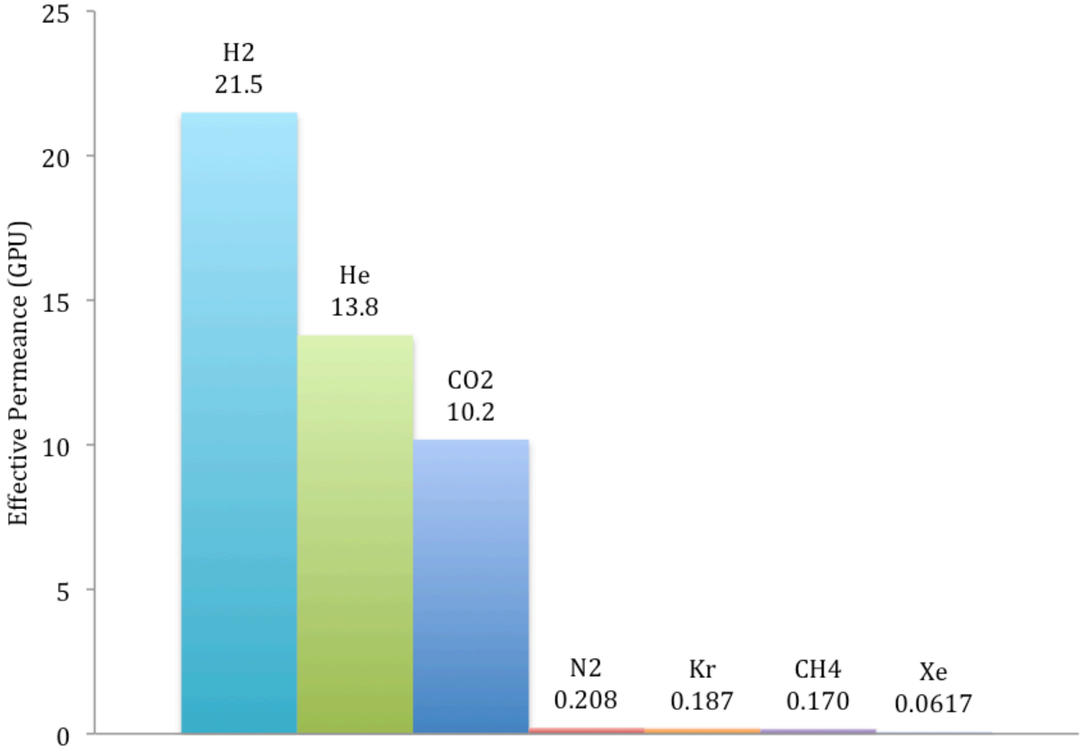

Figure 4.12: Carbon membrane (sample # 8) effective permeance at 15.4 ± 0.3 psia average feed pressure and 15.0 ± 0.4 psi average pressure drop (95% Confidence) and 25 to 26 °C (95% confidence intervals, atmospheric leak rate 2.21 x 10^{-2} GPU).

4.6 DDR Membrane Permeation

Zhou et al. synthesized and characterized (by SEM and XRD) the DDR membranes tested in this research. The DDR membranes synthesized by Zhou et al. were retested with CO_2 and the membrane with the highest CO_2 permeance was selected for further permeation testing.[9]

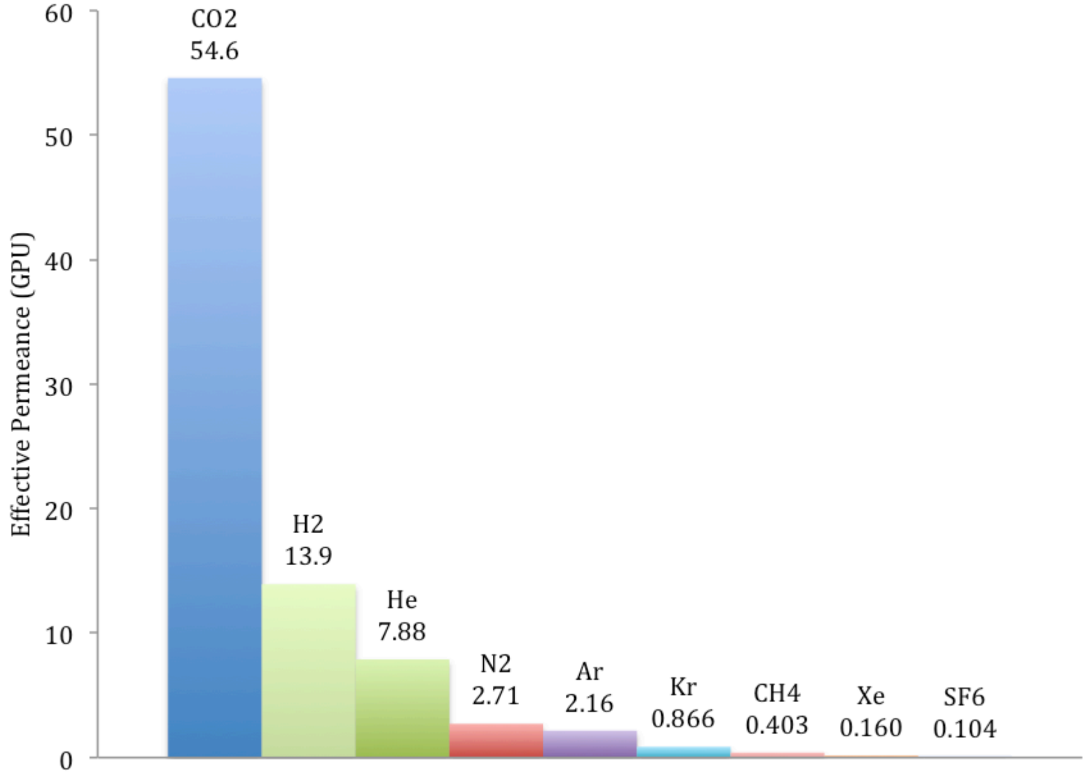

Figure 4.13: DDR membrane (treated with PDMS) effective permeance at 30.7 ± 0.5 psia average feed pressure and 30.6 ± 0.5 psi average pressure drop and 25 °C (95% confidence intervals).

From Figure 4.13, the DDR membrane permeance is two or more orders of magnitude lower than the alumina support permeance (Figures 4.5 and 4.6) and calculating the DDR permeance with Equations 2.20 compared to Equation 2.15 generates an error of 2.3% for CO_2 and 0.12% for Kr. Therefore, Equation 2.20 is valid for the DDR membrane tested in Figure 4.13 (assuming the permeance of the α-alumina support tubes is comparable to the permeance of the α-alumina support disks). The DDR membrane had a CO_2/CH_4 ideal selectivity of 135 and a Kr/Xe ideal selectivity of 5.41. This high CO_2/CH_4 selectivity for DDR is comparable to results reported by van den Bergh et al. (CO_2/CH_4 selectivities 100-3000), but DDR showed low Kr/Xe selectivity and extremely low Kr permeance. This low Kr permeance also agrees with the results of van den Bergh et al., who reported a single-component Kr flux of 0.056 mmol/m^2/s at a partial pressure drop of 200 kPa (Kr permeance of 0.836 GPU) at 30 °C through a DDR membrane (using He sweep gas at 101 kPa on permeate side).[10] DDR's low Kr permeance may be due to the rigidity of the pure-silica framework, which would not allow sufficient framework flexibility for Kr (kinetic diameter 3.6 Å) to travel through the 3.6 Å channels in DDR.[11]

4.7 SAPO-34 Seed Crystal Characterization

SAPO-34 crystals were synthesized to seed the membrane supports and facilitate defect-free membrane growth. The seeds were synthesized with a synthesis gel molar ratio of 1.0 Al_2O_3:1.0 P_2O_5:0.32 SiO_2:1.0 TEAOH:0.8 DPA:52 H_2O and at hydrothermal synthesis times of 6, 12, and 24 h while slowly rotating the acid-digestion vessel. SEM images of the seeds before calcination showed that a 6 h hydrothermal synthesis time yielded cubical crystals with a length of approximately 0.5 μm (Figure 4.14). Hydrothermal synthesis times of 12 and 24 h yielded cubical seeds with lengths ≥ 1 um (Figures 4.15 and 4.16). Only seeds synthesized for 6 h were used to seed SAPO-34 membranes because Carreon et. al. showed that seeding with smaller SAPO-34 crystals produced better quality membranes with higher CO_2/CH_4 selectivity.[12] The seeds were calcined at 390 °C for 10 hr (1 °C/min heating and cooling rate), and XRD patterns for all the calcined SAPO-34 seeds are shown in Figures 4.17, 4.18, and 4.19. The seeds all exhibited characteristic SAPO-34 peaks at 9.8°, 13°, 16°, 21°, 26°, and 31-32° (broad peak).[13]

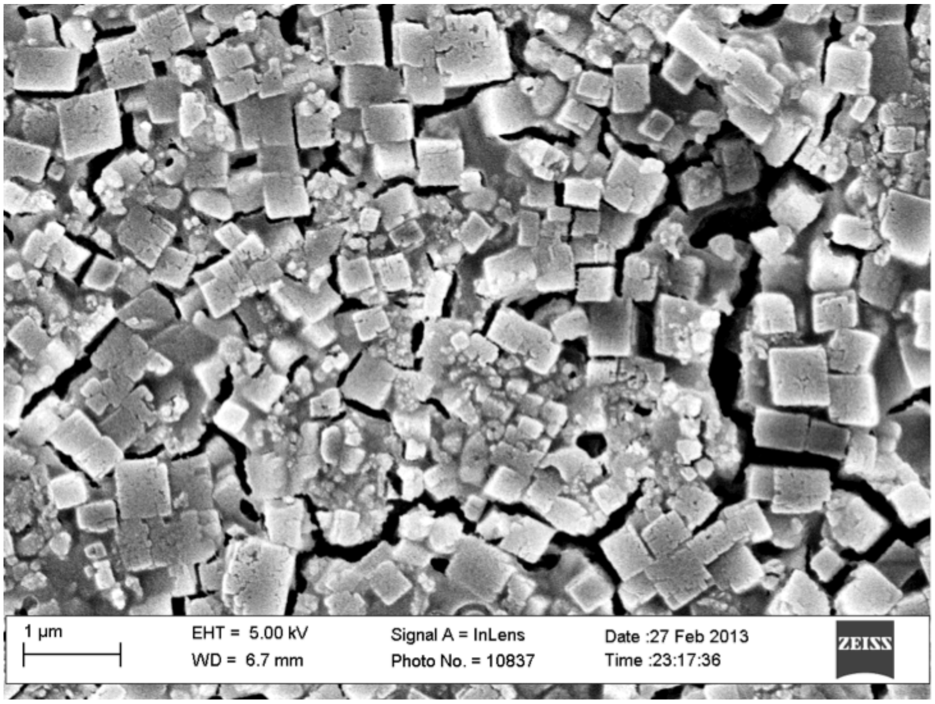

Figure 4.14: SAPO-34 seed crystals after 6 h hydrothermal synthesis before calcination.

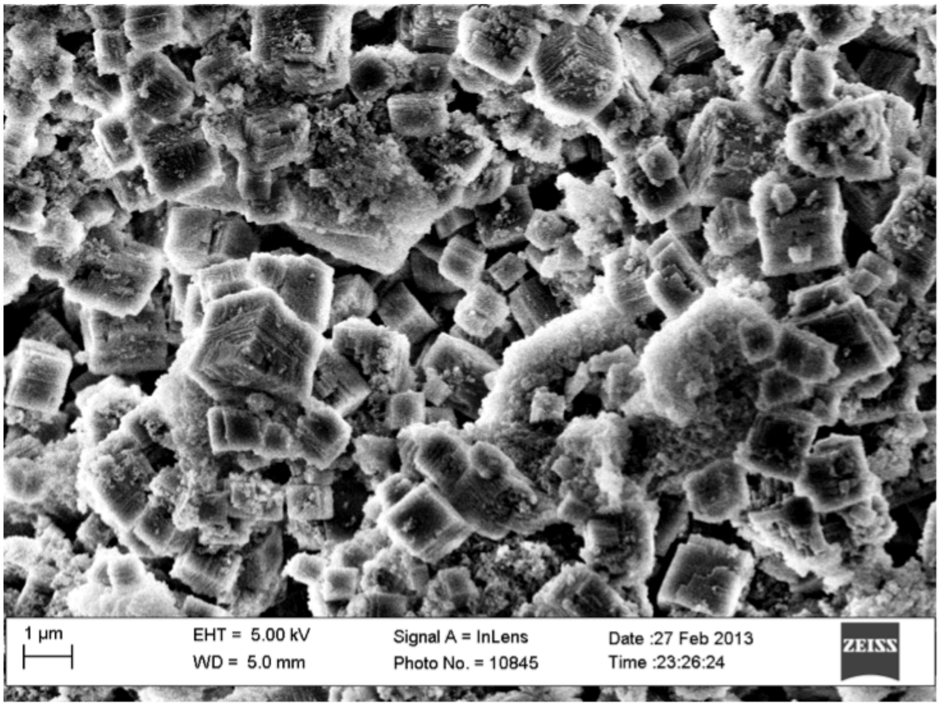

Figure 4.15: SAPO-34 seed crystals after 12 h hydrothermal synthesis before calcination.

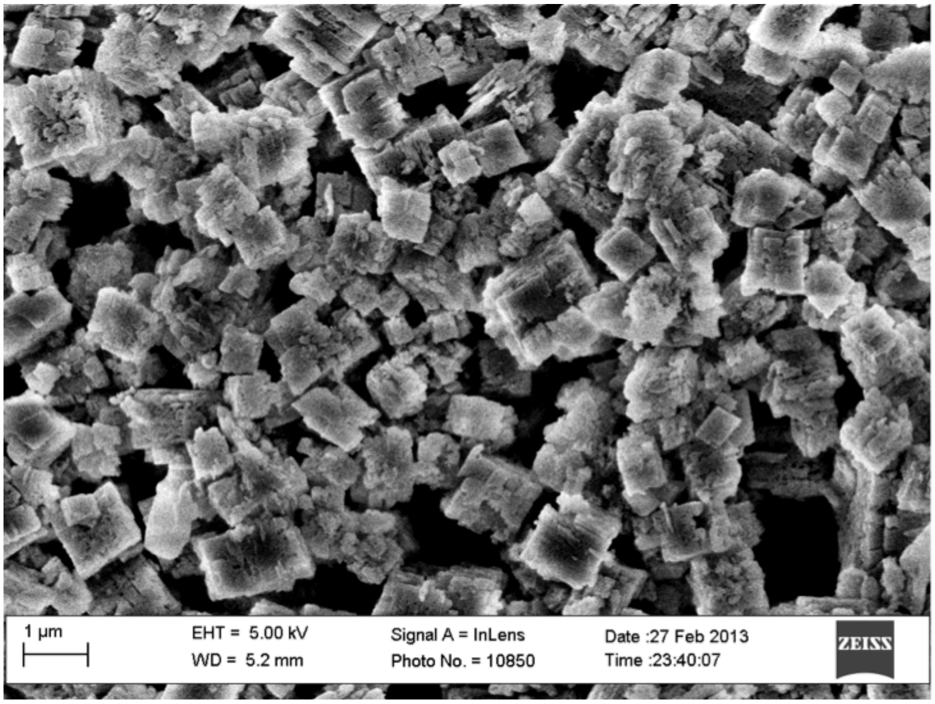

Figure 4.16: SAPO-34 seed crystals after 24 h hydrothermal synthesis before calcination.

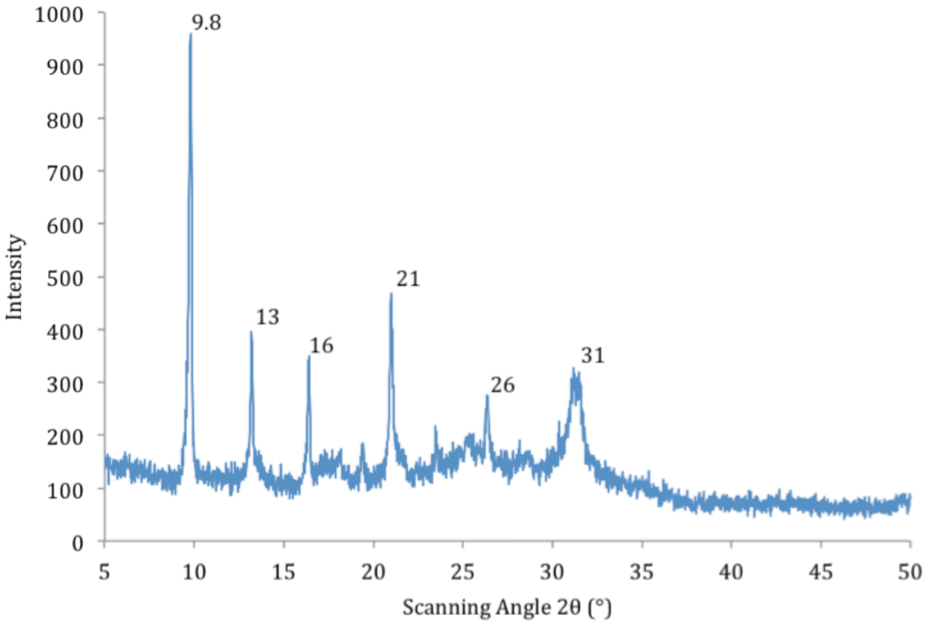

Figure 4.17: XRD pattern of SAPO-34 seed crystals after 6 h hydrothermal synthesis and calcination at 390 °C for 10 h (1 °C/min heating and cooling rate).

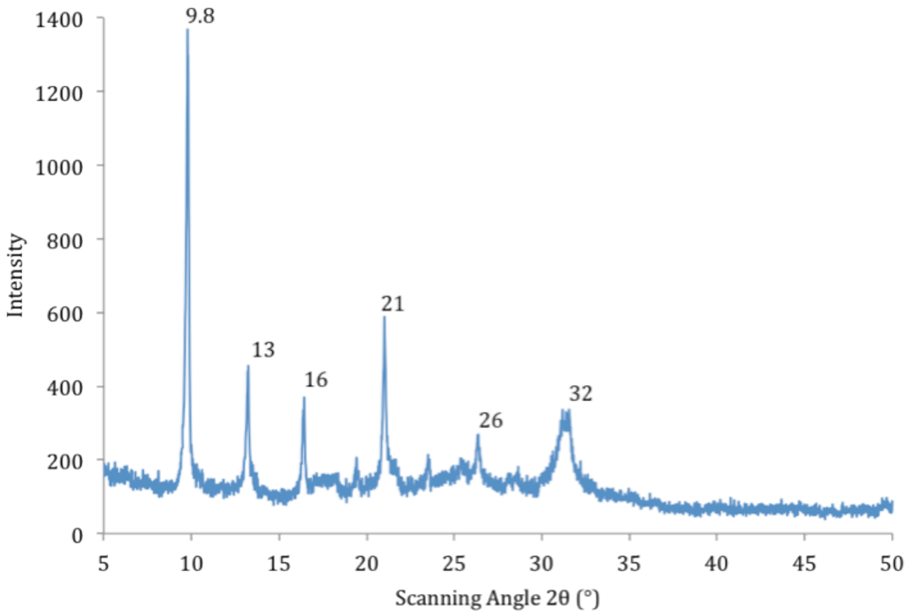

Figure 4.18: XRD pattern of SAPO-34 seed crystals after 12 h hydrothermal synthesis and calcination at 390 °C for 10 h (1 °C/min heating and cooling rate).

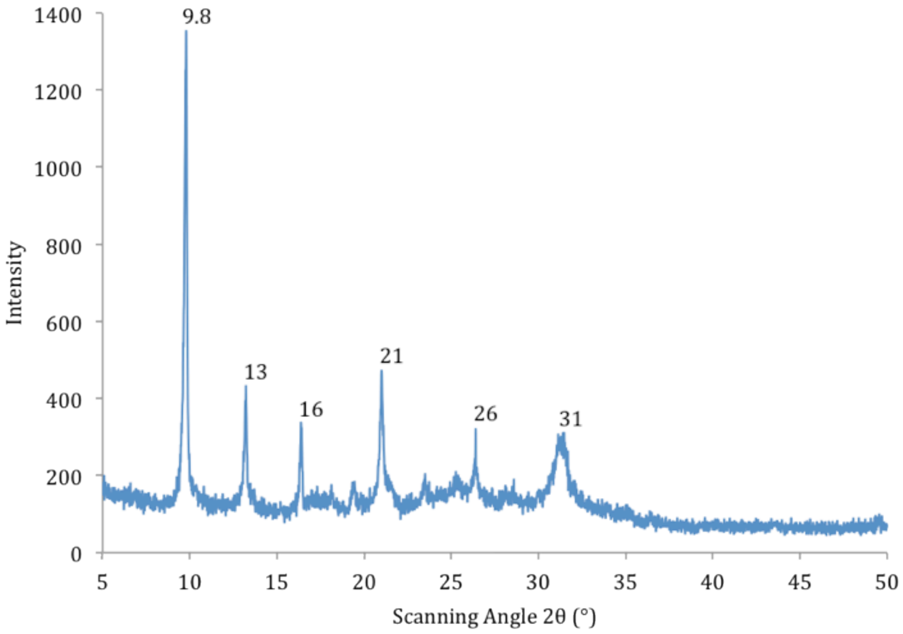

Figure 4.19: XRD pattern of SAPO-34 seed crystals after 24 h hydrothermal synthesis and calcination at 390 °C for 10 h (1 °C/min heating and cooling rate).

After the SAPO-34 seeds were calcined, black particles appeared in the seed powder (Figure 4.20). The black particles are carbon coke formed from the structure directing agents (organic molecules) breaking down at high temperature. Ideally, the structure directing agents should vaporize and evolve as a gas during calcination, leaving pure SAPO-34 crystals. However, if the structure directing agents are trapped in the SAPO-34 crystal framework or powder and cannot evolve as a gas, then they thermal degrade into carbon coke. Large coke particles were gravity separated from the crystals but fine coke particles settled at the same rate as the SAPO-34 crystals. Figure 4.21 shows the fine coke particles precipitated in the pellet with SAPO-34 seeds after centrifugation. To prevent carbon coke from contaminating the SAPO-34 membrane synthesis solution, the SAPO-34 crystals used to seed membranes were not calcined.

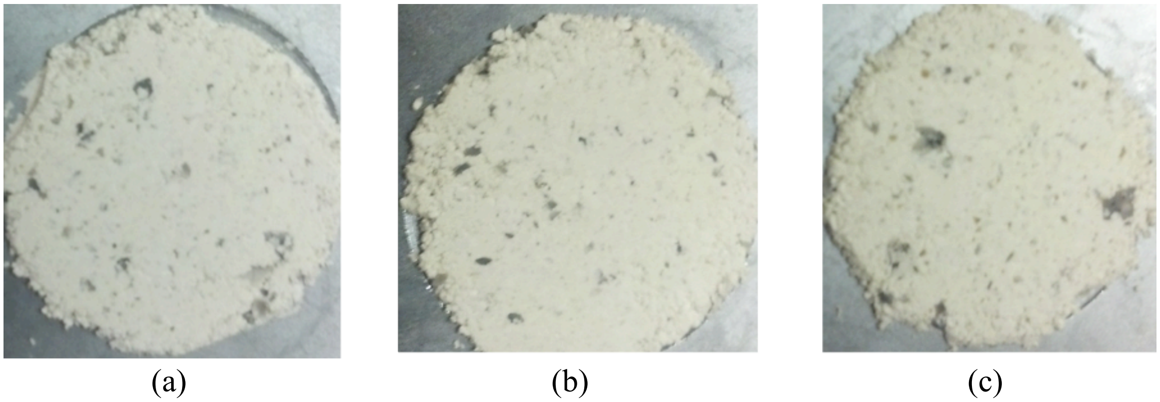
(a) (b) (c)

Figure 4.20: SAPO-34 seeds after calcination at 390 °C for 10 h (1 °C/min heating and cooling rate) for hydrothermal synthesis times of (a) 6 h, (b) 12 h, and (c) 24 h. SAPO-34 seeds are white and carbon coke is black.

(a) (b)

Figure 4.21: SAPO-34 seeds (white) after centrifugation showing carbon coke precipitated as light grey color in center of pellet. Hydrothermal synthesis time of (a) 6 h and (b) 24 h.

4.8 SAPO-34 Membrane Seeding Technique

Two techniques were explored to seed the α-alumina discs: cotton swab rubbing and finger rubbing (procedures described in Chapter 3.7). Figure 4.22 shows the disc surface after seeding with a cotton swab, and Figure 4.23 shows the disc surface after seeding by finger rubbing. Overall, seeding with the finger rubbing technique covered more of the disc surface with SAPO-34 seeds; therefore, membrane support discs were only seeded by finger rubbing.

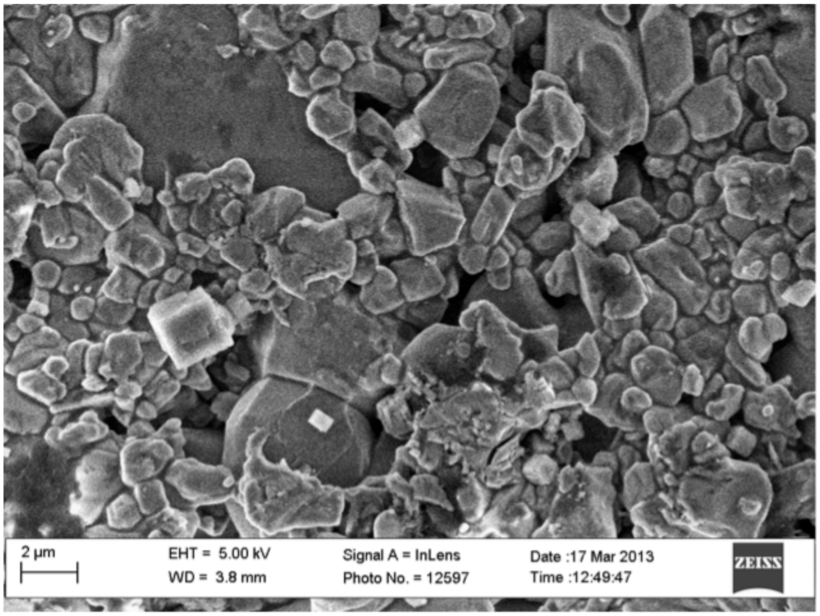

Figure 4.22: α-alumina disc seeded with cotton swab gives low seed layer surface coverage.

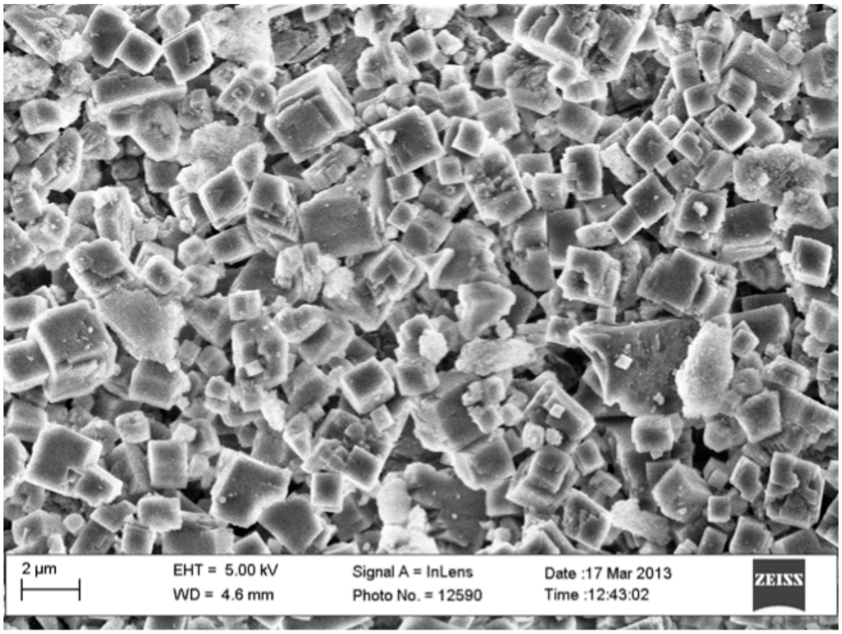

Figure 4.23: α-alumina disc seeded by finger rubbing gives high seed layer surface coverage.

4.9 SAPO-34 Membrane Synthesis Troubleshooting

SAPO-34 membranes were initially synthesized with a synthesis gel molar ratio of 1.0 Al_2O_3:1.0 P_2O_5:0.32 SiO_2:1.0 TEAOH:1.6 DPA:77 H_2O, a hydrothermal synthesis time of 24 h, and calcined at 390 °C for 10 h (1 °C/min heating and cooling rate). The resulting membranes were visually continuous and defect-free (Figure 4.24), and the XRD pattern (Figure 4.25) gave characteristic SAPO-34 peaks at 9.6°, 13°, 16°, and 31° (SAPO-34 peak at 26° overlaps with α-alumina peak at 26°).

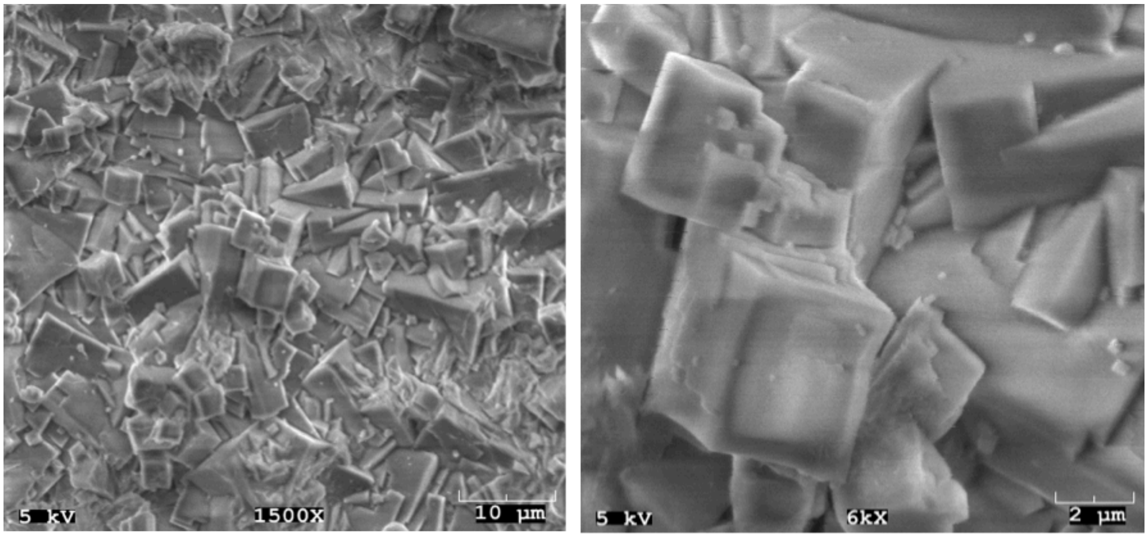

Figure 4.24: SAPO-34 membrane with synthesis gel molar ratio of 1.0 Al_2O_3:1.0 P_2O_5:0.32 SiO_2:1.0 TEAOH:1.6 DPA:77 H_2O, 24 h hydrothermal synthesis time, and calcined at 390 °C for 10 h (1 °C/min heating and cooling rate).

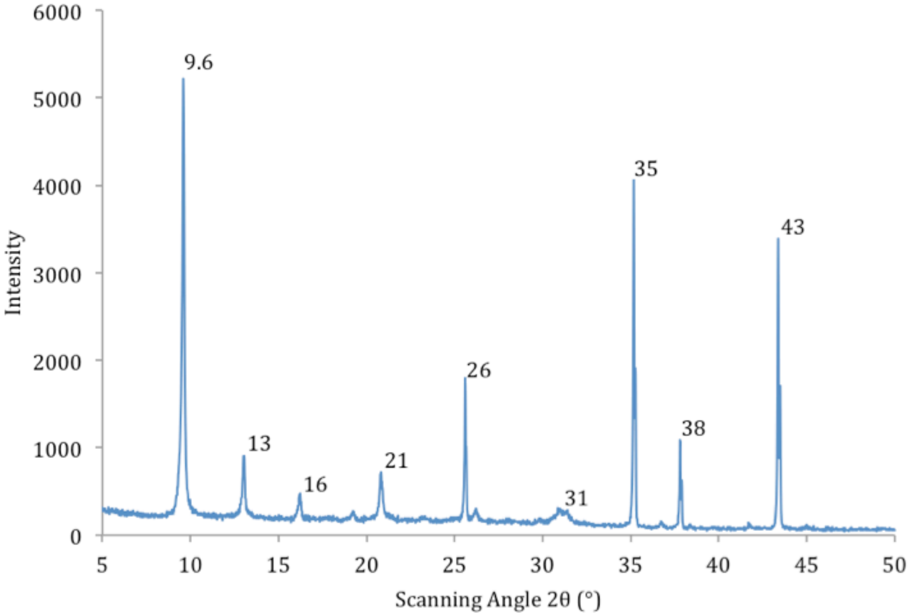

Figure 4.25: XRD pattern of SAPO-34 membrane with synthesis gel molar ratio of 1.0 Al_2O_3:1.0 P_2O_5:0.32 SiO_2:1.0 TEAOH:1.6 DPA:77 H_2O, 24 h hydrothermal synthesis time, and calcined at 390 °C for 10 h (1 °C/min heating and cooling rate). Peaks at 26°, 35°, 38°, and 43° are from α-alumina support disc.

However, after calcination the membranes turned from white to yellow and formed large cracks across the surface (Figure 4.26). Therefore, the selectivity of SAPO-34 membranes was essentially equal to the α-alumina disc selectivity because large cracks formed in the membrane layer during calcination. The membranes were calcined by heating them in stagnant air to vaporize and remove the structure directing agents from the membrane pores. During hydrothermal synthesis, the structuring direct agents act as a template to form the specific crystal structure of the desired zeolite but the membranes as essentially impermeable until the structuring directing agents are removed from the zeolite pores. Calcination at high temperature is a common way to remove the structure directing agents, but the thermal expansion and contraction of the zeolite membrane and α-alumina support disc during heating and cooling can form thermal stress cracks in the zeolite membrane.[14] To address the calcination problems, the synthesis solution was diluted to give a synthesis gel molar ratio of 1.0 Al_2O_3:1.0 P_2O_5:0.32 SiO_2:1.0 TEAOH:1.6 DPA:150 H_2O and the hydrothermal synthesis time was decreased to 6 h, replicating the SAPO-34 membrane synthesis procedure developed by Li et al.[15] Figure 4.27 shows the improved SAPO-34 membranes did not form large cracks after calcination but still turned from white to yellow. Subsequent permeation testing revealed that the improved membranes were essentially impermeable to all the test gases, indicating that the membrane template was not completely removed during calcination.

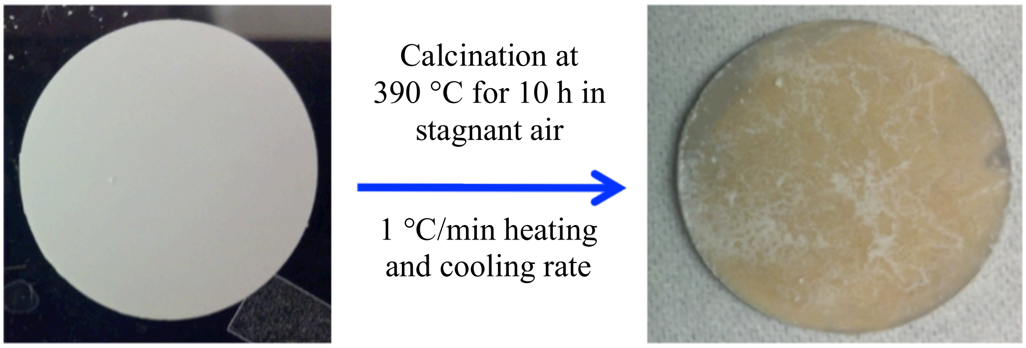

Figure 4.26: Calcination effect on SAPO-34 membrane (synthesis gel molar ratio of 1.0 Al_2O_3:1.0 P_2O_5:0.32 SiO_2:1.0 TEAOH:1.6 DPA:77 H_2O and 24 h hydrothermal synthesis time).

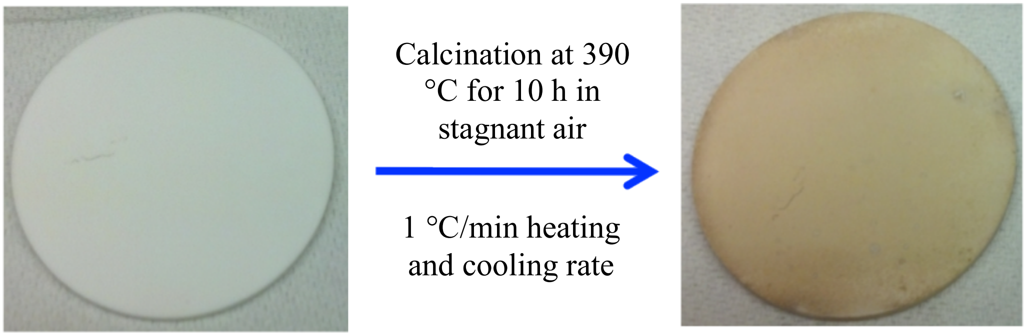

Figure 4.27: Calcination effect on SAPO-34 membrane (synthesis gel molar ratio of 1.0 Al_2O_3:1.0 P_2O_5:0.32 SiO_2:1.0 TEAOH:1.6 DPA:150 H_2O and 6 h hydrothermal synthesis time).

To completely remove the membrane template the membranes were treated with UV light for 24 hr before calcining them at 390 °C for 10 h, 550 °C for 6 h, or 700 °C for 6 h The calcination heating and cooling rate was decreased to 0.5 °C/min heating and cooling rate to prevent cracking from expansion and contraction of the membrane during calcination. Also, a membrane was calcined at 550 °C for 6 h without UV treatment, and all the membrane supports were seeded 3 times each by the finger seeding technique (procedure described in Chapter 3.7), instead of a single time as done in the previous SAPO-34 membrane synthesis, to thoroughly cover the support surfaces with seeds. The membranes after calcination are shown in Figure 4.28. The membranes calcined at of above 550 °C were white after calcination, indicating that the organic template was completely removed.

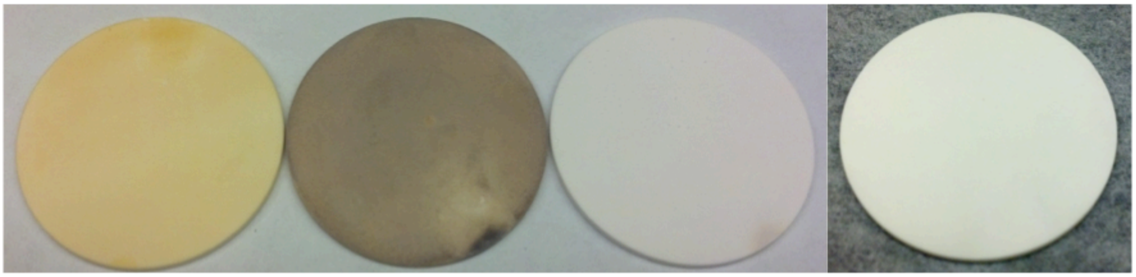
(a) (b) (c) (d)

Figure 4.28: SAPO-34 membranes (a) UV treated, (b) UV treated and then calcined at 390 °C for 10 h, (c) UV treated and then calcined at 550 °C for 6 h, (d) calcined at 550 °C for 6 h.

4.10 UV Treated SAPO-34 Membrane Permeation Testing

The SAPO-34 membrane that was UV treated and calcined at 550 °C for 6 h was permeation tested and results are shown in Figure 4.29. Before each test, the membrane was degassed under vacuum at 100 °C for 30 min and cooled under vacuum for 1.5 h to room temperature.

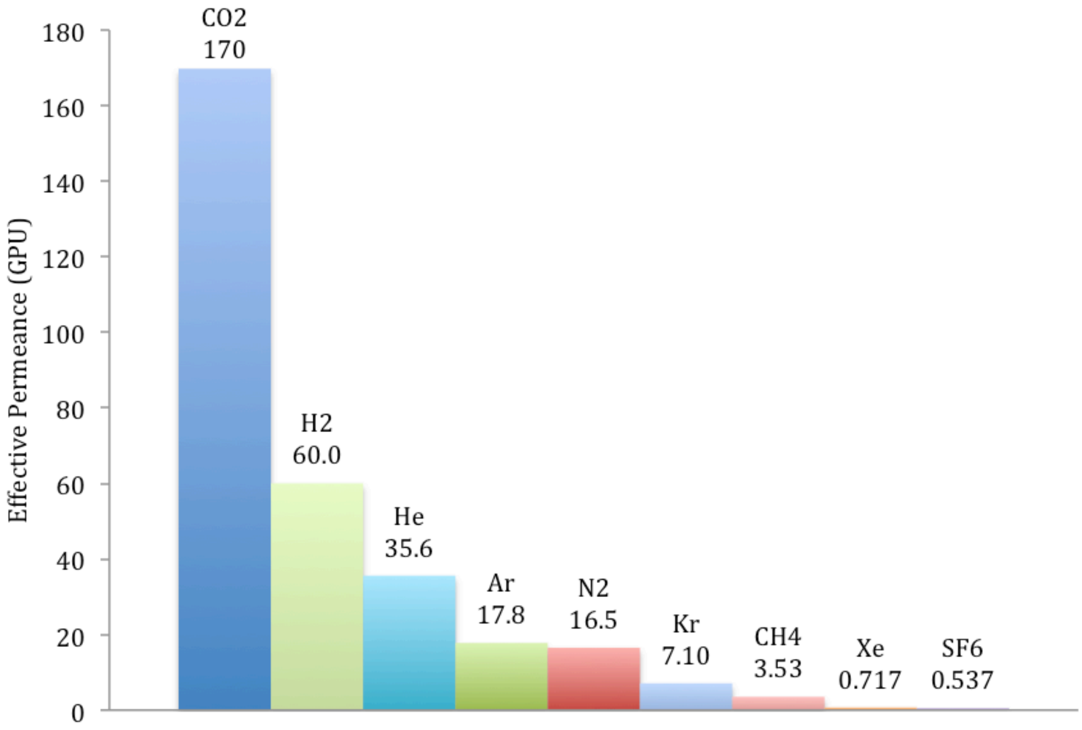

Figure 4.29: SAPO-34 membrane (UV treated) effective permeance at 30.2 ± 0.4 psia average feed pressure and 30.0 ± 0.4 psi average pressure drop and 25-28 °C (95% confidence intervals). Degassed at 100 °C for 30 min under vacuum between each test.

From Figure 4.29, the SAPO-34 membrane had a CO_2/CH_4 ideal selectivity of 48.2 and Kr/Xe ideal selectivity of 9.90 at 2 atm feed pressure and 25-28 °C. The SAPO-34 membrane also had a Kr permeance of 7.10 GPU, which is close to the goal of 10 GPU. Since the SAPO-34 membrane strongly adsorbs water which could block the membrane pores, the membrane was initially degassed at 200 °C for 30 min under vacuum and then retested with Kr and Xe. The results are given in Figure 4.30, and the membrane was degassed for 10 min under vacuum at the test temperature in between each test.

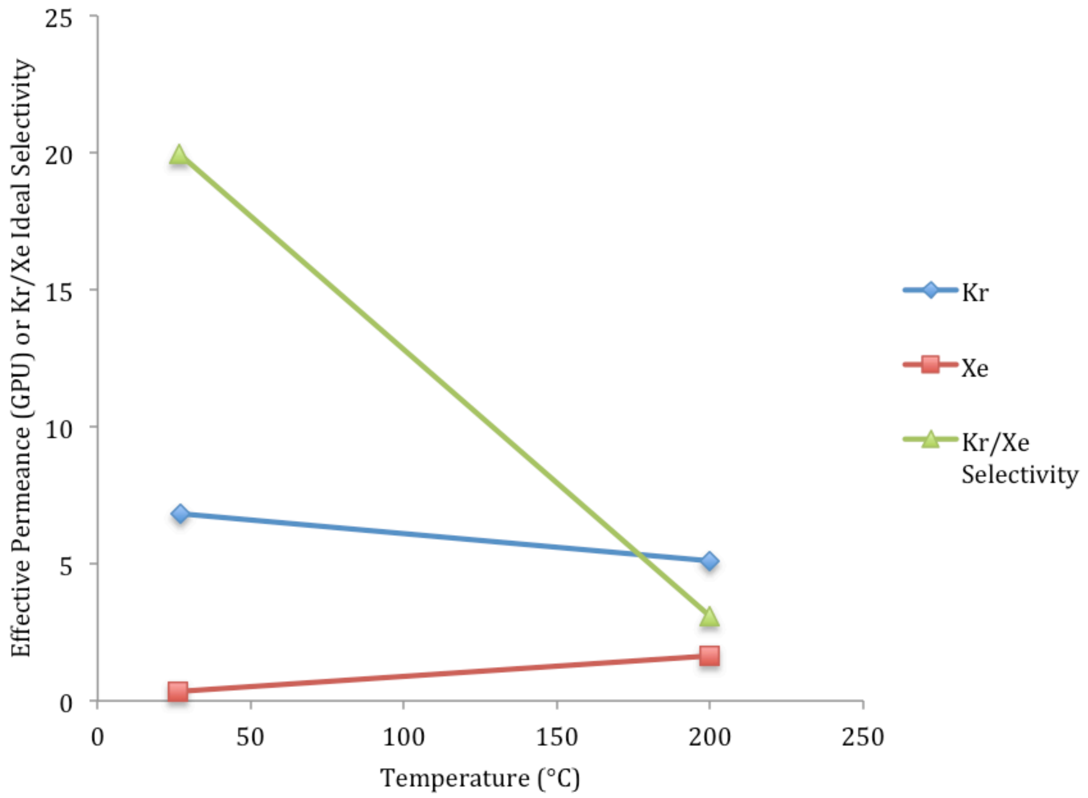

Figure 4.30: SAPO-34 membrane (UV treated) Kr and Xe Effective Permeance and Kr/Xe Ideal selectivity at 30.8 ± 0.2 psia average feed pressure and 30.7 ± 0.2 psi average pressure drop (95% confidence intervals). Initially degassed at 200 °C for 30 min under vacuum.

Figure 4.30 shows that SAPO-34 Kr/Xe ideal selectivity increases as temperature decreases because Kr permeance increases and Xe permeance decreases with decreasing temperature. This indicates that Kr transport through the membrane is adsorption controlled and Xe transport through the membrane is diffusion controlled.

4.11 SAPO-34 UV Treatment and Seeding Permeation Effects

To determine the effect of UV treatment and seeding on SAPO-34 membrane quality, six SAPO-34 membranes were synthesized (synthesis gel molar ratio 1.0 Al_2O_3:1.0 P_2O_5:0.32 SiO_2:1.0 TEAOH:1.6 DPA:150 H_2O) and permeation tested with

CO2 and CH4. Two membranes were finger seeded by a single seed layer, two membranes were finder seeded by 3 seed layers, and 2 membranes were not seeded on the support surface but in the synthesis solution (seeded gel) right before hydrothermal synthesis. After hydrothermal synthesis for 6 h, half of the membranes were UV treated and then all of the membranes were calcined at 550 °C for 6 h (1 °C/min heating and cooling rate). The membranes were permeation tested with CO2 and CH4 at 25 °C and 200 °C.

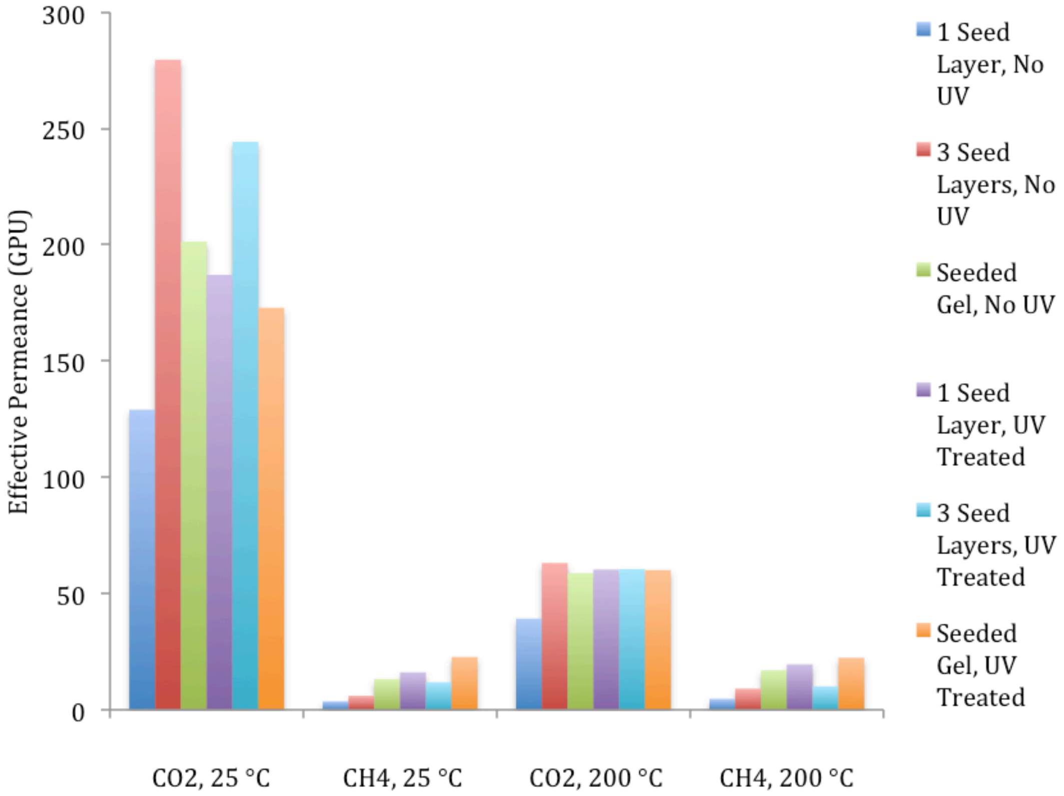

Figure 4.31: SAPO-34 CO_2 and CH_4 effective permeances at 25 °C and 200 °C, 15.1 ± 0.1 psia average pressure, and 14.4 ± 0.4 psi average pressure drop (95% confidence intervals). Degassed at 200 °C for 15 min under vacuum between each test.

Figure 4.31 shows that out of all the membrane, the membrane seeded with 3 seed layers and not UV treated had the highest CO2 permeance and the membrane seeded with 1 seed layer and not UV treated had the lowest CH_4 permeance. From Figure 4.32, the membrane seeded with 3 seed layers and not UV treated had the highest CO_2/CH_4 selectivity and the membrane seeded in the synthesis gel and UV treated had the lowest CO_2/CH_4 selectivity. Overall, the results in Figures 4.31 and 4.32 show that UV treatment before calcination does not increase SAPO-34 membrane quality and performance but SAPO-34 membrane quality and performance is significantly affected by the support seeding method.

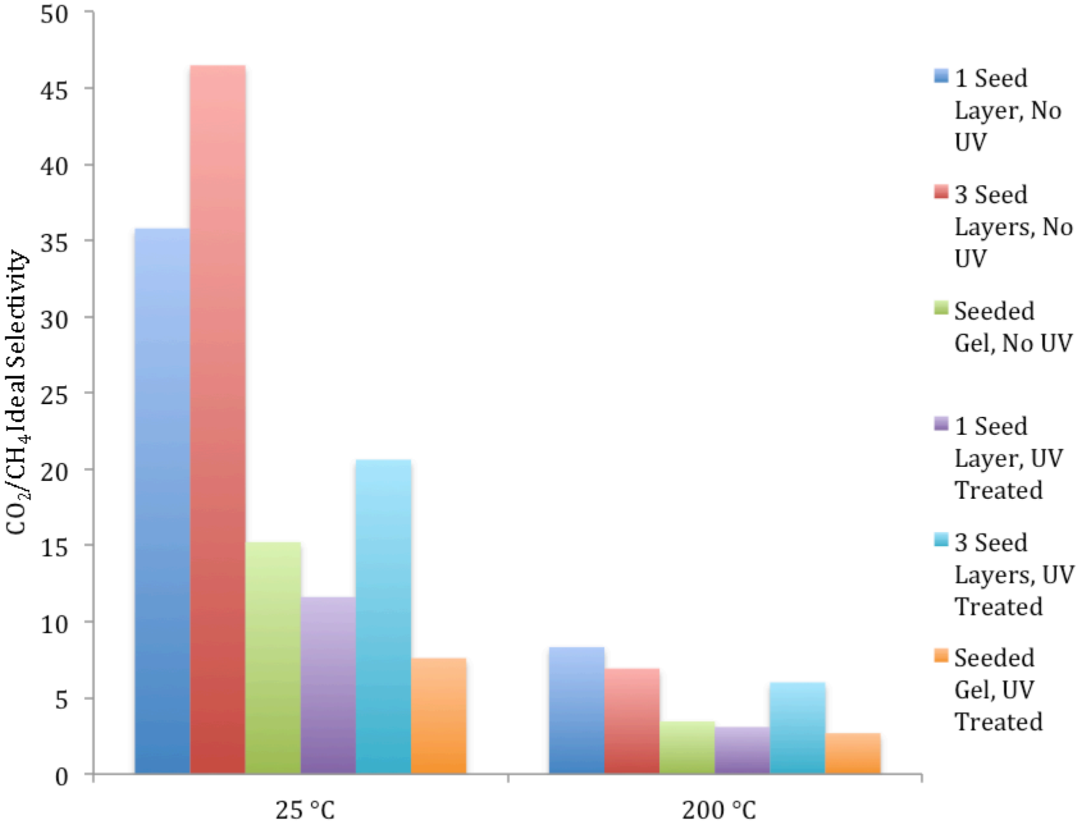

Figure 4.32: SAPO-34 CO_2/CH_4 ideal selectivities at 25 °C and 200 °C, 15.1 ± 0.1 psia average feed pressure, and 14.4 ± 0.4 psi average pressure drop (95% confidence intervals). Degassed at 200 °C for 15 min under vacuum between each test.

4.12 SAPO-34 Membrane Reproducibility

To determine SAPO-34 membrane reproducibility, 4 membranes were synthesized with a synthesis gel molar ratio of 1.0 Al_2O_3:1.0 P_2O_5:0.3 SiO_2:1.0 TEAOH:1.6 DPA:150 H_2O, a 6 h hydrothermal synthesis time, and calcined at 550 °C for 6 h (0.5 °C heating and cooling rate). The membranes were seeded by depositing 3 seed layers on each α-alumina discs using the finger rubbing technique, and the seeds had a synthesis gel molar ratio of 1.0 Al_2O_3:1.0 P_2O_5:0.3 SiO_2:1.0 TEAOH:1.6 DPA:77 H_2O. After calcination, SEM imaging showed the membrane surfaces were visually continuously and defect-free (Figure 4.33).

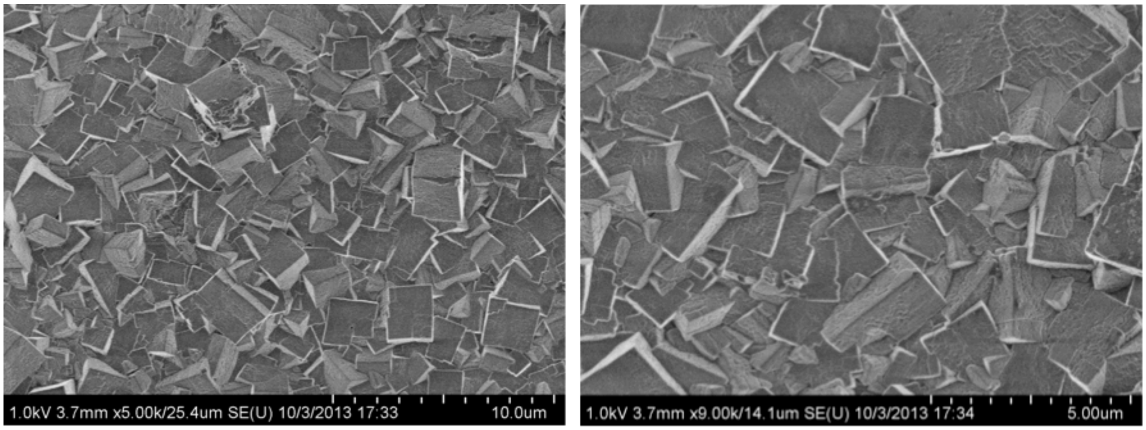

Figure 4.33: SAPO-34 membrane surface with synthesis gel molar ratio of 1.0 Al_2O_3:1.0 P_2O_5:0.3 SiO_2:1.0 TEAOH:1.6 DPA:150 H_2O, 6 h hydrothermal synthesis time, and calcined at 550 °C for 6 h.

XRD characterization (Figure 4.34) showed the membrane degree of crystallinity decreased compared to the 24 h hydrothermal synthesis membrane (Figure 4.25) because all of the characteristic SAPO-34 peaks decreased in intensity. This decrease in degree of crystallinity may be caused by a decrease in the membrane thickness after increasing the synthesis gel dilution factor and decreasing the membrane hydrothermal synthesis time to

6 h. From SEM images of the membrane cross-section (Figures 4.35 and 4.36), the membrane thickness was ~ 11 um.

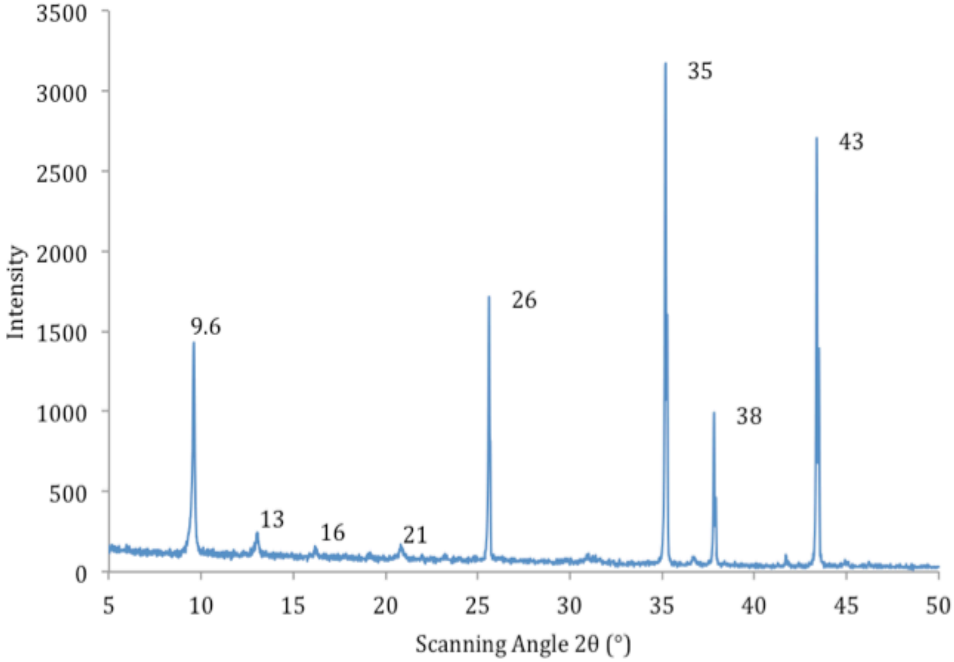

Figure 4.34: XRD pattern of SAPO-34 membrane with synthesis gel molar ratio of 1.0 Al_2O_3:1.0 P_2O_5:0.3 SiO_2:1.0 TEAOH:1.6 DPA:150 H_2O, 6 h hydrothermal synthesis time, and calcined at 550 °C for 6 h. Peaks at 26°, 35°, 38°, and 43° are from α-alumina support disc.

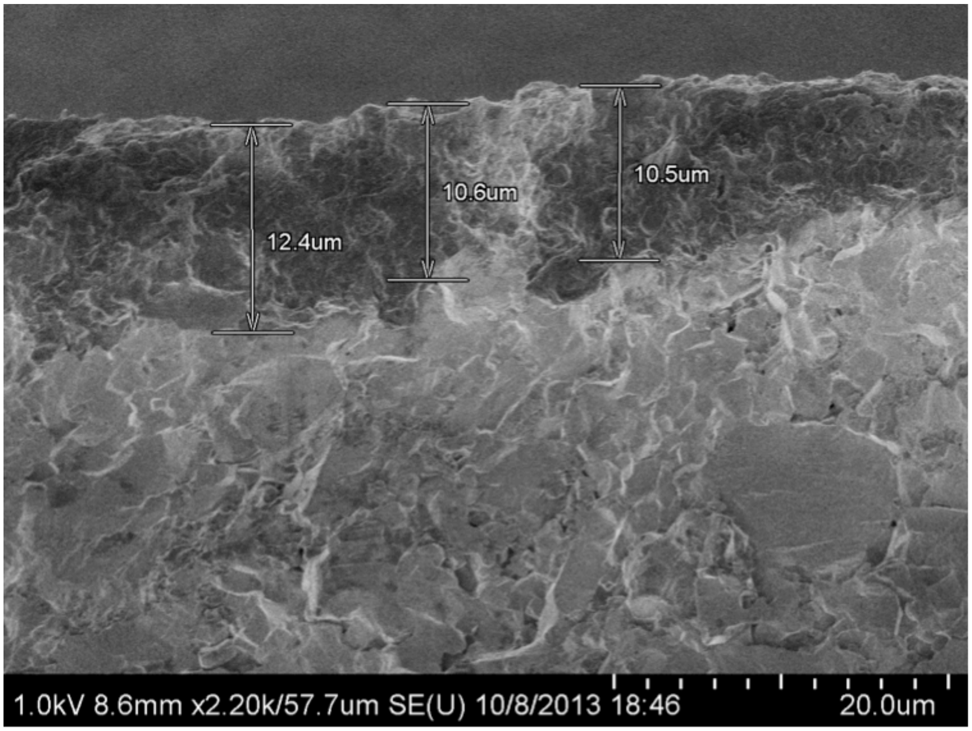

Figure 4.35: Cross-section of SAPO-34 membrane with synthesis gel molar ratio of 1.0 Al_2O_3:1.0 P_2O_5:0.3 SiO_2:1.0 TEAOH:1.6 DPA:150 H_2O, 6 h hydrothermal synthesis time, and calcined at 550 °C for 6 h. Average membrane thickness is 11.2 ± 0.99 µm (95% confidence interval).

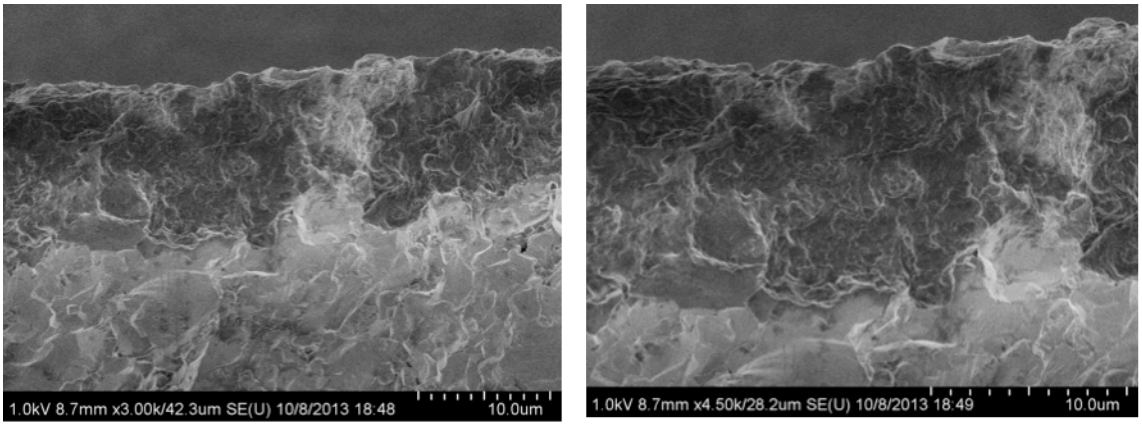

Figure 4.36: Cross-section of SAPO-34 membrane with synthesis gel molar ratio of 1.0 Al_2O_3:1.0 P_2O_5:0.3 SiO_2:1.0 TEAOH:1.6 DPA:150 H_2O, 6 h hydrothermal synthesis time, and calcined at 550 °C for 6 h.

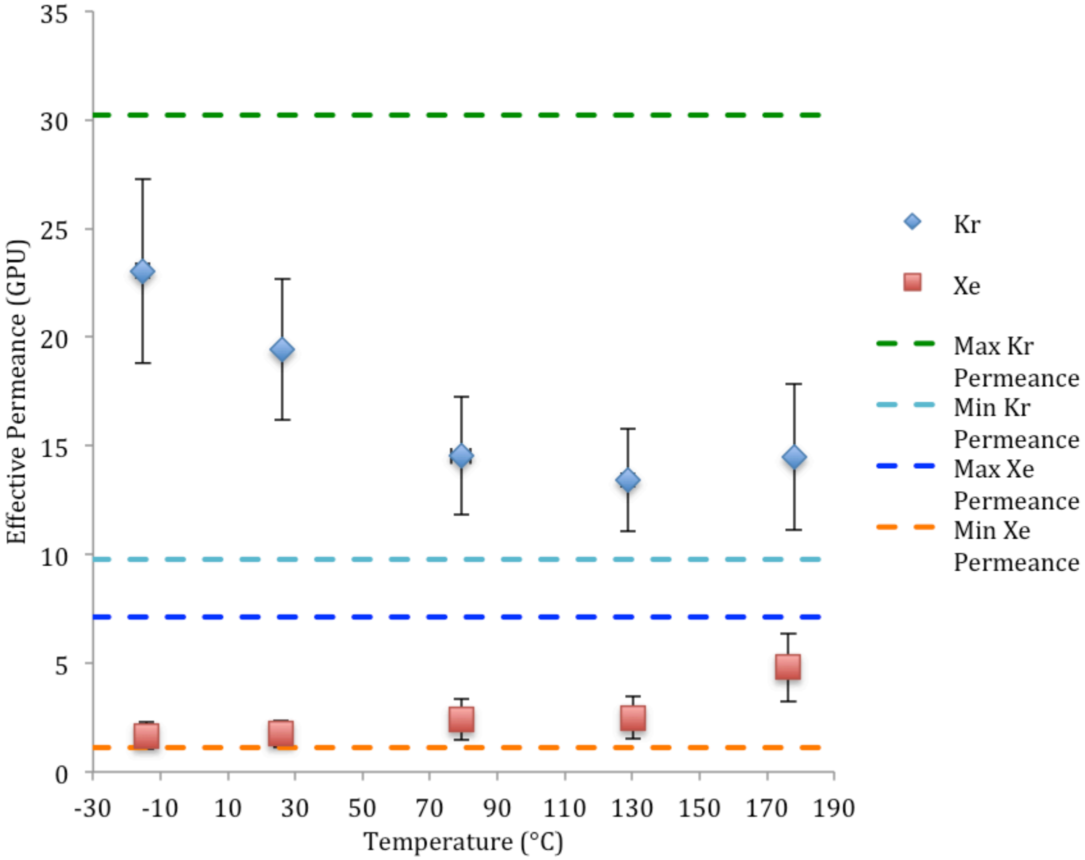

Figure 4.37: SAPO-34 Kr and Xe Permeance at 15.3 ± 0.1 psia average feed pressure and 15.2 ± 0.1 psi average pressure drop (95% confidence intervals). Average of 4 membranes, error bars are one standard deviation.

The membranes were permeation tested with Kr and Xe from -15 to 180 °C with a 1 atm feed pressure, and the results should high reproducibility between membranes. From Figure 4.37, the average Kr permeance increases and the average Xe permeance decreases and the temperature. However, there is a minimum in the Kr permeance at about 130 °C, and at ambient temperature the average Kr permeance is 19.4 GPU, which is about 2 times the goal of 10 GPU. Overall, the Kr permeance increased by 72% from the minimum 130 °C and the Xe permeance decreased by 65% over the entire temperature range.

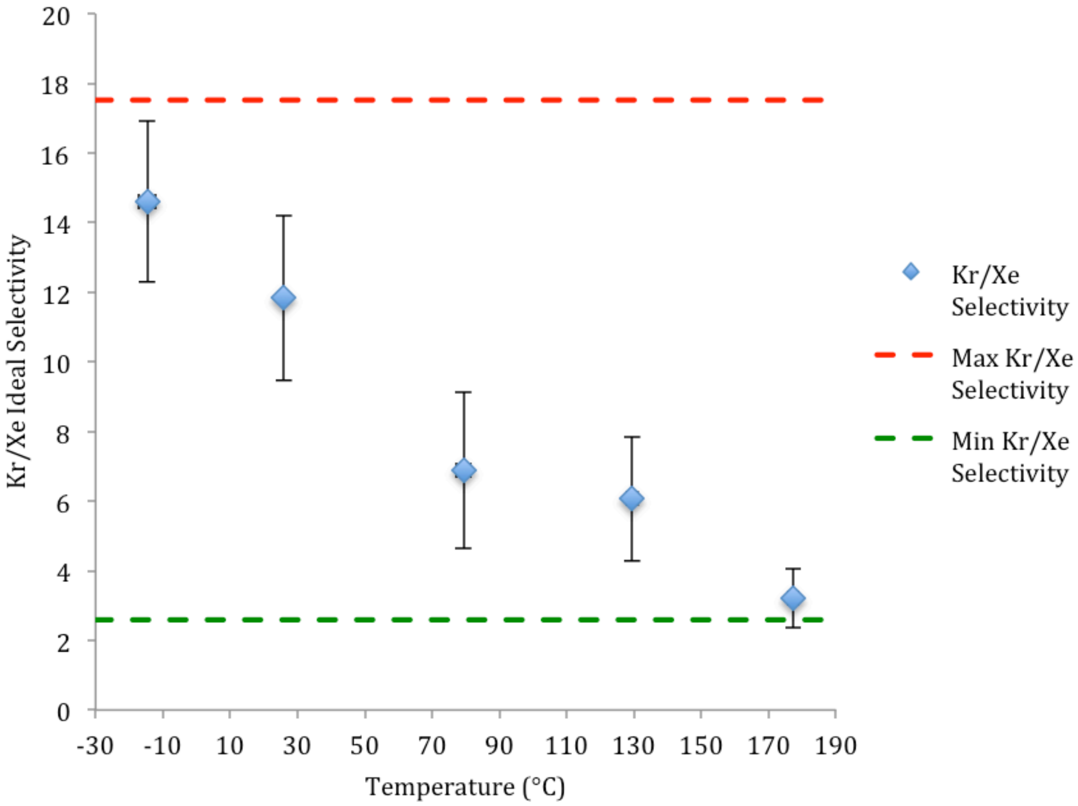

Figure 4.38: SAPO-34 Kr/Xe ideal selectivity at 15.3 ± 0.1 psia average feed pressure and 15.2 ± 0.1 psi average pressure drop (95% confidence intervals). Average of 4 membranes, error bars are one standard deviation (selectivity calculated per membrane and then averaged).

Figure 4.38 shows that the average Kr/Xe ideal selectivity increases as temperature decreases from 180 °C to -15 °C. The maximum average Kr/Xe selectivity was 14.6 at about -15 °C, and at ambient temperature the average selectivity was 11.8. Overall, the average Kr/Xe ideal selectivity increased by 355% from 180 °C to -15 °C.

4.13 SAPO-34 Membrane Defect Permeation

The defect permeance was calculated by assuming all the flux through the membranes before the lag time inflection point was through defects. Therefore, the product of the defect permeance and defect fractional surface coverage ($\theta\overline{P}_{M_i,defects}$ term in Equation 2.19) was calculated by determining the slope of the of the experimental dP/dt curve before the lag time inflection point and then using data analysis method presented in Chapter 3.9 with the defect *dP/dt* slope. Lag times only occurred during Xe testing because the Xe flux is sufficiently slow through SAPO-34 (Kr lag time is essentially zero because the Kr membrane flux is usually one orders of magnitude greater than the Xe membrane flux) Out of the 4 membranes synthesized in Chapter 4.12, only 3 exhibited lag times at ≤ 80 °C and one of those three did not exhibit a lag time at about 80 °C. The membrane with the highest Kr/Xe ideal selectivity from -15 to 180°C did not exhibit a Xe permeance any lag time over the tested temperature range. The graphical analysis for each membrane that exhibited a Xe lag time is in Appendix D. Also, assuming all transport through membrane defects is by Knudsen diffusion, the Kr defect permeance was calculated from the Xe defect permeance for each membrane by using Equation 2.3.

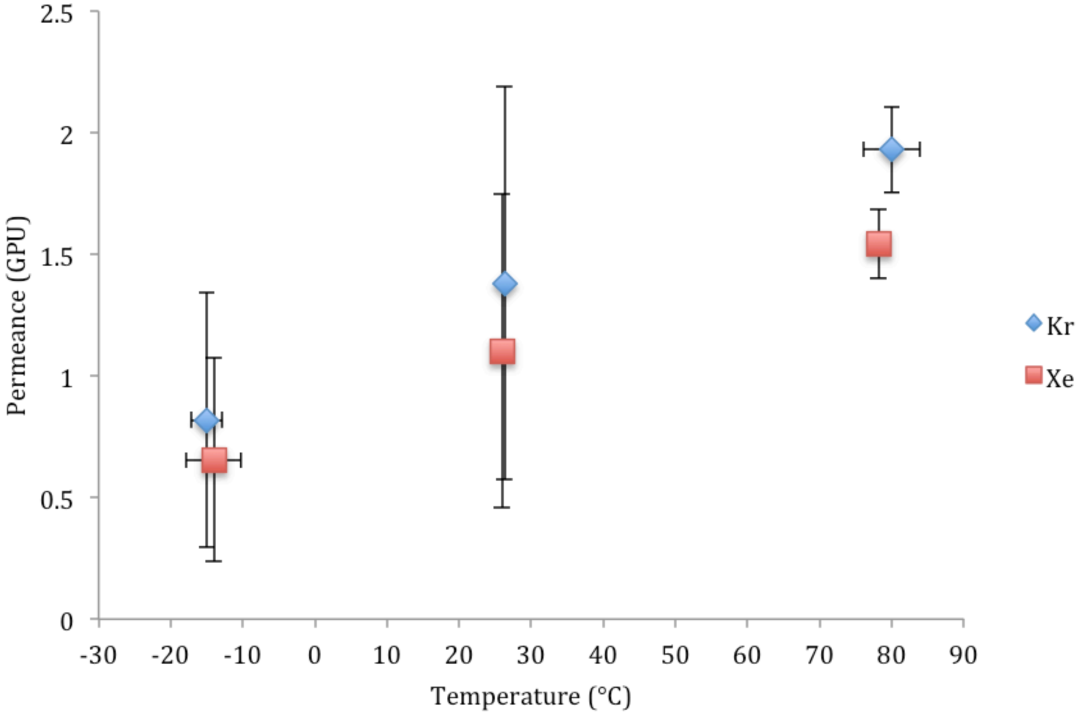

Figure 4.39: SAPO-34 Kr and Xe defect permeance at 15.2 ± 0.1 psia average feed pressure and 15.2 ± 0.1 psi average pressure drop (95% confidence interval). Points at about -15°C and 26 °C are average of 3 membranes, points at about 80 °C are average of two membranes, error bars are one standard deviation.

Figure 4.39 shows the average Kr and Xe defect permeances through all the SAPO-34 membranes that exhibited a Xe lag time. The average defect permeance for Kr and Xe increases as temperature increases, which agrees with Knudsen diffusion permeance (Equation 2.34) because Knudsen diffusivity (Equation 2.31) increases as the temperature increases. Subtracting the average defect permeance from the average total permeance using Equation 2.19 leaves the defect-free permeance of Kr and Xe through SAPO-34 (Figure 4.40). At ambient temperature, Kr defect permeance accounts for 6.93% of the total permeance, and Xe defect permeance accounts for 57.0% of the total Xe permeance.

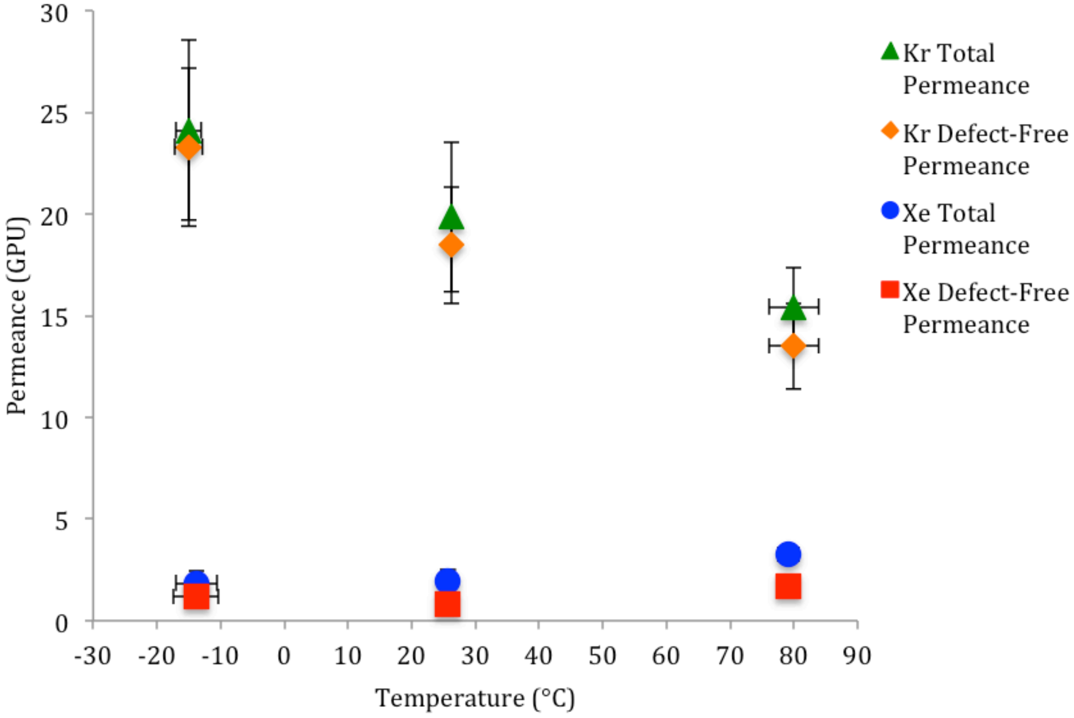

Figure 4.40: SAPO-34 total and defect-Free Kr and Xe Permeance at 15.3 ± 0.03 psia average feed pressure and 15.2 ± 0.04 psi average pressure drop (95% confidence intervals). Points at about -15°C and 26 °C are average of 3 membranes, points at about 80 °C are average of two membranes, error bars are one standard deviation.

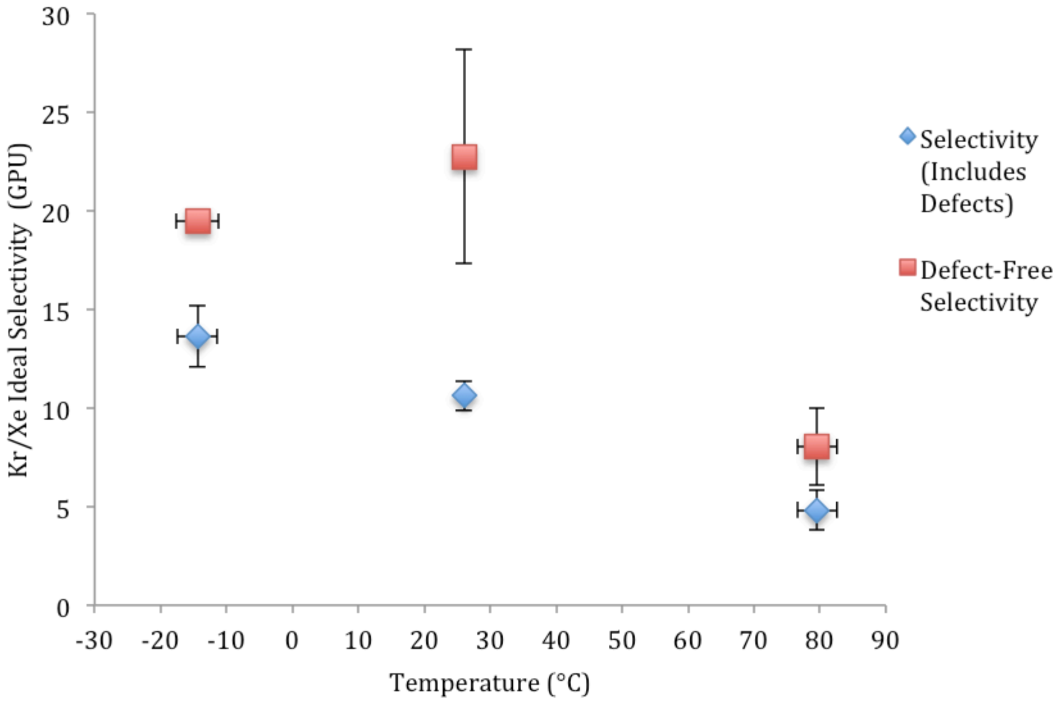

Figure 4.41: SAPO-34 defect-free Kr/Xe ideal selectivity at 15.3 ± 0.08 psia average feed pressure and 15.2 ± 0.1 psi average pressure drop (95% confidence intervals). Points at about -15°C and 26 °C are average of 3 membranes, points at about 80 °C are average of two membranes, error bars are one standard deviation (selectivities calculated per membrane and then averaged).

Figure 4.41 compares the total Kr/Xe ideal selectivity (includes defect permeance) with the defect-free Kr/Xe ideal selectivity. Overall, the average Kr/Xe selectivity increases after the defect permeance is removed. Additionally, a maximum average defect-free Kr/Xe selectivity of 22.7 occurs at 26 °C which is 114% greater than the average total Kr/Xe selectivity at 26 °C. However, the standard deviation of the maximum defect-free selectivity is 23.9 % of the average, which indicates significant variation between membrane defect permeance at ambient temperature.

4.14 SAPO-34 Xe Diffusivity

The average molecular diffusivity of Xe through SAPO-34 was calculated with Equation 2.38, an average SAPO-34 membrane thickness of 11 um (from Figure 4.35), and the Xe lag times of each membrane (Appendix D).

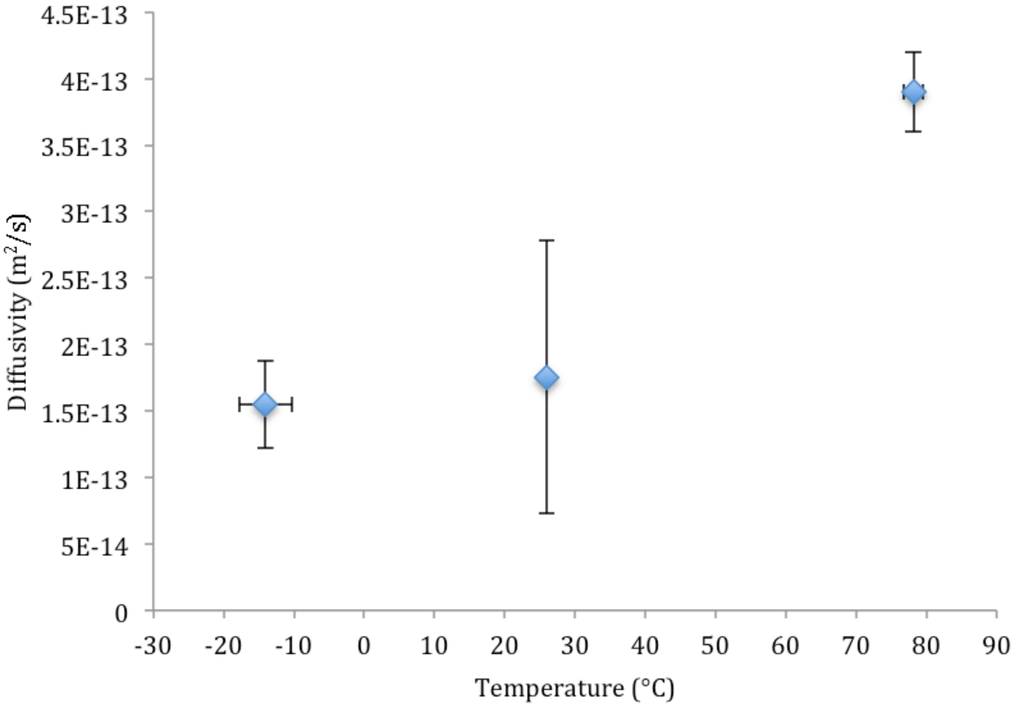

Figure 4.42: Xe diffusivity through SAPO-34 at 15.2 ± 0.1 psia average feed pressure and 15.2 ± 0.1 average pressure drop (95% confidence intervals). Points at about -15°C and 26 °C are average of 3 membranes, points at about 80 °C are average of two membrane, error bars are one standard deviation (diffusivity calculated per membrane and then average).

Figure 4.42 shows that the average Xe diffusivity through SAPO-34 decreases at temperature increases. Thus, the permeance of Xe decreases through SAPO-34 with decreasing temperature because the diffusivity of Xe decreases with temperature. The average diffusivity of Xe through SAPO-34 at 26 °C was 1.75 x 10^{-13} with a standard deviation of 58% of the average. The high standard deviation at 26 °C was due to large variation in the membrane lag times at ambient temperature, which may be caused my large differences between the membrane thicknesses. As a point of comparison, Bakker et al. measured the surface diffusivities of Kr and Xe through an MFI membrane at 30 °C as 5 x 10^{-10} and 2 x 10^{-10} m^2/s, respectively.[7]

4.15 Sealing SAPO-34 Membrane Defects with PDMS

Two SAPO-34 membranes were treated with a 5 wt % PDMS solution in n-hexanes after calcination to attempt sealing the membrane defects with PDMS and prevent unselective transport through the membrane defects. From Figure 4.43, Membrane 1 was synthesized with a synthesis gel molar ratio of 1.0 Al_2O_3:1.0 P_2O_5:0.32 SiO_2:1.0 TEAOH:1.6 DPA:150 H_2O, hydrothermal synthesis time of 6 h, UV treated for 24 h, and calcined at 700 °C for 6 h (0.5 °C/min heating and cooling rate). Membrane 2 was one of the 4 membranes synthesized and tested in Chapter 4.12. Membrane 1 was treated with PDMS three times for one minute each, and Membrane 2 was treated with PDMS one time for 30 seconds (PDMS treatment procedure described in Chapter 3.8). Figure 4.41 compares the Xe and Kr permeation results before and after PDMS treatment for each membrane.

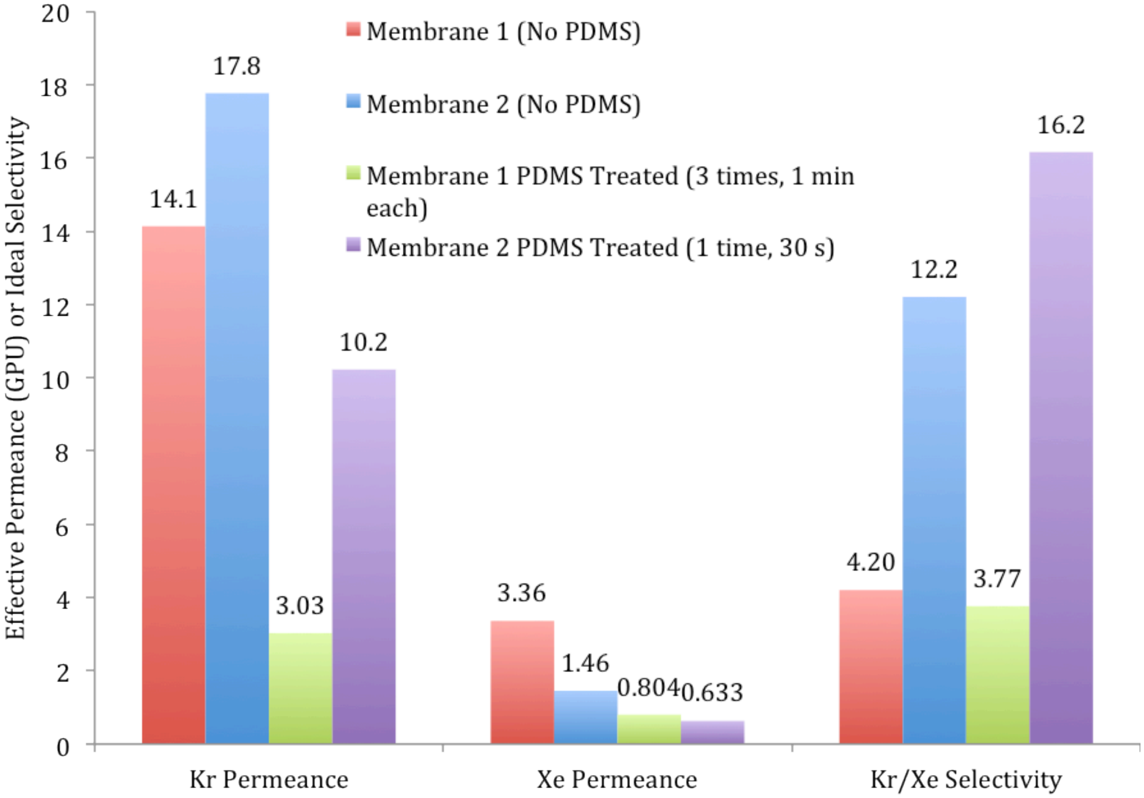

Figure 4.43: PDMS Sealed SAPO-34 Kr and Xe Permeance and Kr/Xe Ideal Selectivity at 15.3 ± 0.1 psia Average Feed Pressure, 15.2 ± 0.1 psia Average Pressure Drop, and 25.3 ± 0.8 °C (95% confidence intervals).

The Kr/Xe ideal selectivity of Membrane 1 decreased by 10.2 % to 3.77 after PDMS treatment, but the Kr/Xe ideal selectivity of Membrane 2 increased by 32.8% to 16.2, which is the highest Kr/Xe selectivity measured at ambient temperature and 1 atm feed pressure in this study. However, after Membrane 2 was PDMS treated the Kr permeance decreased by 46.7 % to 10.2 GPU. The PDMS treatment worked by sealing membrane defects and reducing Xe permeance (Xe permeance reduced 76.1 % for Membrane 1 and 56.6 % for Membrane 2), but Kr permeance also decreased significantly. This may be caused by PDMS depositing on the membrane surface and blocking transport through the zeolite pores. SEM images indicated that after three

PDMS treatments for 1 min each (Membrane 1), a PDMS layer deposited on the surface and covered the zeolite membrane (Figure 4.44). However, Figure 4.45 shows the membrane PDMS treated only once for 30 sec (Membrane 2) does not look any different compared to SAPO-34 membranes not PDMS treated with PDMS (Figure 4.33). Figures 4.46 and 4.47 show the cross-sections of the PMDS treated membranes, but no PDMS layer is visible most likely because the PDMS layer (if any) is not thick enough to see.

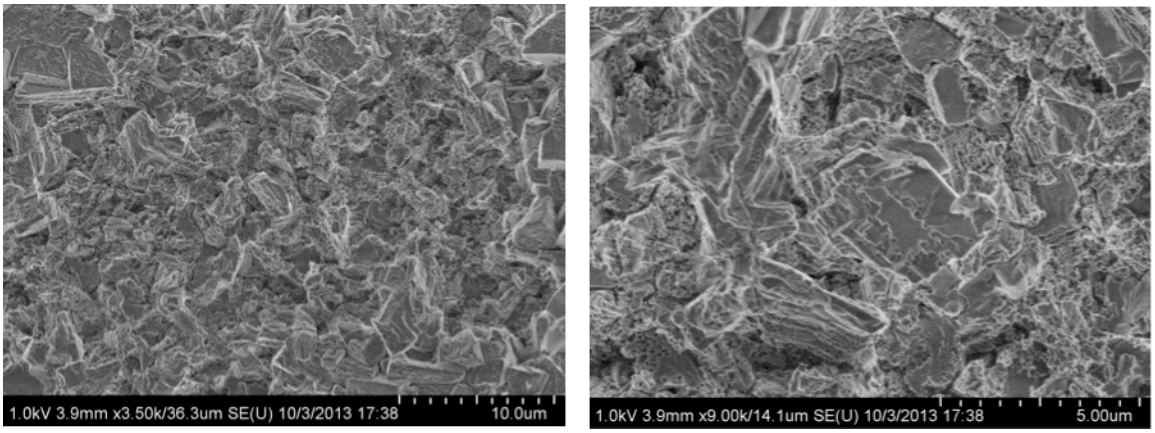

Figure 4.44: SAPO-34 membrane surface (Membrane 1) after three PDMS treatments for 1 min each. SAPO-34 zeolite membrane crystals (Figure 4.33) are not visible because they are covered with a PDMS layer.

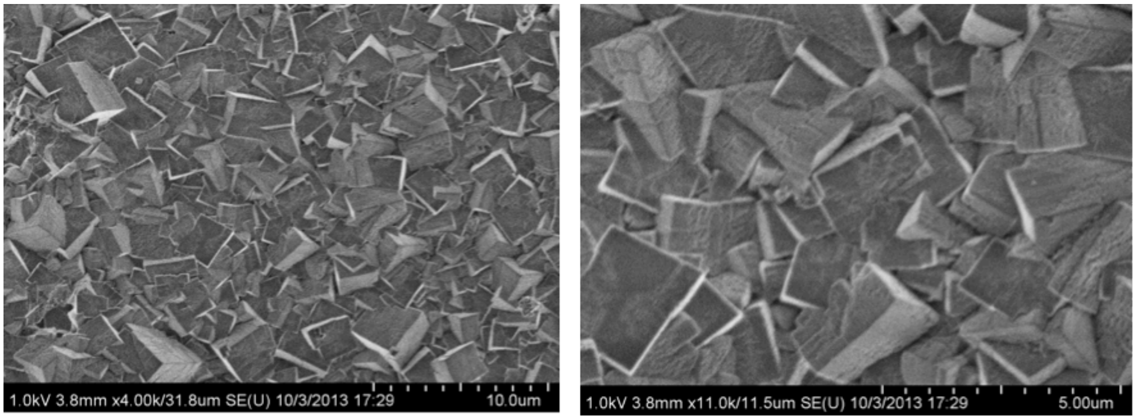

Figure 4.45: SAPO-34 membrane surface (Membrane 2) after a single PDMS treatment for 30 s. SAPO-34 zeolite membrane crystals (Figure 4.33) are visible and not covered by PDMS.

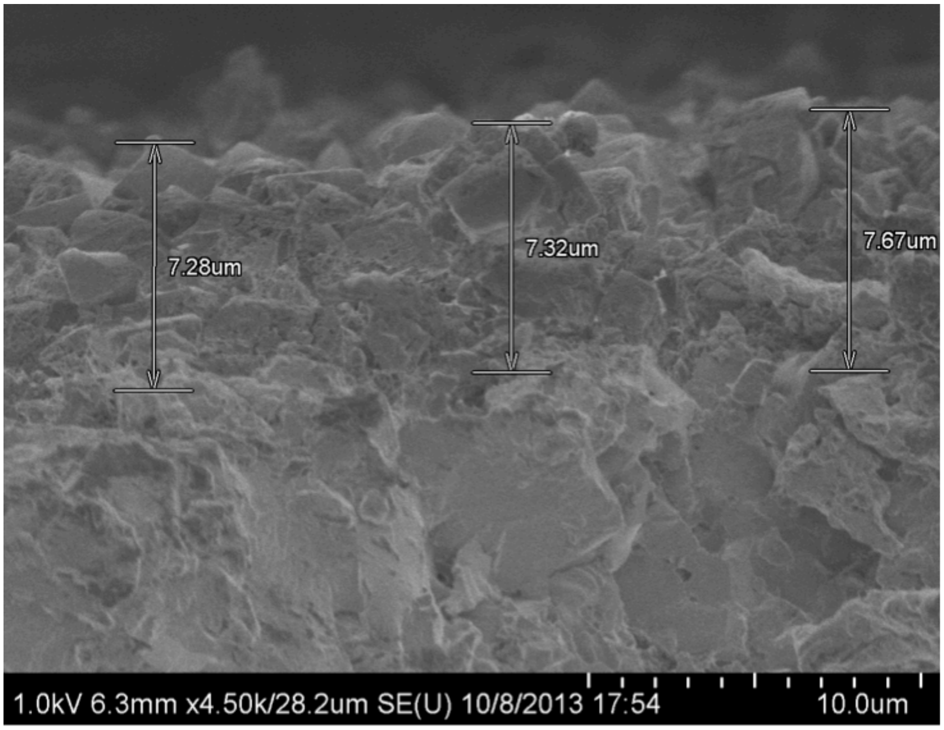

Figure 4.46: SAPO-34 membrane cross-section (Membrane 1) after three PDMS treatments for 1 min each. PDMS layer on membrane surface (Figure 4.44) is not thick enough to see. Average zeolite membrane thickness is 7.42 ± 0.20 µm (95% confidence interval).

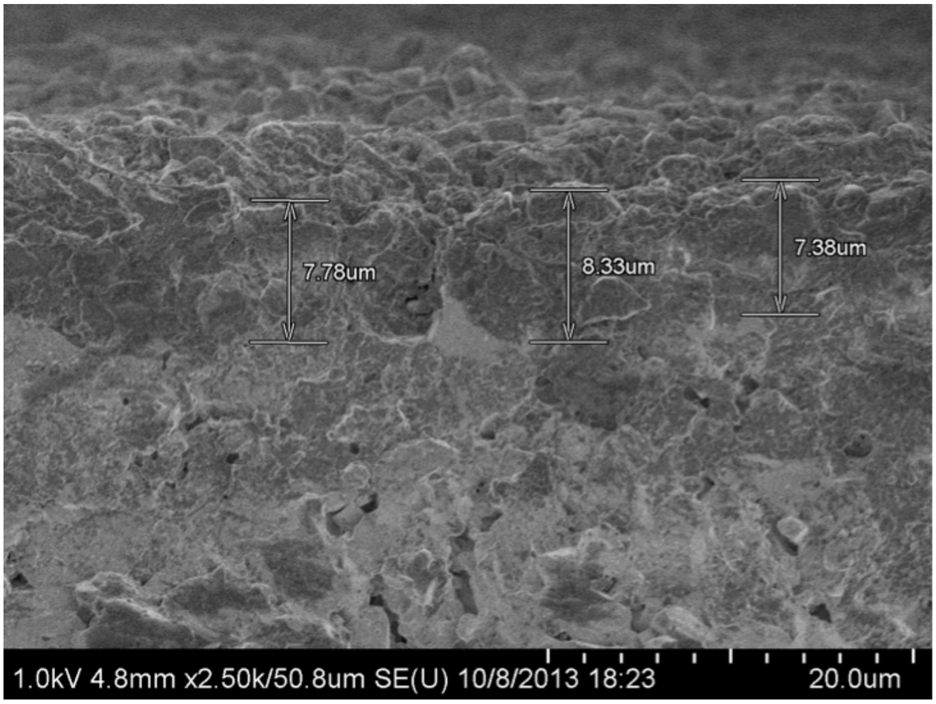

Figure 4.47: SAPO-34 membrane cross-section (Membrane 2) after a single PDMS treatment for 30 s. No PDMS layer is visible compared to SAPO-34 membrane cross-section not PDMS treated pictured in Figures 4.35-36. Average zeolite membrane thickness is 7.83 ± 0.44 μm (95% confidence interval).

4.16 SAPO-34 Membrane Scale-Up Analysis

A scale-up analysis (outlined by Seader et al.) was performed using the experimental results to model a TFF (cross-flow) SAPO-34 membrane.[16] A 1 L/min feed flow rate was assumed with a 0.09%/91% (by mole) Kr/Xe feed stream (0.09%/91% Kr/Xe mixture by volume) at 25 °C, 1 atm feed pressure, and a permeate pressure of zero (vacuum on permeate side). The calculations were performed using a Kr/Xe ideal selectivity of 11.8 and a Kr permeance of 19.4 GPU. In Figures 4.48 and 4.49, the membrane cut is defined as the permeate flow rate divided by the feed flow rate

$$\theta = \frac{n_P}{n_F} \tag{4.1}$$

where θ is the cut, n_P is the permeate molar flow rate, and n_F is the feed molar flow rate. Since the permeate pressure is always zero, the Kr/Xe selectivity is constant across the entire membrane and the cut is calculated by

$$1-\theta=\frac{x_{Kr_F}}{x_{Kr_R}+x_{Kr_R}^{\left(\frac{1}{1-\alpha}\right)}\left[\left(1-x_{Kr_R}\right)^{\left(\frac{\alpha}{\alpha-1}\right)}\left(\frac{x_{Kr_F}}{1-x_{Kr_F}}\right)^{\left(\frac{\alpha}{\alpha-1}\right)}-x_{Kr_R}^{\left(\frac{\alpha}{\alpha-1}\right)}\right]} \tag{4.2}$$

where x_{Kr_F} is the mole fraction of Kr in the feed, x_{Kr_R} is the mole fraction of Kr in the retentate (which decreases along the length of the membrane), and α is the Kr/Xe selectivity. Equation 4.2 was evaluated for incremental values of θ as x_{Kr_R} decreased from 0.09 to 0.001 in increments of 0.001. Then the mole fraction of Kr in the permeate stream is given by

$$y_{Kr_P}=\frac{x_{Kr_F}-x_{Kr_R}\left(1-\theta\right)}{\theta} \tag{4.3}$$

where y_{Kr_P} is the mole fraction of Kr in the permeate stream. Figure 4.48 shows that for a cut of about 0.4, the retentate contains 99.9% Xe and the permeate contains 22% Kr.

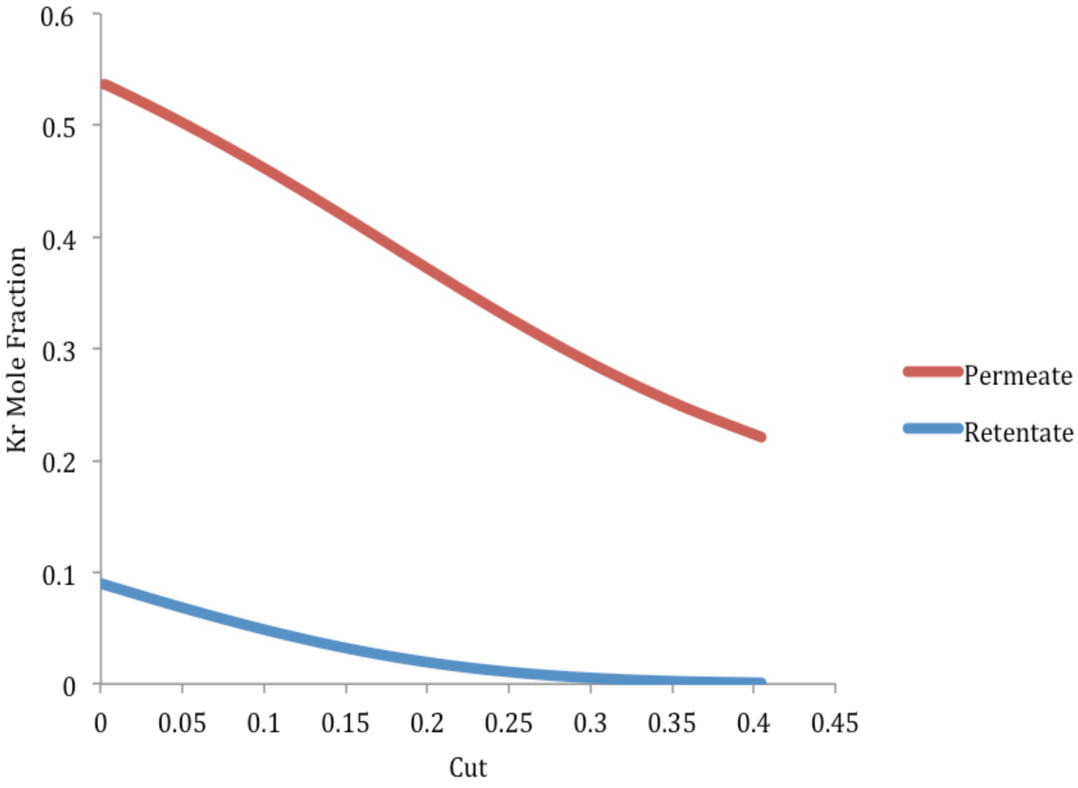

Figure 4.48: Kr mole fraction in permeate and retentate streams vs. cut.

For each differential volume element in the TFF membrane model, the differential area of the membrane is given by

$$dA_M = \frac{y_{Kr}dn}{\overline{P}_{M_{Kr}}\left(x_{Kr}P_F - y_{Kr}P_P\right)} \tag{4.4}$$

where dA_M is a differential element of the membrane area, y_{Kr} is the local Kr mole fraction of the permeate through that differential membrane area, *dn* is the number of moles that permeate through the differential membrane area element, and x_{Kr} is the local Kr mole fraction of the feed. A material balance for Kr around the differential-volume element yields

$$\frac{dn}{dx_{Kr}} = \frac{n}{y_{Kr} - x_{Kr}} \tag{4.5}$$

where n is the local number of moles in the feed and decrease along the length of the membrane. The local mole fraction of Kr (y_{Kr}) is given by

$$y_{Kr} = \frac{\alpha x_{Kr}}{1 + (\alpha - 1) x_{Kr}} \tag{4.6}$$

Equations 4.4, 4.5, and 4.6 where solved numerically using a mole fraction step size of .001 (dx_{Kr}) from 0.09 to 0.001 (note that after each step, n decreases by dn). Each differential area element (dA_M) is summed after every step to give the total membrane area.

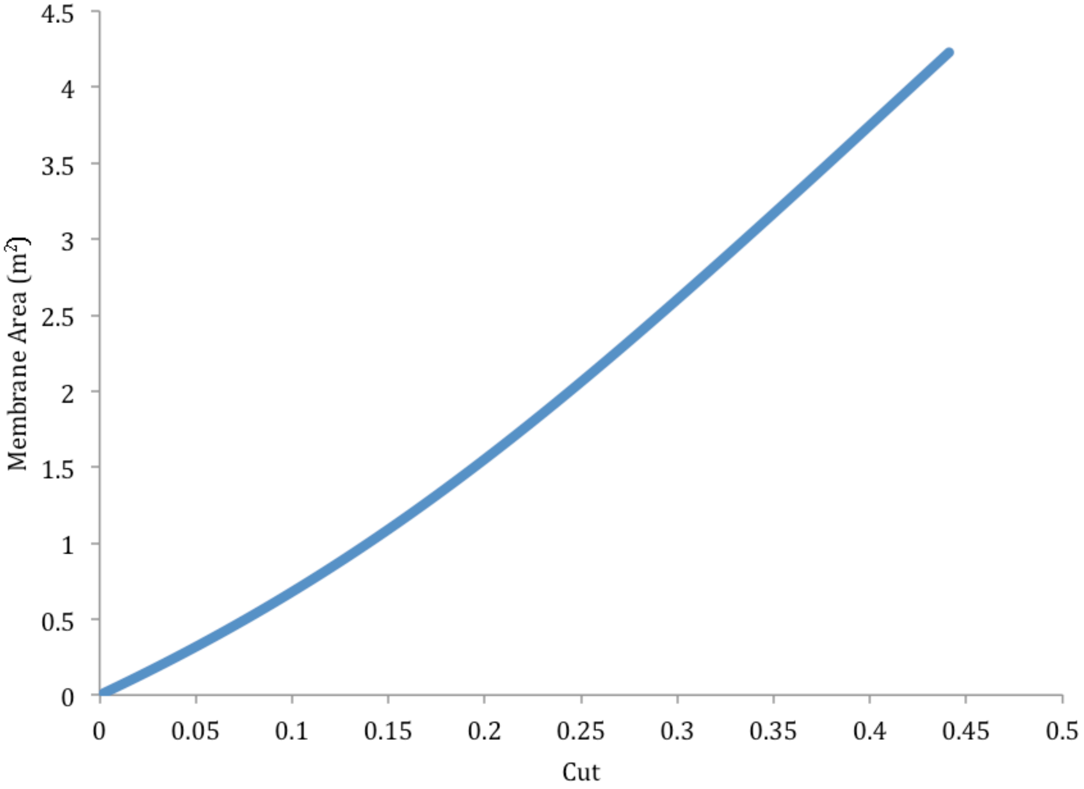

Figure 4.49: Total membrane area vs. cut.

Figure 4.49 shows the total membrane area versus the cut (cut calculated numerically by summing *dn* for every step and dividing the sum by the initial value of *n*, not using Equation 4.2), and 4.2 m^2 of membrane area are required to recover 99.5% (Figure 4.50) of the Kr into the permeate stream. For tubular membranes with an inner diameter of 1 cm and a length of 0.5 m, about 270 tubes would give a total area of 4.2 m^2.

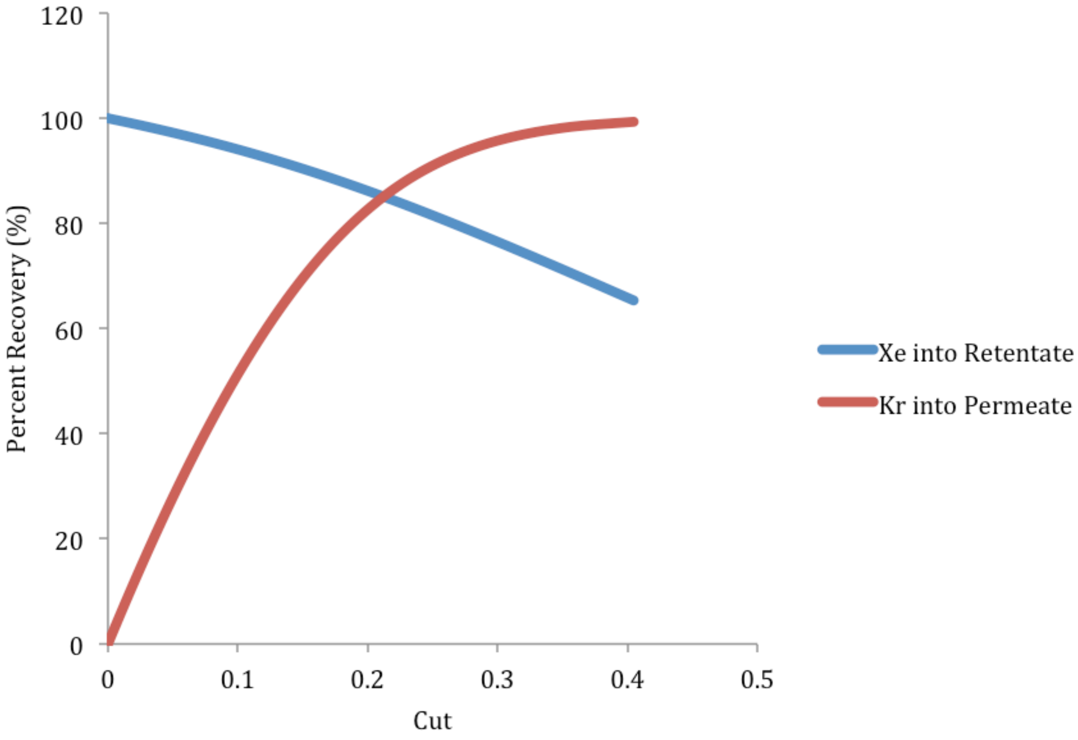

Figure 4.50: Percent recovery of Xe and Kr vs. cut.

With 4.2 m^2 of membrane area, the permeate stream contains 78% Xe and 65% (Figure 4.50) of the Xe is recovered into the retentate stream. To further separate the permeate stream, a series of SAPO-34 cross-flow membrane separation steps can be used until the desired Xe recovery and Kr purity are achieved. Table 4.1 lists the results of six SAPO-

34 cross-flow membrane separation steps in series with the feed to each membrane being the permeate stream of the previous membrane (except for the first step). Table 4.1 shows that three SAPO-34 membrane separation steps are required to recover more than 90% of the Xe in the initial feed stream.

Table 4.1: SAPO-34 membrane separation steps in series with the feed to each membrane being the permeate stream of the previous membrane (except for the first step). All flow rates are at 25 °C and 1 atm, and the Kr/Xe ideal selectivity is 11.8 for each membrane.

Membrane Steps in Series	1	2	3	4	5	6
Cut	0.405	0.540	0.714	0.784	0.876	0.930
Feed Flow Rate (L/Min)	1.00	0.405	0.219	0.156	0.122	0.107
Kr Mole Fraction in Feed	0.09	0.221	0.408	0.572	0.730	0.832
Permeate Flow Rate (L/min)	0.405	0.219	0.156	0.122	0.107	.0996
Kr Mole Fraction in Permeate	0.221	0.408	0.572	0.730	0.832	0.895
Retentate Flow Rate (L/min)	0.595	0.186	0.0626	0.0337	0.0151	0.00749
Xe Mole Fraction in Retentate	0.999	0.999	0.999	0.999	0.999	0.999
Membrane Area (m^2)	4.23	1.75	1.08	0.508	0.321	0.227
Overall Xe Percent Recovery (%) into Retentate	65.3	85.7	92.6	96.3	97.9	98.8

Finally, the SAPO-34 membrane scale-up results can be compared to the cryogenic distillation process designed by Takeuchi for the separation of ^{85}Kr from Xe. The process used a single column that was 3 m tall, had 13 equilibrium stages, and operated at -93 to -95 °C and 2 atm with a reflux ratio of ~190. The distillation column separated a Xe feed (0.6 kg/min) containing 3 ppb of Kr into a Kr-rich distillate stream containing 330 ± 100 ppb of Kr (about 1% Kr) and a purified Xe bottoms stream containing 3.3 ± 1.1 ppt of Kr. The recovery of Xe in the bottoms was about 99%.[17] For distillation separations, the relativity volatility of two components is comparable to the definition of membrane selectivity for two components (Equation 2.21). Relative volatility is defined as

$$\alpha_{A,B} = \frac{\left(y_A / x_A\right)}{\left(y_B / x_B\right)} \tag{4.7}$$

where $\alpha_{A,B}$ is the relative volatility of component A to component B at vapor-liquid equilibrium, y_A is the mole fraction of component A in the vapor phase, x_A is the mole fraction of component A in the liquid phase, y_B is the mole fraction of component B in the vapor phase, x_B is the mole fraction of component B in the liquid phase.[16] Takeuchi reported a Kr/Xe relative volatility of 10.4 at -95 °C and 2 atm, which is lower than the average Kr/Xe ideal selectivity of 11.8 at 25 °C and 1 atm obtained with the SAPO-34 membranes.[17]

4.17 Conclusions

In conclusion, the MFI zeolite membrane, DDR zeolite membrane, and amorphous carbon membranes did not separate Kr and Xe with high selectivity and high Kr permeance. However, SAPO-34 zeolite membranes were able to separate Kr and Xe with an average Kr/Xe ideal selectivity of 11.8 and an average Kr permeance of 19.4 GPU at ambient temperature and a 1 atm feed pressure. Also, an analysis of the SAPO-34 membrane defect permeance determined that the average Kr/Xe selectivity decreased by 53% at room temperature due to unselective defect permeance by Knudsen diffusion. However, sealing the membrane defects with PDMS increased Kr/Xe selectivity by 32.8% to 16.2 and retained a high Kr membrane permeance of 10.2 GPU at ambient temperature. Overall, this research has shown that high quality SAPO-34 membranes can be consistently fabricated to achieve a Kr/Xe ideal selectivity >10 and Kr permeance >10 GPU at ambient temperature and 1 atm feed pressure. Furthermore, a scale-up analysis based on the experimental results determined that a cross-flow SAPO-34 membrane with a Kr/Xe selectivity of 11.8 and an area of 4.2 m^2 would recover 99.5% of the ^{85}Kr from a 1 L/min feed stream containing 0.09% Kr and 0.91% Xe (at ambient temperature and 1 atm feed pressure) and produce a retentate stream containing 99.9% Xe.

4.18 Recommendations

Although SAPO-34 membranes have shown promising results for separating Kr and Xe, further work is necessary to develop SAPO-34 membranes for separation of ^{85}Kr and Xe from nuclear reprocessing off-gas. The SAPO-34 membranes should be synthesized on hollow tubular supports and tested in cross-flow filtration mode with Kr/Xe feed mixtures to verify the Kr/Xe ideal selectivity obtained with disc membranes. Also, other feed gas mixtures containing N_2, O_2, and CO_2 with Kr and Xe should be tested to determine SAPO-34 membrane Kr/Xe selectivity in the presence of these feed components. Furthermore, the characteristic diffusion and adsorption coefficients of Kr and Xe should be measured to determine the intrinsic Kr/Xe selectivity of SAPO-34. This can be accomplished by measuring the Kr and Xe molar uptake in SAPO-34 seeds with a pressure decay cell. Finally, SAPO-34 membranes must be subjected to a representative radioactive environment and then retested for Kr/Xe selectivity to verify that radiation exposure will not compromise the membrane performance.

4.19 References

1. Yan, Y., Davis, M. E., & Gavalas, G. R. (1995). Preparation of Zeolite ZSM-5 Membranes by In-Situ Crystallization on Porous α-Al_2O_3. *Industrial & Engineering Chemistry Research, 34(5)*, 1652-1661.
2. Boumaza, A., Favaro, L., Lédion, J., Sattonnay, G., Brubach, J. B., Berthet, P., ... & Tétot, R. (2009). Transition alumina phases induced by heat treatment of boehmite: an X-ray diffraction and infrared spectroscopy study. *Journal of Solid State Chemistry, 182(5)*, 1173.
3. Carruthers, J. D., Payne, D. A., Sing, K. S. W., & Stryker, L. J. (1971). Specific and nonspecific interactions in the adsorption of argon, nitrogen, and water vapor on oxides. *Journal of Colloid and Interface Science, 36(2)*, 205-216.
4. Adnadjević, B., Vukićević, J., Filipović-Rojka, Z., & Marković, V. (1990). The influence of NaX zeolite particle size on crystallinity measured by the XRD method. *Zeolites, 10(7)*, 699-702.
5. Van den Broeke, L. J. P., Kapteijn, F., & Moulijn, J. A. (1999). Transport and separation properties of a silicalite-1 membrane - II. Variable separation factor. *Chemical Engineering Science, 54(2)*, 259-269.

6. Prausnitz, J. M., Lichtenthaler, R. N., & de Azevedo, E. G. (1998). *Molecular thermodynamics of fluid-phase equilibria*. Pearson Education. 57-72.
7. Bakker, W. J., Van Den Broeke, L. J., Kapteijn, F., & Moulijn, J. A. (1997). Temperature dependence of one - component permeation through a silicalite -1 membrane. *AIChE Journal, 43(9)*, 2203-2214.
8. Bhave, R., *Personal Communication*. 2013.
9. Zhengzhi, Z., McCarley, K. C., Drese, J. H., & Nair, S. (2013). Zeolite DDR Submicron Crystals and Membranes for Gas Separation: Synthesis and Post-Treatment. Unpublished manuscript. *Georgia Institute of Technology, Atlanta, GA.*
10. Van den Bergh, J., Zhu, W., Gascon, J., Moulijn, J. A., & Kapteijn, F. (2008). Separation and permeation characteristics of a DD3R zeolite membrane. *Journal of Membrane Science, 316(1)*, 35-45.
11. Kapko, V., Dawson, C., Treacy, M. M. J., & Thorpe, M. F. (2010). Flexibility of ideal zeolite frameworks. *Physical Chemistry Chemical Physics, 12(30)*, 8531-8541.
12. Carreon, M. A., Li, S., Falconer, J. L., & Noble, R. D. (2008). Alumina-supported SAPO-34 membranes for CO2/CH4 separation. *Journal of the American Chemical Society, 130(16)*, 5412-5413.
13. Carreon, M. A., Li, S., Falconer, J. L., & Noble, R. D. (2008). SAPO-34 Seeds and Membranes Prepared Using Multiple Structure Directing Agents. *Advanced Materials, 20(4)*, 729-732.

14. Caro, J., Albrecht, D., & Noack, M. (2009). Why is it so extremely difficult to prepare shape-selective Al-rich zeolite membranes like LTA and FAU for gas separation?. *Separation and Purification Technology, 66(1)*, 143-147.
15. Li, S., Carreon, M. A., Zhang, Y., Funke, H. H., Noble, R. D., & Falconer, J. L. (2010). Scale-up of SAPO-34 membranes for CO_2/CH_4 separation. *Journal of Membrane Science, 352(1)*, 7-13.
16. Seader, J. D. (2006). *Separation process principles*. Wiley. 2nd Edition. 119-512.
17. Takeuchi, Y. (2005). Distillation purification of xenon for krypton and measurement of radon contamination in liquid xenon. *Proceedings of the XeSAT*. Retrieved from http://www-sk1.icrr.u-tokyo.ac.jp/xmass/prelist/xesat2005-xmass-mar2005.pdf.

APPENDIX A

Leak Rate for Permeation Units and Disc Permeation Cell

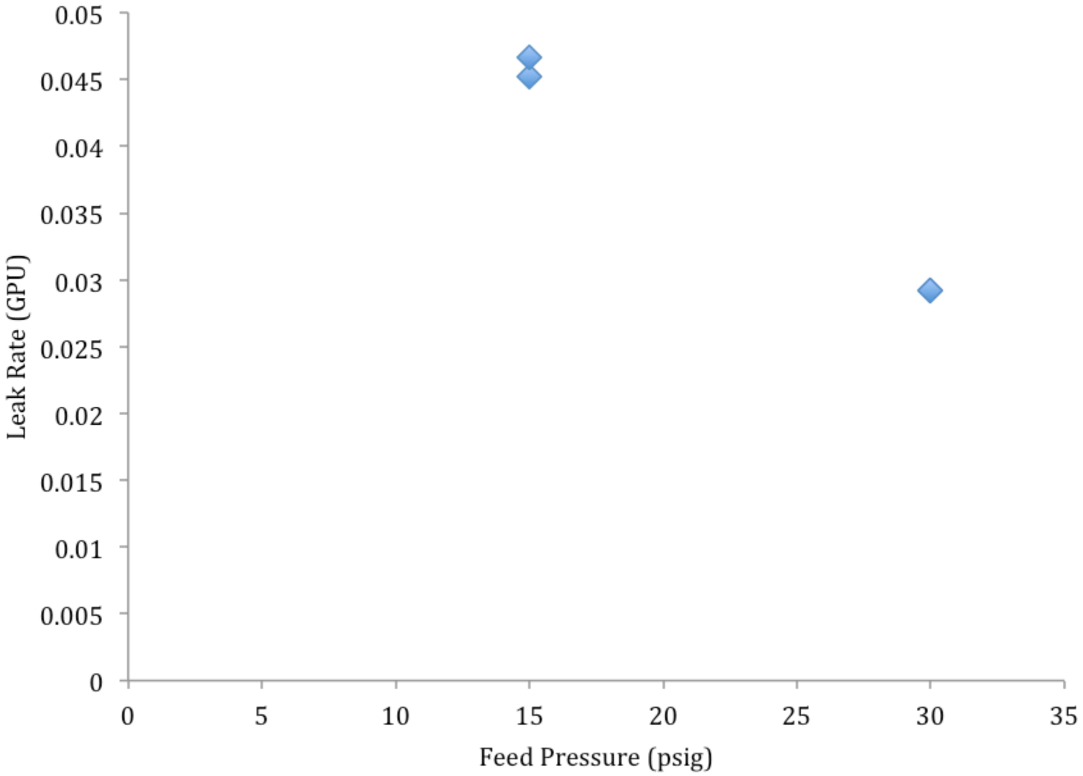

Figure A.1: N_2 leak rate at 50 °C and nonporous metal disc installed in disc permeation cell. Permeate pressure initially at ~0 psia.

APPENDIX B

Permeation Unit Flow Diagram

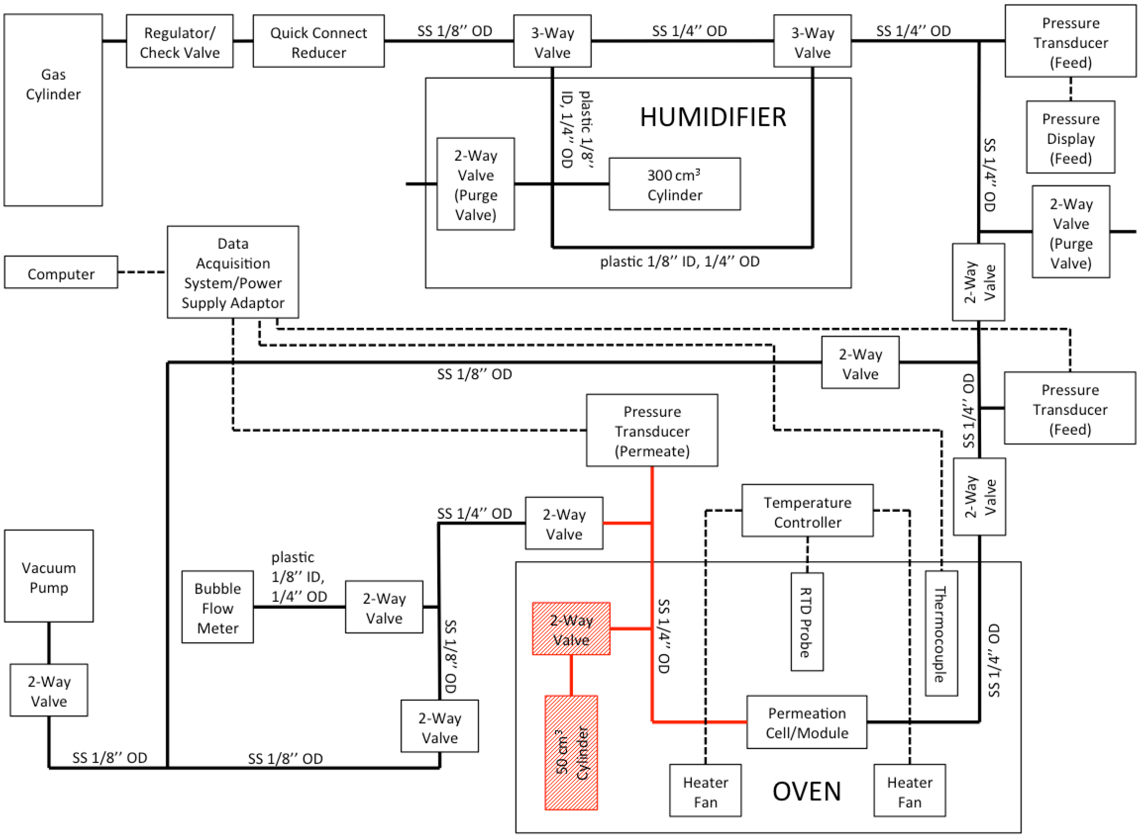

Figure B.1: Permeation unit flow diagram. Permeate gas collection volume is red. The humidifier was not used in this research.

APPENDIX C

MATLAB Code for Linear Regression Analysis of Permeation Data

```
function A = PermSlope(excelFile)
% The input is an Excel file with five columns of data
% Column 1 contains the time stamps for each measurement (not used for calculations)
% Column 2 contains the data (MM/DD/YY) of each measurement (not used for calculations)
% Column 3 contains the feed pressure measurements in psia
% Column 4 contains the permeate pressure measurements in psia
% Column 5 contains the temperature measurements in degrees Celsius
% This code uses all of the inputted pressure measurements that are positive
% to perform the linear regression analysis. Negative pressure values are
% caused by calibration error in the pressure transducers all low pressures
% and all negative pressure values are truncated from the inputted data.
num = xlsread(excelFile); % extract Excel file data
feed = transpose(num(:,3)); % feed pressure in third column
perm = transpose(num(:,4)); % permeate pressure in fourth column
temp = transpose(num(:,5)); % temperature in fifth column
for i = 1:length(perm) % find last negative number in permeate column
    if perm(i) < 0
        posSec = i+1; % set time starting position to one plus the position of the last
negative number in permeate pressure column
    end
end
posPerm = perm(posSec:end); % truncate all numbers before and including last negative
number in permeate column
sec = length(posPerm); % numbers of seconds (scans) used for data analysis
posFeed = feed(posSec:end); % truncate all numbers before and including last negative
number in permeate column
posTemp = temp(posSec:end); % truncate all numbers before and including last negative
number in permeate column
avgFeed = sum(posFeed)/length(posFeed); % average feed pressure
stdFeed = std(posFeed, 1); % standard deviation based on population
pdFeed = fitdist(posFeed.', 'Normal'); % fit to normal probability distribution
ciFeed = paramci(pdFeed, 0.05);% 95% confidence interval
meanciFeed = avgFeed - ciFeed(1,1); % plus/minus confidence interval around mean feed
pressure
avgPerm = sum(posPerm)/length(posPerm); % average permeate pressure
stdPerm = std(posPerm, 1); % standard deviation based on population
pdPerm = fitdist(posPerm.', 'Normal'); % fit to normal probability distribution
ciPerm = paramci(pdPerm, 0.05); % 95% confidence interval
meanciPerm = avgPerm - ciPerm(1,1); % plus/minus confidence interval around mean permeate
pressure
avgTemp = sum(posTemp)/length(posTemp); % average temperature
stdTemp = std(posTemp, 1); % standard deviation based on population
pdTemp = fitdist(posTemp.', 'Normal'); % fit to normal probability distribution
ciTemp = paramci(pdTemp, 0.05 );% 95% confidence interval
meanciTemp = avgTemp - ciTemp(1,1); % plus/minus confidence interval around mean
temperature
secVec = 1:sec; % second vector
p = polyfit(secVec ,posPerm, 1); % fit permeate pressure data to a line
slope = p(1,1); % slope of permeate pressure fit
int = p(1,2); % intercept of permeate pressure fit
R = corrcoef(secVec, posPerm); % compute correlation coefficient for linear fit
fit = R(1,2); % correlation coefficient (R^2 value)
A = {excelFile(1:end-5), [], [], [];
    [], [], 'Standard Devaition (based on Population)', '95% Confidence Interval around
Mean (based on Normal Distribution)';
    'Average Feed Pressure (PSIA)', avgFeed, stdFeed, meanciFeed;
    'Average Permeate Pressure (PSIA)', avgPerm, stdPerm, meanciPerm;
    'Average Temperature (C)', avgTemp, stdTemp, meanciTemp;
    'Time (s)', sec, [], [];
    'Slope (PSIA/s)', slope, [], [];
    'Intercept (PSIA)', int, [], [];
    'Correlation Coefficient (R^2)', fit, [], []}; % put data analysis results into a
cell matrix
newFileName = strcat(excelFile(1:end-5), '_MATLAB'); % name for new Excel file
xlswrite(newFileName, A) % write data analysis results to new Excel file
end
```

APPENDIX D

Lag Time Graphical Analysis

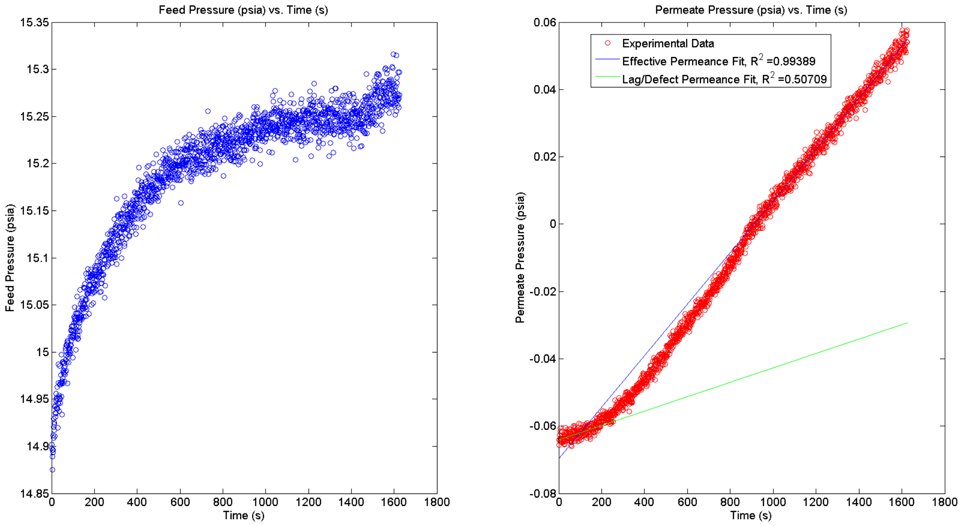

Figure D.1: SAPO-34 Xe permeation at -8.84 °C (sample # 1). Lag time is 123 s.

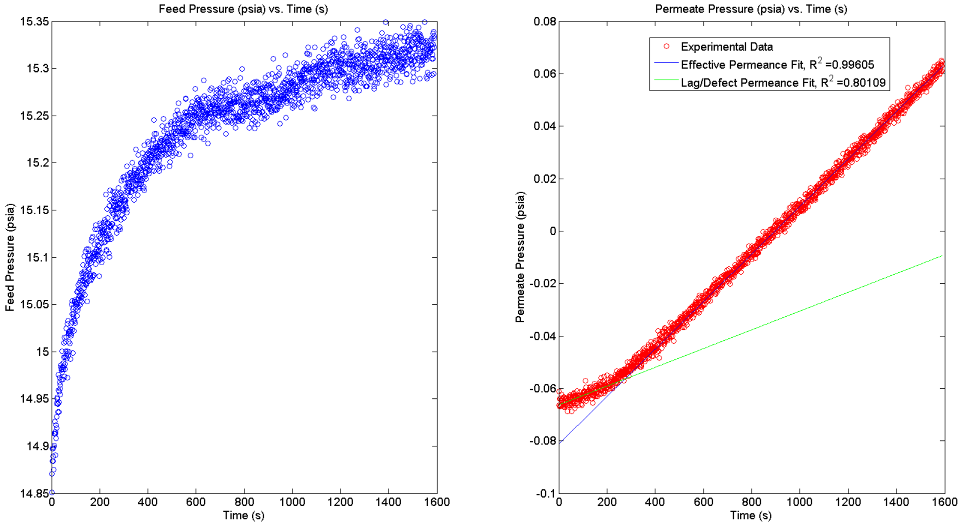

Figure D.2: SAPO-34 Xe permeation at 25.5 °C (sample # 1). Lag time is 210 s.

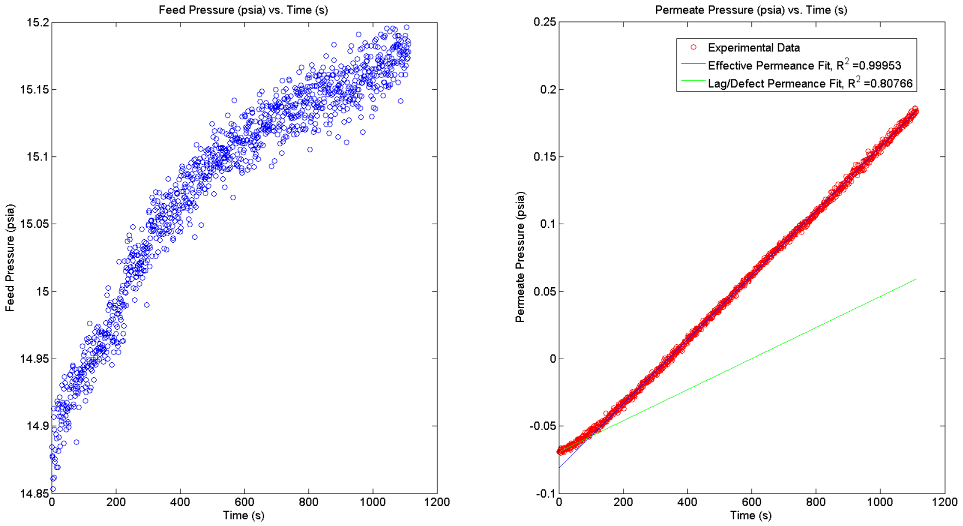

Figure D.3: SAPO-34 Xe permeation at 80.8 °C (sample # 1). Lag time is 43 s.

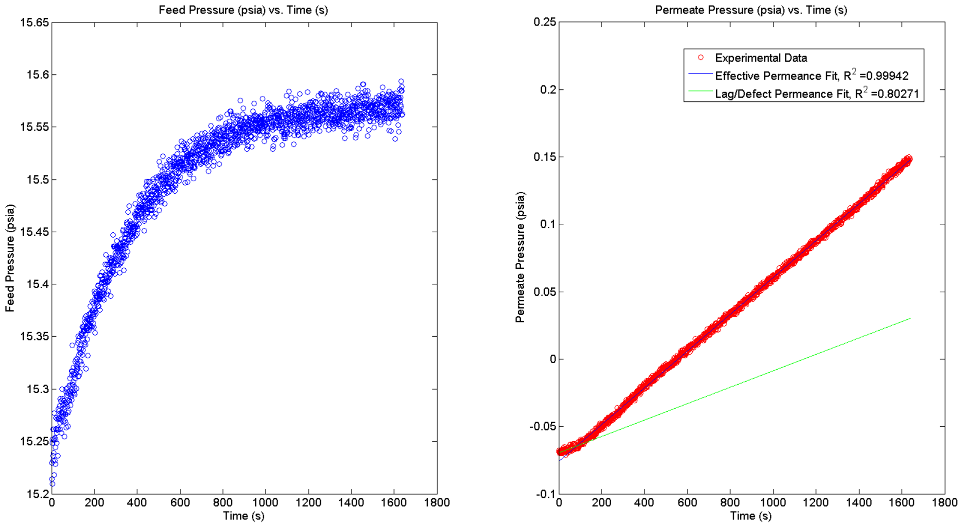

Figure D.4: SAPO-34 Xe permeation at -16.4 °C (sample # 4). Lag time is 106 s.

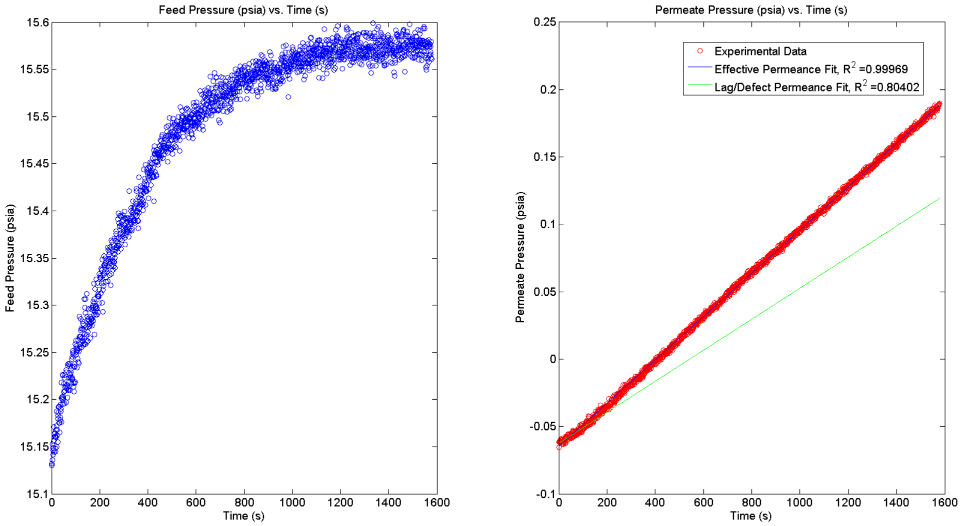

Figure D.5: SAPO-34 Xe permeation at 25.9 °C (sample # 4). Lag time is 63 s.

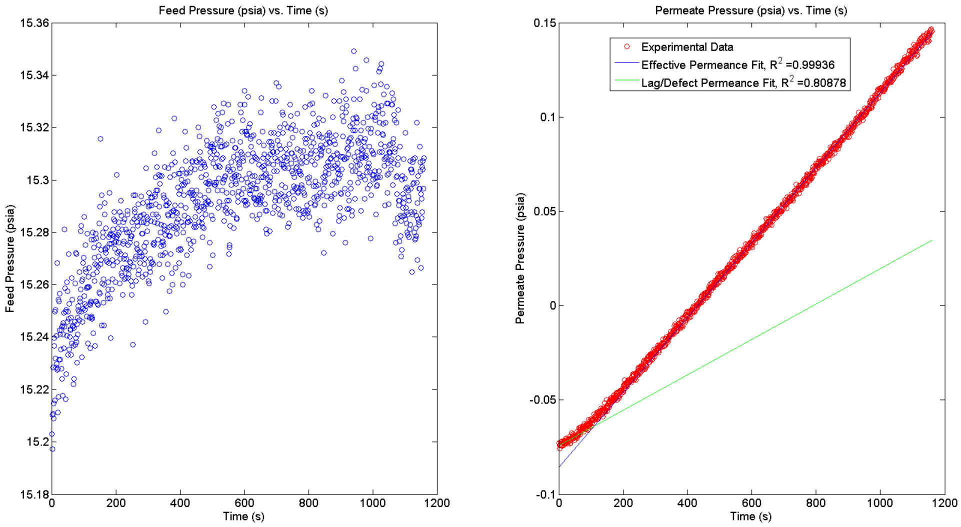

Figure D.6: SAPO-34 Xe permeation at 77.6 °C (sample # 4). Lag time is 56 s.

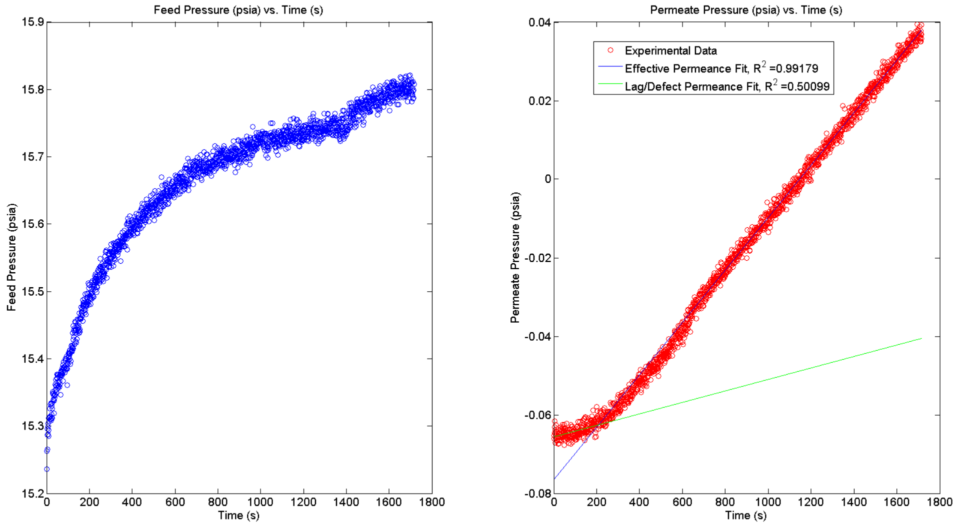

Figure D.7: SAPO-34 Xe permeation at -16.3 °C (sample # 5). Lag time is 182 s.

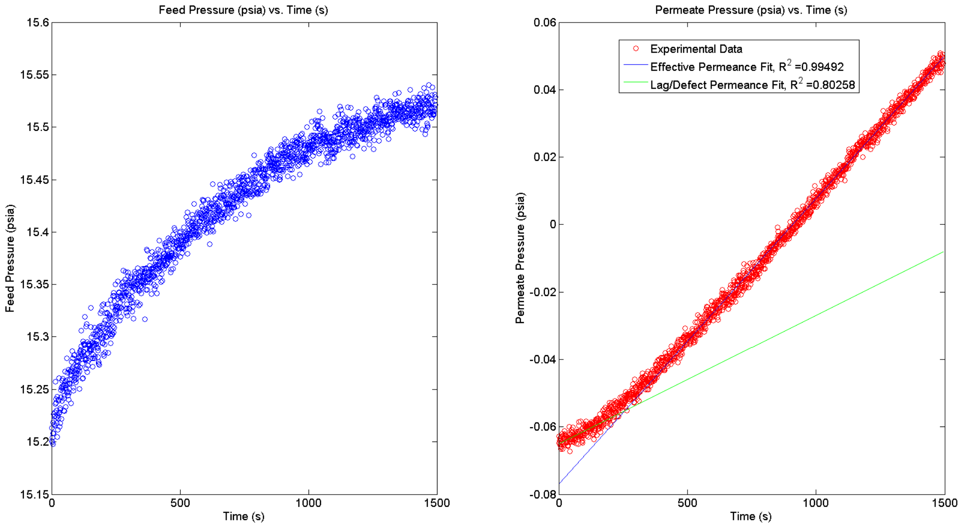

Figure D.8: SAPO-34 Xe permeation at 25.8 °C (sample # 5). Lag time is 183 s.